NOAA Technical Memorandum ERL NSSL-85

A DUAL DOPPLER VARIATIONAL OBJECTIVE ANALYSIS AS APPLIED TO STUDIES OF CONVECTIVE STORMS

Conrad L. Ziegler

National Severe Storms Laboratory
Norman, Oklahoma
November 1978

UNITED STATES DEPARTMENT OF COMMERCE
Juanita M. Kreps, Secretary

NATIONAL OCEANIC AND ATMOSPHERIC ADMINISTRATION
Richard A. Frank, Administrator

Environmental Research Laboratories
Wilmot N. Hess, Director

TABLE OF CONTENTS

LIST OF FIGURES

LIST OF TABLES

A DUAL DOPPER VARIATIONAL OBJECTIVE ANALYSIS AS APPLIED TO STUDIES OF CONVECTIVE STORMS

Conrad L. Ziegler

1. INTRODUCTION

Numerous investigations in the past ten years have sought to determine wind velocities in precipitating weather systems from pulse Doppler data. At least two Doppler radars scanning a common volume are necessary to adequately deduce in-storm velocities. Although additional radars reduce error variance in estimated winds, fabrication costs may limit many institutions to the use of only two radars. Additionally, a storm located well outside the area circumscribed by three or more radars can be analyzed nearly as accurately with the closest two radars as with three or more radars. This thesis demonstrates that tangible gains in accuracy of dual Doppler derived wind fields can be realized through application of all known information in determining velocities, including Doppler measurements, kinematic constraints, Doppler measurement error, and general knowledge of severe storm structure based on theoretical and numerical models. The new technique is applied to the analysis of Doppler data in selected convective storms where results from a conventional dual Doppler analysis and of three or four radar analyses are available. An evaluation of the relative merits of the various analyses is performed. The new technique is applied to a study of the structure and evolution of an isolated hail-bearing convective storm. Storm motion, nearly 90° to the right of mid- and upper-tropospheric winds, may be explained by continuous propagation as deduced from synthesized wind fields. A simple hail growth model in concert with derived wind fields produces realistic hailstones deposited near a ground hail-sampling site. Air trajectory computations suggest that air, transported into the upper troposphere by updrafts, remains at high levels despite the presence of deep downdrafts.

2. DUAL DOPPLER DATA ANALYSIS TECHNIQUE

2.1 History of Dual Doppler Analysis Methods

Early dual Doppler data analysis techniques stressed the synthesis of two independent Doppler velocity estimates to deduce at most two air motion components. Later efforts included kinematic constraints on the three-dimensional wind field in order to estimate the third (quasi-vertical) wind component. Browning et al. (1968) utilized two 3 cm wavelength Doppler radars, one fixed pointing vertically and the other scanning in elevation so that the two radars could illuminate a common volume. For a shower moving directly over the vertically-pointing radar, the mean vertical wind component W_p was estimated from the velocity spectrum. The mean radial velocity component V_p was estimated by the scanning radar. For an echo at elevation angle ε, the horizontal wind component U_β in the plane containing the scanning radars' beam was calculated from $U_\beta = V_p(\cos \varepsilon)^{-1} - W_p \tan \varepsilon$. Time-height sections of W_p and U_β were transformed according to known echo motion into a

vertical space cross-section in order to estimate precipitation trajectories in the plane. To utilize wind information in this manner, steadiness of the wind field following the motion was assumed for the data collection period of approximately 10 minutes. Peace and Brown (1968) used graphical techniques to combine radial velocity estimates from two remotely spaced Doppler radars that scanned in azimuth at low elevation angles. Contribution of vertical air and precipitation particle motion to radial velocity was negligable. To produce maps of horizontal velocities, it was necessary to assume storm stationarity while adjusting the positions of asynchronously observed velocities by time-to-space advection. These pioneering studies demonstrated the great potential of dual Doppler systems to aid in the study of precipitating weather systems.

Armijo (1969) derived general formulations of the two and three Doppler analysis problems. He considered the geometric relations between radial velocity estimates, the three Cartesian wind components, and the mean hydrometeor fall speed. He further utilized the continuity equation for air in anelastic form, with the logarithmic vertical gradient of air density assumed constant. For the dual Doppler case, he proposed a transformation of coordinates from radar spherical to cylindrical geometry to ease solution of the governing system of equations. For the dual Doppler problem to be well-posed, it was necessary to assume that the hydrometeor terminal fallspeed was known everywhere in the analysis domain. Smoothing of data was suggested as a means of reducing error in derived wind velocites. Lhermitte and Miller (1970) proposed a dual Doppler data collection scheme and wind synthesis based upon the formulation of the dual Doppler problem in cylindrical geometry. The two radars' scanning is coordinated such that both radar beams move within a common plane. This scanning method (COPLAN scanning) relaxes assumptions of storm stationarity and simplifies interpolation procedures. The wind components in evenly spaced, tilted planes common to both radars, are synthesized from interpolated radial velocity estimates. Frisch et al. (1974) and Miller and Strauch (1974) applied the COPLAN scheme to data collected in the lowest kilometer of a Colorado snowstorm. The incompressible continuity equation in cylindrical coordinates, was integrated vertically to obtain the orthogonal (nearly vertical) wind component. Finally, Cartesian components were computed and interpolated to a suitable Cartesian grid. The solution fields were displayed in vertical cross-sections in both studies, and also on horizontal planes in the latter report. Ray et al. (1975) documented a dual Doppler radar study of a tornadic storm in central Oklahoma, and introduced the anelastic form of the continuity equation into dual Doppler analysis. Two 10 cm wavelength radars scanned a common volume, each turning through a specified azimuth interval at constant elevation, then tilting upward by a fixed elevation increment and scanning back in azimuth. This process was repeated until each radar had scanned through storm mid-levels and completed the tilt sequence. Data in quasi-horizontal azimuthal scan sectors for each radar were obtained at approximately the same time. Data positions were adjusted for storm motion, then interpolated in 3-space to a common grid in cylindrical coordinates. A synthesis of wind components in tilted planes was performed, incorporating a terminal velocity-reflectivity relation. Vertical integration of the anelastic continuity equation produced the vertical wind component after the horizontal wind fields had been smoothed using a two dimensional filter. Interpolation of reflectivity and velocities to a

suitable Cartesian grid completed the objective analysis. Reflectivities and velocities were displayed on horizontal planes and vertical sections to facilitate meteorological analysis. The interpolation scheme involved computation of weighted averages at gridpoints using a distance dependent weighting function within an oblate-spheroidal influence volume. The degree of smoothing during interpolation could be controlled by varying the dimensions of the influence volume, which for this study assumed the proportions of individual grid elements. Studies by Miller (1975) and Kropfli and Miller (1976) utilized the previously outlined COPLAN or coplane technique to determine the wind and reflectivity structure of deep convective storms in northeastern Colorado. Both analyses featured the assumption of a reflectivity-terminal fallspeed relation, and use of the anelastic continuity equation to deduce the vertical wind component from the two synthesized coplane wind components. Doviak et al. (1976) performed a detailed error analysis applicable to dual Doppler analyses, where the initial synthesis of wind components is assumed to have been performed in cylindrical coordinates. Results were obtained for bivariate and distance-weighting interpolation methods. Expressions were derived for error variance of cylindrical coordinate wind components, direction and magnitude standard deviations of horizontal Cartesian wind components, and also for magnitude standard deviation of the vertical Cartesian wind component. Maps of spatial error distributions relative to a radar site were presented. Brandes (1977) used a dual Doppler analysis scheme in which wind components were synthesized from Doppler observations directly within a Cartesian grid, bypassing analysis procedures in cylindrical coordinates altogether. Two equations relating Doppler velocities to Cartesian wind components, the anelastic continuity equation, and an expression relating reflectivity and terminal fallspeed, formed the set of analysis equations. Reflectivities and Doppler velocities were spatially interpolated to a Cartesian grid using an exponential weighting function within an oblate spheroidal influence volume on the order of the volume of a grid cube. The vertical component w was determined iteratively from the continuity equation and an initial guess field w'. On each iteration, successive approximations of the w field were used to determine approximate horizontal wind components to be used in the continuity equation. Advantages of this scheme are that only one interpolation is needed, and that the grid may be set in an east-west, north-south configuration regardless of the orientation of the radar system.

2.2 The Variational Approach to Dual Doppler Analysis

The previous discussion of dual Doppler analysis techniques illustrates the reliance on the continuity equation as an analysis constraint. Independent measurements of the temperature and pressure fields within convective storms are not currently available to the analyst. Since the only data source is Doppler measurements, the kinematic method of deducing vertical velocity is the lone recourse. Any method of determining vertical velocities should consider measurement and/or analyses errors when they are significant.

Several error sources may substantially contribute to uncertainties in derived vertical wind when the kinematic method is applied to Doppler velocity estimates. 1) Estimation of the mean Doppler velocity from a velocity spectrum has an associated error. 2) In addition, storm structure is assumed not to

change over the data collection period. If storm structure does indeed change, significant error will result when observations are merely advected a distance proportional to the difference between observation time and analysis time to a new location, accommodating storm translation. This operation will introduce error if the storm fields decorrelate over the data collection period. In severe storms where the magnitudes of time derivatives following the motion may be far greater than for weak convective showers, the assumption of storm stationarity may have serious consequences. Generally, larger errors may associate with longer data collection periods. A related problem involves the combination of Doppler velocities from a given region within a convective cloud when the tilt sequences for each radar are only approximately coordinated in time. A storm discussed in this thesis, for example, was studied by using Doppler data sets separated by 7 minutes at lowest levels and 4 minutes at storm top. These data sets did not overlap in time for any given region in the cloud. Time-weighting of observations will not ameliorate this situation if the time weights do not reflect the time decorrelations or if the decorrelation time is a fraction of the collection time. This error is difficult to estimate quantitatively without knowledge of the time evolution of convective storm fields. 3) As pointed out by Ray and Wagner (1976), error accumulation during numerical integration of the continuity equation and poor sampling of low-level winds both contribute to uncertainty in the derived vertical wind. The latter difficulty introduces a nearly constant bias into the vertical motion profile which would in general be horizontally variable. This reflects the variability of the horizontal divergence. Truncation errors related to the application of the continuity equation on a large grid mesh will also contribute to errors in computed vertical velocity. These errors cannot be estimated without a more detailed knowledge of subgrid scale motions. The most effective recourse against this latter error would be to use radars which collect data with a higher spatial density, allowing the analyst to define smaller scales.

It is desired to develop an alternative dual Doppler analysis technique which is less likely to admit the above sources of error such that the derived vertical motion fields constitute physically improved estimates. The need for such an analysis is suggested by the typical observations in conventional dual Doppler analyses, that vertical velocities at high levels are unrealistically large and characterized by excessive horizontal variability. The temporal and spatial variations of storm hydrometeor fields as indicated by radar reflectivities, do not appear to agree in all cases with computed vertical velocities from continuity considerations. Recent numerical cloud simulations (e.g., Hane, 1973; Wilhelmson, 1974) indicate that vertical motion and water content in the upper levels of simulated deep convection show generally good correlation and common scales of horizontal variation. Updraft maxima were invariably near mid-levels during the clouds' mature stage, despite the presence of considerable thermal buoyancy above the updraft maximum. This configuration relates to the strong influence of the perturbation pressure. This result was not obtained in one-dimensional cloud models (Srivastava, 1967, Danielsen, et al, 1972), where updraft maxima were observed near cloud top. In these models, the perturbation pressure was not included. In the multi-dimensional investigations, compensating downdrafts in upper levels were less than or of the order of maximum updrafts at the same level.

The cores of high liquid water content usually coincided with the updraft plume. The generation, vertical advection, and storage of condensate in the updraft were found to be important to the maintenance of the relation between wind and water fields. Profiles of vertical velocity had a convergent tendency i.e., large values in mid-levels gradually giving way to small values near cloud top. These results suggest that Doppler-derived vertical velocities should also be small near cloud top and that the level of maximum updraft should be considerably lower than that frequently observed in synthesized wind fields.

In the case of rapidly overshooting or collapsing storm towers in the vicinity of the tropopause, updrafts and/or downdrafts of order 10 m s^{-1} or larger are possible. Figures 1 through 5 illustrate the time evolution of a typical deep convective storm in central Oklahoma (this particular storm is discussed at length in a later chapter). Each panel depicts Doppler radar-derived equivalent reflectivity structure on a vertical, west-east oriented plane centered on the storm core. Storm date and time of each cross-section are indicated in the upper left corner. One important feature is the fairly persistent reflectivity maximum aloft which indicates strong, deep updrafts. Another important feature is the location and behavior of the penetrating

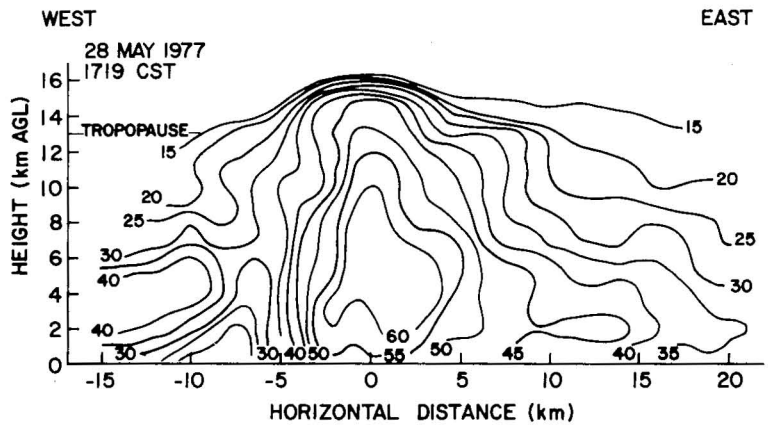

Figure 1. Vertical west-east cross-section through the Wynnewood storm at 1719 CST 28 May 1977. Reflectivity contoured as 10 log (Z). Horizontal coordinate has arbitrary origin.

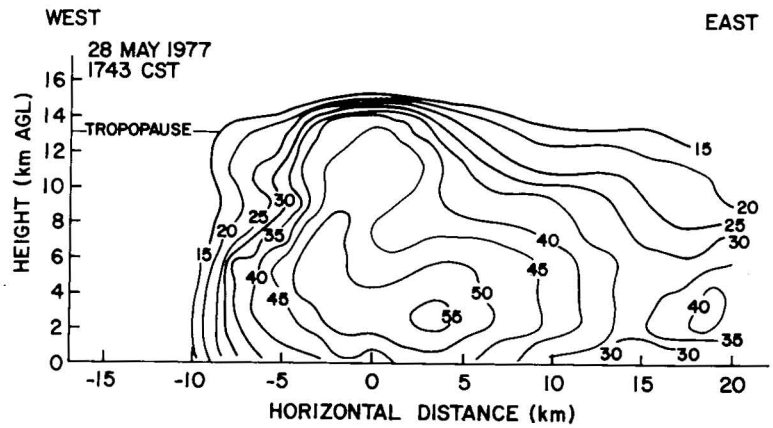

Figure 2. Same as in Fig. 1, but at 1743 CST.

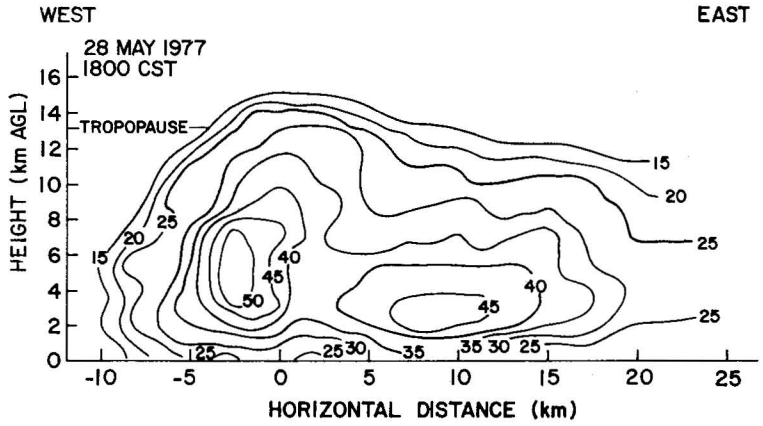

Figure 3. Same as in Fig. 1, but at 1800 CST.

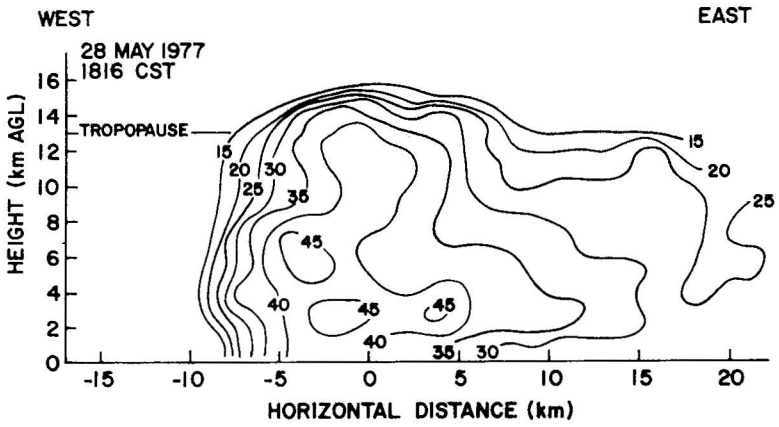

Figure 4. Same as in Fig. 1, but at 1816 CST.

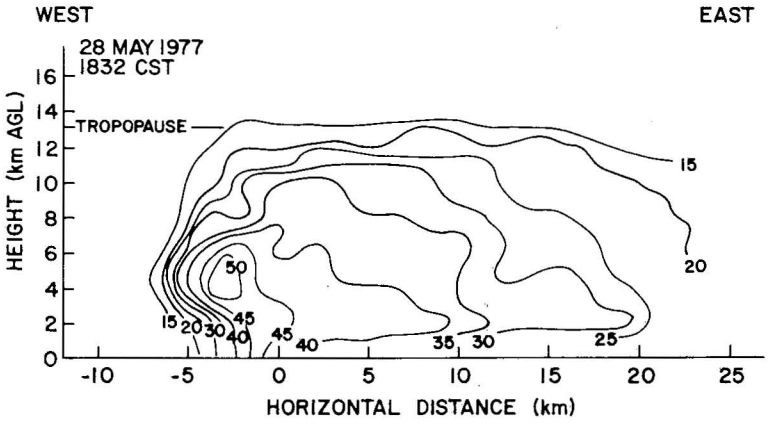

Figure 5. Same as in Fig. 1, but at 1832 CST.

stratospheric tower whose edge is defined by the 15 dBZ contour. This feature is always nearly over the reflectivity maximum and exhibits a pulsating tendency until it subsides to the level of the tropopause by 1832 CST. We may infer that the central updraft extends through the reflectivity maximum aloft to the upper levels of the stratospheric tower core, after the reasoning of Newton (1966). Figure 7 in Newton's paper depicts vertical radar-derived cross-sections spaced in time, of a convective storm with pulsating towers. The shortest apparent period of tower pulsation was approximately 8 minutes with corresponding average vertical motion speed of approximately 5 m s^{-1}. In Figs. 1 through 5, the largest height changes of the tower occurred in the periods 1719-1743 CST and 1816-1832 CST. Largest observed height changes were on the order of 2000 meters which corresponded to an average vertical motion speed of approximately 1.5 m s^{-1}. Greatly reduced time resolution may have prevented the detection of short period large amplitude oscillations. In an effort to determine whether shorter period cloud top oscillations occurred during the 28 May storm, time lapse photographs of the storm taken at NSSL were utilized. Stratospheric tower oscillations near 1530 CST were found to have a period of roughly 5 minutes and associated rise/fall rates in the range of 10-15 m s^{-1}. Similar estimates could not be made at later times because the anvil rapidly expanded to hide cloud top activity. Although the exact relation between motions of radar top and visible top are not known, they may be quite similar. It is hypothesized that these oscillations may be typified by velocities up to 15 m s^{-1}. Since the width of the visible towers was much smaller than the width of the cloud as a whole, a representative storm-top vertical velocity may be one order of magnitude less.

An alternative analysis technique recognizes the importance of incorporating and adjusting for errors. The analysis design is founded on the concept of a modified kinematic method. Horizontal winds are subject to analysis and measurement errors. Consequently, the vertical motion field is derived from horizontal winds adjusted in accord with known error such that the continuity equation and two kinematic boundary conditions are satisfied simultaneously. With the upper boundary condition on vertical motion properly specified, it is hoped that many of the ills attributed to conventionally derived vertical motion fields will be mitigated. The framework of the analysis modification is the strong constraint formalism in the calculus of variations (Sasaki, 1958; Stephens, 1965; Sasaki, 1970), which involves the introduction of a multiplier to increase the number of unknowns and render the analysis problem well-posed. The problem solution is in the form of optimally adjusted horizontal wind components. O'Brien (1970) derived an analytical variational solution for the vertical velocity problem, and applied this technique to mesoscale radiosonde data through the adjustment of horizontal divergence.

An appropriate upper boundary condition is important for maximized accuracy of derived vertical motion. This is particularly true in the upper levels where adjusted vertical velocities are strongly influenced by the boundary value. In a previous discussion we concluded that the assumption of a stationary storm top could be a good approximation. An intuitive consequence of this condition is that in-cloud air motions near storm top must be small. This would lead to the choice of a small value of w on the upper boundary. In this preliminary investigation, we assume that precipitation is floated at altitude. The resulting approximate upper boundary condition is $w = -V_t$.

The choice of a lower kinematic boundary condition is that w is assumed to be zero at the earth's surface. All previous studies using dual Doppler data have included this boundary condition. Maximum vertical velocities at the ground arising from wind flow over sloping or irregular terrain are unlikely to exceed 2 m s^{-1}, while terrain-induced vertical velocities for these studies would be at least one order of magnitude less. Such effects are justifiably negligible in studies of convective storms, where maximum in-cloud vertical velocities are at least two orders of magnitude larger.

2.3 Data Management and Interpolation

Data collected by a pair of pulse Doppler radars are processed and synthesized in post-analysis to obtain storm wind and reflectivity fields. The information gathered by three different radars is employed in this investigation. The first radar is the NSSL Doppler radar located at Max Westheimer Airfield in Norman, Oklahoma. The second radar is the CHILL (University of Chicago and Illinois State Water Survey) Doppler Radar located during the Spring 1977 research program 77.1 km at 246.7° from Norman, near Anadarko, Oklahoma. The third Doppler radar is located at Cimarron Airfield 41.3 km at 310.0° from Norman, near Yukon, Oklahoma. Characteristics of each radar appear in Table 1 while the relative locations of the radars are indicated in Fig. 6. Each radar is equipped with a digital integrator that employs an exponential time weighting function to provide signal power averages. These are recorded on magnetic tape for post-analysis. The NSSL and Cimarron radars both have 762 range gates spaced 150 m apart, while the CHILL radar has 1024 range gates spaced 150 m apart. Doppler data are derived by applying a hardwired processor of the pulse pair algorithm (Sirmans and Bumgarner, 1975) to time series of complex (in-phase I, and quadrature -phase Q) video echoes. Estimated power-weighted spectral means for each range gate are recorded on magnetic tape. In post-analysis, range-normalized equivalent reflectivity and signal-to-noise ratio are retrieved from average power. Data are then reformatted and written on magnetic tape for archival.

Data analysis is divided into three parts. Doppler velocities are checked to determine if aliasing exists, with any detected aliasing corrected. In the next step, Doppler velocities and equivalent reflectivity information for each radar separately are interpolated to a common grid in cylindrical coordinates. The analyst has the option of incorporating the first step into the second step. In the third step, horizontal wind components are first derived from synthesized Doppler velocities obtained from the two radars. As an option, the continuity equation may then be integrated vertically to obtain a conventional vertical wind estimate. Alternatively, a variational adjustment may be performed on the horizontal winds prior to integration of the continuity equation. Cartesian wind components are then computed and interpolated to a suitable Cartesian grid. Lastly, equivalent reflectivities at cylindrical coordinate grid points are directly interpolated to the same Cartesian grid. Analyzed fields are displayed by a variety of graphic techniques to facilitate interpretation.

Prior to objective analysis, aliased Doppler velocities must be detected and corrected. Noisy velocity estimates are removed by thresholding with a minimum signal-to-noise ratio, typically on the order of 5 dB. For a Doppler

Table 1. Characteristics of the Doppler Radars.

	Norman	Cimarron	CHILL
Wavelength (cm)	10.52	10.94	10.94
Peak power (KW)	750	500	600
Pulse length (μs(m))	1(150)	1(150)	1(150)
Half-power beam width (deg)	0.81	0.85	0.95
Nyquist velocity interval (m s^{-1})	±34.2	±35.6	±26.6
PRT (μs)	768	768	1024
Antenna gain (dB) including waveguide and radome transmission loss	44.8	43.2	41.5

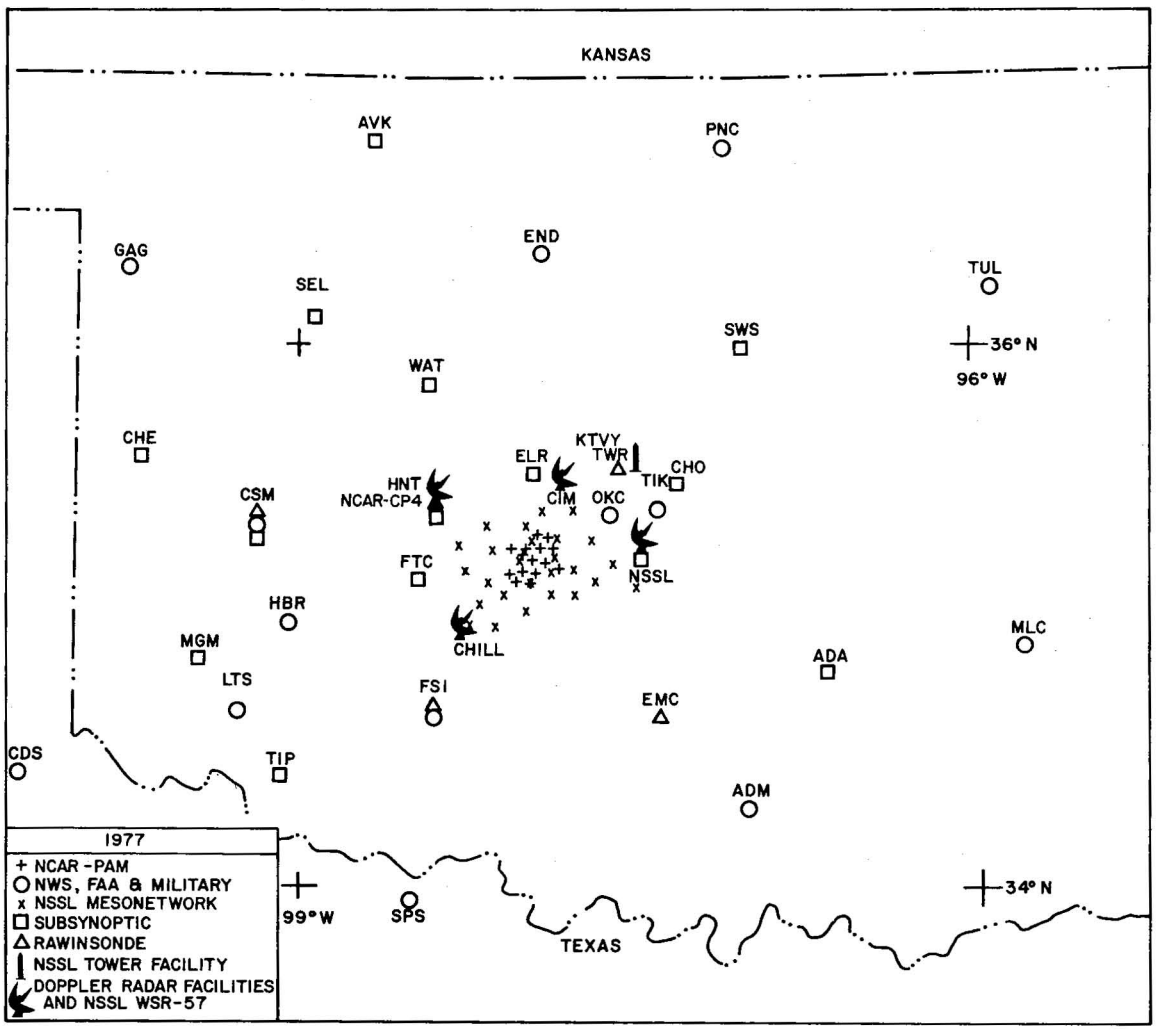

Figure 6. Schematic of radars, surface instrumentation, tower and rawinsonde site locations for the NSSL 1977 Spring Program.

radar with sampling frequency f_s and wavelength of transmitted energy λ, frequencies $>f_s/2$ are aliased into the fundamental Nyquist interval ($\pm f_s/2$) and are interpreted as velocities within $\pm V_{max}(=f_s\lambda/4)$. For the purpose of detecting and correcting such ambiguities, three different methods may be employed for each radial, depending on the expected distribution of velocities in the Nyquist interval. Examination of velocity data from each radar in a range-azimuth format (B-scan) indicates both the spread of velocities within the Nyquist interval and the severity of aliasing. Gate-to-gate velocity differences of order $2V_{max}$ indicate that aliasing is present. When velocity estimates along the radial are quasi-normally distributed and velocities are not aliased throughout the Nyquist interval, the technique of Ray and Ziegler (1977) may be employed. In this method, a histogram of velocities along a radial is constructed and a velocity sub-interval containing quasi-normally distributed velocities is identified. Any velocities well outside of this sub-interval are flagged and corrected for aliasing such that all velocities are then normally distributed. In many severe storm data sets, aliasing is totally absent at low elevation while velocities appear throughout the Nyquist interval at high elevation. This is a consequence of the intense divergence at high levels. In these cases, two alternative techniques are employed to detect aliasing. For low elevation angles, aliased velocities are detected by comparing each velocity along the radial with a truncated Fourier expansion of the entire series of velocities along each radial. Pronounced deviations from the reconstructed model of velocity distributions indicate aliased velocities and corrections are performed on the assumption that multiple aliasing does not exist. The previously described technique may be used as an alternative procedure. In subsequent radial scans, a shear check is employed between velocity estimates both in azimuth (previous radial) and range. Assuming that some initial velocity is not aliased adjacent velocities are flagged if a velocity difference greater than a prescribed threshold of order $2V_{max}$ exists. A flagged velocity will be corrected unless the adjustment results in an unrealistic azimuthal shear. Since the reference velocity must not itself be aliased the first element is compared to the first element of the adjacent radial and adjusted if necessary. In practice, this technique is more cumbersome than the frequency distribution technique, but yields satisfactory results.

In order to solve the finite-difference analysis equations, data in radar spherical coordinates are interpolated to a common analysis grid in cylindrical coordinates. After derivation of wind components and combination of reflectivity estimates from each radar, fields are interpolated to a Cartesian grid. Figure 7 shows the basic characteristics of the nested cylindrical and Cartesian coordinate systems employed in these analyses.

Interpolation is a distance-weighted average of all data contained within a spherical volume whose radius R is of the order of the grid point separation. A Cressman weighting function (Cressman, 1959) of the form

$$W_i = \begin{cases} \dfrac{R^2 - D_i^2}{R^2 + D_i^2} & ; \quad D_i \leq R \\ 0 & ; \quad D_i > R \end{cases}$$

manages the interpolation, where the i'th datum within the influence volume is located a distance D_i from the gridpoint. The weighted gridpoint average of a quantity Q is computed from

$$\overline{Q} = \sum_{i=1}^{N} W_i Q_i \Big/ \sum_{i=1}^{N} W_i \quad ,$$

where N is the total number of data within the averaging volume and Q represent Doppler velocities, reflectivities, or derived Cartesian wind components. This algorithm is not optimal, but yields satisfactory results since Doppler data is rather densely distributed. Due to the large quantity of data to be processed, running sums of weights and weighted data are created as data is read. After all data has been read, the gridpoint average is computed. To avoid data extrapolation at the analysis volume boundaries, the sums of weights at each grid point must be above a prescribed threshold for an analysis variable to be assigned to that gridpoint.

After radar information has been interpolated to common gridpoints, the wind components in ρ - s planes are synthesized. The two Doppler velocity estimates $\overline{V}_1$, $\overline{V}_2$, and the volume mean hydrometeor terminal velocity $\overline{V}_t$ are related to the wind components by

$$U_\rho = \frac{(s+d) r_1 \overline{V}_1 - (s-d) r_2 \overline{V}_2}{2 d \rho} - \overline{V}_t \sin \alpha$$

and

$$U_s = \frac{r_2 \overline{V}_2 - r_1 \overline{V}_1}{2d} \quad ,$$

where U_s is the wind component parallel to the s-axis and U_ρ is the wind component parallel to the ρ-axis. The geometric factors s, d, ρ, r_1, r_2, and α are determined by the position of a gridpoint in the chosen cylindrical coordinate system. Figure 7 illustrates the orientation of this coordinate system with respect to the two radars. A plane of constant α is called a "coplane." Terminal velocity estimates are based on interpolated reflectivity $\overline{Z}$ (Joss and Waldvogel, 1970) and two correction factors. The first correction accounts for changes in terminal velocity due to changes in air density γ (Foote and du Toit, 1969) while the second factor parameterizes the effect of a linearly varying mixture of ice and water within a given layer. The liquid fraction is represented by the $\overline{V}_t$ - $\overline{Z}$ relation and a constant value of $\overline{V}_t$ is imposed in the ice region of the cloud. The complete expression is

$$\overline{V}_t = 2.6\ \overline{Z}^{\,0.107}\left(\frac{\gamma_o}{\gamma}\right)^{0.4} s_1(z) + s_2(z)$$

where the height scales s_1, s_2 take the values

$$s_1(z) = \begin{cases} \dfrac{Z_i - z}{Z_i - Z_\ell} & ;\ Z_\ell \le z \le Z_i \\ 1 & ;\ 0 \le z \le Z_\ell \\ 0 & ;\ Z_i < z \end{cases}$$

$$s_2(z) = \begin{cases} 2\,\dfrac{z - Z_\ell}{Z_i - Z_\ell} & ;\ Z_\ell \le z \le Z_i \\ 2 & ;\ Z_i < z \\ 0 & ;\ 0 \le z \le Z_\ell \end{cases} \quad .$$

The gridpoint altitude is z while Z_ℓ and Z_i are respectively the freezing level and some high level where the cloud condensate is assumed to be entirely in the ice phase. For storms studied here, $Z_\ell \sim$ 5 km and $Z_i \sim$ 10 km.

2.4 Variational Optimization Method

The mass continuity equation in anelastic form, the fundamental kinematic constraint employed in the variational and conventional analyses utilized in this thesis, may be expressed in vector notation as

$$\nabla_3 \cdot \gamma\vec{U} = 0 \quad . \tag{1}$$

In these analyses, the wind vector is determined in a cylindrical coordinate system natural to the two radars. Interpolation to a Cartesian grid follows computation of Cartesian wind components. Equation (1) is written for cylindrical coordinates as

$$\frac{\partial}{\partial s}(\gamma U_s) + \frac{1}{\rho}\frac{\partial}{\partial \rho}(\rho\gamma U_\rho) + \frac{1}{\rho}\frac{\partial}{\partial \alpha}(\gamma U_\alpha) = 0 \quad . \tag{2}$$

The continuity Eq. (2) may be written in expanded form as

$$\underset{1}{\frac{\partial}{\partial s}(\gamma U_s)} + \underset{2}{U_s \frac{\partial}{\partial s}(\ell n\gamma)} + \underset{3}{\frac{1}{\rho}\frac{\partial}{\partial \rho}(\rho U_\rho)} + \underset{4}{U_\rho \frac{\partial}{\partial \rho}(\ell n\gamma)} + \underset{5}{\frac{1}{\rho}\frac{\partial}{\partial \alpha}(U_\alpha)}$$

$$+ \underset{6}{\frac{1}{\rho} U_\alpha \frac{\partial}{\partial \alpha}(\ell n\gamma)} = 0 \quad . \qquad (3)$$

Consider the task of scaling the terms numbered 1 through 6 in Eq. (3). Since Eq. (3) will be applied to kinematic fields obtained by remote sensing of deep convection, representative spatial scales for the disturbance and orientation of the sensor relative to the disturbance, must be specified. Temporal scales need not be specified since Eq. (3) is diagnostic in the wind components U_s, U_ρ, and U_α. We adopt the density profile of the undisturbed environment to estimate order of magnitude of the within-cloud profile, hence horizontal density variations will be scaled much smaller than vertical variations. The scales are:

$P \sim 5 \times 10^4$ m,

$\delta s \sim \delta\rho \sim 5 \times 10^3$ m,

$\delta\alpha \sim 5° \sim 10^{-1}$ radian,

$D \sim 10^4$ m

$L \sim \delta s, \delta\rho$ (length scale),

$U_\alpha \lesssim U_s \sim U_\rho \sim 10$ m s^{-1},

$\gamma \sim 1$ kg m^{-3},

$\delta_z \ell n\gamma \sim 1$,

$K_z = \frac{\partial}{\partial z}(\ell n\gamma) \sim \frac{1}{D}\delta_z \ell n\gamma \sim 1 \times 10^{-4}$,

$K_\alpha = \frac{1}{\rho}\frac{\partial}{\partial \alpha}(\ell n\gamma) \sim K_z\cos(\alpha) \sim K_z\cos(\delta\alpha) \sim K_z \sim 1 \times 10^{-4}$,

$K_\rho \sim \frac{\partial}{\partial \rho}(\ell n\gamma) \sim K_z\cos(90-\alpha) \sim 1 \times 10^{-5}$.

Evaluate term-by-term orders of magnitude:

Term 1 - $\frac{\partial}{\partial s}(U_s) \sim \frac{1}{L} U_s \sim 2 \times 10^{-3}$,

Term 2 - $U_s \frac{\partial}{\partial s}(\ell n\gamma) \sim 0$,

Term 3 - $\frac{1}{\rho}\frac{\partial}{\partial\rho}(\rho U_\rho) \sim \frac{1}{L}U_\rho \sim 2 \times 10^{-3}$,

Term 4 - $U_\rho\frac{\partial}{\partial\rho}(\ell n\gamma) \sim K_\rho U_\rho \sim 10^{-4}$,

Term 5 - $\frac{1}{\rho}\frac{\partial}{\partial\alpha}(U_\alpha) \sim \frac{1}{P\delta\alpha}U_\alpha \lesssim 2 \times 10^{-3}$,

Term 6 - $\frac{1}{\rho}U_\alpha\frac{\partial}{\partial\alpha}(\ell n\gamma) \sim K_\alpha U_\alpha \lesssim 10^{-3}$.

We adopt a first-order approximation of Eq. (3) by retaining terms 1, 3, 5, and 6. This approximation is justified since for the given scales, the α-component of the wind is quasi-vertical. Hence, the s- and ρ-components of mass advection are small compared to the α-component. After replacing the α-gradient of log-density by the constant κ, the approximate equation of mass continuity takes the final form

$$\frac{\partial}{\partial s}(U_s) + \frac{1}{\rho}\frac{\partial}{\partial\rho}(\rho U_\rho) + \frac{\kappa}{\rho}U_\alpha + \frac{1}{\rho}\frac{\partial}{\partial\alpha}(U_\alpha) = 0 \quad . \tag{4}$$

In finite-difference form using centered differences, Eq. (4) is written as

$$D_\alpha + \frac{\kappa(U_{\alpha-1/2} + U_{\alpha+1/2})}{2\rho} + \frac{U_{\alpha+1/2} - U_{\alpha-1/2}}{\rho\Delta\alpha} = 0 \quad , \tag{5}$$

where $D_\alpha \equiv$ horizontal divergence (in tilted planes)

$$= [(U_s)_{i+1} - (U_s)_{i-1}] \Big/ 2\Delta s + [(\rho U_\rho)_{j+1} - (\rho U_\rho)_{j-1}] \Big/ 2\rho\Delta\rho \ .$$

In recursive form:

$$U_{\alpha+1/2} = \left[\frac{(\rho\Delta\alpha)^{-1} - \kappa(2\rho)^{-1}}{(\rho\Delta\alpha)^{-1} + \kappa(2\rho)^{-1}}\right]U_{\alpha-1/2} - D_\alpha\left[(\rho\Delta\alpha)^{-1} + \kappa(2\rho)^{-1}\right]^{-1} \quad . \tag{5a}$$

For the purposes of the variational analysis, the continuity equation is vertically integrated through the storm depth, i.e.,

$$\int_\alpha \left[D_\alpha + \frac{\kappa}{\rho}U_\alpha + \frac{1}{\rho}\frac{\partial}{\partial\alpha}(U_\alpha)\right] d\alpha = 0 \quad .$$

In finite-difference form the integral is replaced by a vertical sum (quadrature) which is written as

$$\sum_{k=1}^{km} D_k + \sum_{k=1}^{km} C_1 U_{\alpha+1/2} - C_2 U_{\alpha-1/2} = 0 \quad , \tag{6}$$

where

$$C_1 = \frac{\kappa}{2\rho} + \frac{1}{\rho\Delta\alpha} > 0 \text{ and } C_2 = \frac{1}{\rho\Delta\alpha} - \frac{\kappa}{2\rho} > 0 \quad ,$$

and the index km is the number of grid levels in the vertical. Expanding the second L.H.S. sum and using the index relation $\alpha = k-1$, there follows

$$\sum_{k=1}^{km} C_1 U_{\alpha+1/2} - C_2 U_{\alpha-1/2}$$

$$= (C_1 U_{1/2} - C_2 U_{-1/2}) + (C_1 U_{1+1/2} - C_2 U_{1/2})$$

$$+ \ldots + (C_1 U_{\alpha_{max}+1/2} - C_2 U_{\alpha_{max}-1/2})$$

$$= -C_2 U_{-1/2} + C_1 U_{\alpha_{max}+1/2}$$

$$+ (C_2-C_1)(U_{1/2} + U_{1\ 1/2} + \ldots + U_{\alpha_{max}-1/2}).$$

Since $C_2 - C_1 \sim \frac{\kappa}{\rho} \sim 10^{-4}$ and the sum of U_α is less than or of order 10^2, the third r.h.s. term is less than or of order 10^{-2}. For $U_\alpha \gtrsim 1$, the first two r.h.s. terms are at least of order 10^{-3}. In general, the last term is not negligible. However, since we desire a constraint with vertical motion implicit only, we will adopt the incompressible continuity equation in these studies. To retain the anelastic form, an iterative solution would be required since the kinematic constraint Eq. (6) involves vertical velocities within upper and lower boundaries. We may then write

$$\sum_{k=1}^{km} D_k = C_2 U_{-1/2} - C_1 U_{\alpha_{max}+1/2} \quad .$$

The lower kinematic boundary condition is $(U_\alpha)_{-1/2} = 0$. Here we have assumed that the earth's surface essentially coincides with the -0.5 deg coplane. For convenience we assume that $U_{\alpha_{max}} = U_{\alpha_{max}+1/2}$. We may then write

$$\sum_{k=1}^{km} D_k + C_1 U_{\alpha_{max}} = 0 \tag{7}$$

as the final form of the continuity equation in integral form.

The vertical Cartesian wind component U_z is related to the cylindrical components U_ρ and U_α by the transformation

$$U_z = w = U_\rho \sin(\alpha) + U_\alpha \cos(\alpha)$$

where α is coplane elevation angle. Solving for U_α, we obtain

$$U_\alpha = w/\cos(\alpha) - U_\rho \tan(\alpha)$$

By employing a suitable estimate of w at storm volume top and inserting an observed value of U_ρ at the same point, we may compute the appropriate kinematic upper boundary condition in the cylindrical coordinate system.

The initial phase of the objective analysis manages the derivation of U_s (baseline) and U_ρ (radial) air motion components at regularly spaced gridpoints, in a series of coplanes evenly spaced from local horizontal upwards. This 3-dimensional array of gridpoints constitutes the analysis domain S. It is desired to adjust U_s and U_ρ at all interior points in S in an optimum least-squares sense so that the constraining relation (7) is exactly satisfied throughout S. A solution of this problem is obtained by applying theory of the calculus of variations. First define the functional

$$I = \int_\sigma \int_\alpha \left[\tilde{\alpha}(\tilde{U}_s - \tilde{U}_s)^2 + \tilde{\beta}(U_\rho - \tilde{U}_\rho)^2 + \lambda\, G(U_s, U_\rho, U_\alpha)\right] d\alpha d\sigma \quad , \qquad (8)$$

where G is the mass continuity given in Eq. (4), $\tilde{\alpha}$ and $\tilde{\beta}$ are observational weights having specified functional dependence on space variables, U_s and U_ρ are wind components to be adjusted, and λ is the lagrange multiplier. A tilde (~) denotes a quantity which is already known throughout the given region of interest. If the extremals U_s and U_ρ exist, these functions will uniquely and exactly satisfy G at least in the interior of the region of interest. In finite difference form the functional is presented as

$$I = \sum_{i=i\ell}^{ih} \sum_{j=j\ell}^{jh} \sum_{k=1}^{km} \tilde{\alpha}(U_s - \tilde{U}_s) + \tilde{\beta}(U_\rho - \tilde{U}_\rho)^2 + \lambda G'(U_s, U_\rho, U_\alpha) \quad , \qquad (9)$$

where summation replaces integration and the region of interest is the gridpoint domain S. The boundary surface defined by the summation limits, $i\ell$, ih, $j\ell$, jh, and km is generally irregular. All quantities in Eq. (9) are analogous to those in Eq. (8) except that they are defined at discrete gridpoints. G' is the continuity equation in finite-difference form, Eq. (5). Now assume $\lambda = \lambda(s,\rho)$. We can rearrange the vertical summation in Eq. (9) and apply the integral constraint Eq. (7) to obtain an equivalent form of the finite-difference functional, i.e.,

$$I = \sum_{i=i\ell}^{ih} \sum_{j=j\ell}^{jh} \sum_{k=1}^{km} \tilde{\alpha}(U_s - \tilde{U}_s)^2 + \tilde{\beta}(U_\rho - \tilde{U}_\rho)^2$$

$$+ \sum_{i=i\ell}^{ih} \sum_{j=j\ell}^{jh} \lambda \sum_{k=1}^{km} \left[\nabla_s U_s + \frac{1}{\rho} \nabla_\rho (\rho U_\rho)\right] + F \qquad (10)$$

where $F = C_1 U_\alpha(k=km)$. The centered difference approximation used to evaluate the first derivative in the s and ρ directions is, respectively,

$$\nabla_s \phi_{i,j} = \frac{1}{2d} (\phi_{i+1,j} - \phi_{i-1,j}) \equiv \frac{1}{2d} \Psi_s \phi$$

and

$$\nabla_\rho \phi_{i,j} = \frac{1}{2d} (\phi_{i,j+1} - \phi_{i,j-1}) \equiv \frac{1}{2d} \Psi_\rho \phi \quad . \tag{10a}$$

The identities in Eqs. (10a) define the symbols Ψ_s and Ψ_ρ. The extremals of the functional Eq. (10) may be determined if it is stationary and if the first variation of (10) vanishes. The latter condition is expressed as

$$\delta I = \sum_{i=i\ell}^{ih} \sum_{j=j\ell}^{jh} \sum_{k=1}^{km} 2\tilde{\alpha}(U_s - \tilde{U}_s)\delta U_s + 2\tilde{\beta}(U_\rho - \tilde{U}_\rho)\delta U_\rho$$

$$+ \sum_{i=i\ell}^{ih} \sum_{j=j\ell}^{jh} \lambda \sum_{k=1}^{km} \nabla_s \delta U_s + \frac{1}{\rho}\nabla_\rho(\rho \delta U_\rho)$$

$$+ \sum_{i=i\ell}^{ih} \sum_{j=j\ell}^{ih} \delta\lambda \sum_{k=1}^{km} [\nabla_s U_s + \frac{1}{\rho}\nabla_\rho(\rho U_\rho)] + F \quad = 0. \tag{11}$$

Now commute the sums S1 and S2 where

$$S1 = \sum_{i=i\ell}^{ih} \sum_{j=j\ell}^{jh} \sum_{k=1}^{km} \lambda_{i,j} \Psi_s(\delta U_s)_{i,j}$$

and

$$S2 = \sum_{i=i\ell}^{ih} \sum_{j=j\ell}^{jh} \sum_{k=1}^{km} \lambda_{i,j} \frac{1}{\rho_j} \Psi_\rho(\rho \delta U_\rho)_{i,j}$$

Consider first the commutation of the sum S1. Expanding and rearranging of terms gives

$$\sum_{i=i\ell}^{ih} \sum_{j=j\ell}^{jh} \sum_{k=1}^{km} \lambda_{i,j} \Psi_s(\delta U_s)_{i,j}$$

$$= \sum_{j=j\ell}^{jh} \sum_{k=1}^{km} \lambda_{i\ell,j}(\delta U_{i\ell+1,j} - \delta U_{i\ell-1,j}) + \lambda_{i\ell+1,j}(\delta U_{i\ell+2,j} - \delta U_{i\ell,j})$$

$$+ \ldots + \lambda_{ih-1,j}(\delta U_{ih,j} - \delta U_{ih-2,j}) + \lambda_{ih,j}(\delta U_{ih+1,j} - \delta U_{ih-1,j})$$

$$= -\sum_{j=j\ell}^{jh} \sum_{k=1}^{km} \delta U_{i\ell+1,j}(\lambda_{i\ell+2,j} - \lambda_{i\ell,j}) + \delta U_{i\ell+2,j}(\lambda_{i\ell+3,j} - \lambda_{i\ell+1,j})$$

$$+ \ . \ . \ . + \delta U_{ih-2,j}(\lambda_{ih-1,j} - \lambda_{ih-3,j}) + \delta U_{ih-1,j}(\lambda_{ih,j} - \lambda_{ih-2,j})$$

$$+ \{\text{uncommutable terms}\}_i \ .$$

The uncommutable terms in the index i are

$$\sum_{j=j\ell}^{jh} \sum_{k=1}^{km} -\lambda_{i\ell,j}\, \delta U_{i\ell-1,j} - \lambda_{i\ell+1,j}\, \delta U_{i\ell,j} + \lambda_{ih-1,j}\, \delta U_{ih,j} + \lambda_{ih,j}\, \delta U_{ih+1,j}$$

where subscript s has been suppressed on some of the above terms for convenience.

The commutation of the sum S1 takes the final form

$$\sum_{i=i\ell}^{ih} \sum_{j=j\ell}^{jh} \sum_{k=1}^{km} \lambda_{i,j}\, \nabla_s (\delta U_s)_{i,j}$$

$$= - \sum_{i=i\ell+1}^{ih-1} \sum_{j=j\ell}^{jh} \sum_{k=1}^{km} \nabla_s \lambda_{i,j} (\delta U_s)_{i,j} + \{\text{uncommutable terms}\}_i .$$

A similar manipulation for the commutation of the sum S2 yields

$$\sum_{i=i\ell}^{ih} \sum_{j=j\ell}^{jh} \sum_{k=1}^{km} \frac{\lambda_{i,j}}{\rho_j} \nabla_\rho (\rho \delta U_\rho)$$

$$= - \sum_{i=i\ell}^{ih} \sum_{j=j\ell+1}^{jh-1} \sum_{k=1}^{km} \rho_j \nabla_\rho \frac{\lambda_{i,j}}{\rho_j} (\delta U_\rho)_{i,j} + \{\text{uncommutable terms}\}_j \ ,$$

where the uncommutable terms in the index j are

$$\sum_{i=i\ell}^{ih} \sum_{k=1}^{km} -(\rho \delta U_\rho)_{i,j\ell-1} \frac{\lambda_{i,j}}{\rho_{j\ell}} - (\rho \delta U_\rho)_{i,j\ell} \frac{\lambda_{i,j+1}}{\rho_{j+1}}$$

$$+ (\rho \delta U_\rho)_{i,jh+1} \frac{\lambda_{i,jh}}{\rho_{jh}} + (\rho \delta U_\rho)_{i,jh} \frac{\lambda_{i,jh-1}}{\rho_{jh-1}} \ .$$

The first variation of I as expressed by Eq. (11) may now be written as

$$\sum_{i=i\ell}^{ih}\sum_{j=j\ell}^{jh}\sum_{k=1}^{km} 2\tilde{\alpha}(U_s-\tilde{U}_s)\,\delta U_s + 2\tilde{\beta}(U_\rho-\tilde{U}_\rho)\delta U_\rho$$

$$-\sum_{i=i\ell+1}^{ih}\sum_{j=j\ell}^{jh}\sum_{k=1}^{km} \nabla_s\lambda\,\delta U_s - \sum_{i=i\ell}^{ih}\sum_{j=j\ell+1}^{jh}\sum_{k=1}^{km} \rho\nabla_\rho\frac{\lambda}{\rho}\,\delta U_\rho$$

$$+\sum_{i=i\ell}^{ih}\sum_{j=j\ell}^{jh}\left\{\sum_{k=1}^{km}\left(\nabla_s U_s + \frac{1}{\rho}\nabla_\rho(\rho U_\rho)\right) + F\right\}\delta\lambda$$

$$+ \{\text{uncommutable terms}\}_i + \{\text{uncommutable terms}\}_j = 0 \quad .$$

It is desirable to bring the first three summed quantities above under a "common summation sign". For convenience we will adopt a subscript convention to identify boundary terms while rearranging terms in the above expression. This subscript notation, to be associated with the last five bracketed terms below, will indicate the set of gridpoints at which each term applies; e.g. $[(A)]_{i=i\ell,ih\}j,k}$ is interpreted as "term A appears at gridpoints where index i equals $i\ell$ or ih and a summation of term A is carried through all values of indices j and k". The first variation of I may then be re-expressed as

$$\sum_{i=i\ell+1}^{ih-1}\sum_{j=j\ell+1}^{jh-1}\sum_{k=1}^{km}\left(2\tilde{\alpha}(U_s-\tilde{U}_s) - \nabla_s\lambda\right)\delta U_s + \left(2\tilde{\beta}(U_\rho-\tilde{U}_\rho) - \rho\nabla_\rho\frac{\lambda}{\rho}\right)\delta U_\rho$$

$$+\sum_{i=i\ell+1}^{ih-1}\sum_{j=j\ell+1}^{jh-1}\left\{\sum_{k=1}^{km}\left(\nabla_s U_s + \frac{1}{\rho}\nabla_\rho(\rho U_\rho)\right) + F\right\}\delta\lambda + \{\text{uncommutable term in i,j}\}$$

$$+\left(2\tilde{\alpha}(U_s-\tilde{U}_s)\delta U_s\right)_{\substack{i=i\ell,ih\\ j=j\ell,jh\}k}} + \left(2\tilde{\beta}(U_\rho-\tilde{U}_\rho)\delta U_\rho\right)_{\substack{i=i\ell,ih\\ j=j\ell,jh\}k}}$$

$$+\left(-\nabla_s\lambda\,\delta U_s\right)_{j=j\ell,jh\}i,k} + \left(-\rho\nabla_\rho\frac{\lambda}{\rho}\,\delta U_\rho\right)_{i=i\ell,ih\}j,k}$$

$$+\left\{\left\{\sum_{k=1}^{km}\left(\nabla_s U_s + \frac{1}{\rho}\nabla_\rho(\rho U_\rho)\right) + F\right\}\delta\lambda\right\}_{\substack{i=i\ell,ih\\ j=j\ell,jh}} = 0 \quad .$$

All terms not under summation are the boundary terms in the problem. It is desirable for these terms to vanish identically. Employing so-called natural boundary conditions on λ, we specify

$$\lambda_{i\ell,j} = \lambda_{i\ell+1,j} = \lambda_{ih-1,j} = \lambda_{ih,j} = 0 \quad ,$$

and

$$\lambda_{i,j\ell} = \lambda_{i,j\ell+1} = \lambda_{i,jh-1} = \lambda_{i,jh} = 0 \quad .$$

To complete the set of boundary conditions we further specify that the variations of the fields U_s and U_ρ vanish on the lateral boundaries, i.e.,

$$(\delta U_s, \delta U_\rho)_{i\ell,j} = (\delta U_s, \delta U_\rho)_{ih,j} = (\delta U_s, \delta U_\rho)_{i,j\ell} = (\delta U_s, \delta U_\rho)_{i,jh} = 0 \quad .$$

Further note that since λ is specified on the outer two lateral boundaries, it follows that the variation of λ is zero at the same points where λ is specified. The condition of vanishing wind component variations on the lateral boundaries implies that the values of observed winds $\tilde{U}_s$ and $\tilde{U}_\rho$ and the functionals U_s and U_ρ on the lateral boundaries are identical. With these boundary conditions assumed, all boundary terms vanish identically. In appropriately simplified form the first variation of I is written as

$$\sum_{i=i\ell+1}^{ih-1} \sum_{j=j\ell+1}^{jh-1} \sum_{k=1}^{km} \left(2\tilde{\alpha}(U_s-\tilde{U}_s)-\nabla_s\lambda\right)\delta U_s + \left(2\tilde{\beta}(U_\rho-\tilde{U}_\rho)-\rho\nabla_\rho\frac{\lambda}{\rho}\right)\delta U_\rho$$

$$+\left[\sum_{k=1}^{km}\left(\nabla_s U_s + \frac{1}{\rho}\nabla_\rho(\rho U_\rho)\right) + F\right]\delta\lambda = 0 \quad . \tag{12}$$

Now δU_s and δU_ρ are arbitrary everywhere in S except on the lateral boundaries, while $\delta\lambda$ is arbitrary everywhere in S except on the outer two grid surfaces. In order to satisfy Eq. (12) at all points in V except on lateral boundaries given variation conditions, it follows that

$$2\tilde{\alpha}(U_s-\tilde{U}_s) - \nabla_s\lambda = 0 \tag{13}$$

and

$$2\tilde{\beta}(U_\rho-\tilde{U}_\rho) -\rho\nabla_\rho\frac{\lambda}{\rho} = 0 \quad , \tag{14}$$

while at all points in S except on outer two grid surfaces (given variation conditions)

$$\sum_{k=1}^{km}\left(\nabla_s U_s + \frac{1}{\rho}\nabla_\rho(\rho U_\rho)\right) + F = 0 \tag{15}$$

which is the recovered constraint Eq. (7). Equations (13) and (14) are the so-called Euler-Lagrange equations. Note that although vertically summed divergences of observed winds may be obtained at points just inside the lateral boundaries, we are not guaranteed that the constraint, Eq. (7), will also be met at these points. This is true because the third term in Eq. (12) vanishes identically through the assumption of natural boundary conditions, irrespective of whether or not the constraint is in fact satisfied. Substitution of Eq. (13) and Eq. (14) into Eq. (12) allows for the elimination of U_s and U_ρ, and the equation for λ can be derived. After performing the substitution and rearranging terms we can write

$$\sum_{k=1}^{km} \nabla_s \frac{1}{2\tilde{\alpha}} \nabla_s\lambda + \frac{1}{\rho}\nabla_\rho \frac{\rho^2}{2\tilde{\beta}}\nabla_\rho \frac{\lambda}{\rho} = -\left[\sum_{k=1}^{km}\left(\nabla_s U_s + \frac{1}{\rho}\nabla_\rho(\rho U_\rho)\right) + F\right] \tag{16}$$

This equation is elliptic and has non-constant coefficients which are proportional to geometric factors and the so-called Gauss precision moduli, defined as (Whittaker and Robinson, 1944)

$$\tilde{\alpha} = \frac{1}{2\sigma_s^2} \text{ and } \tilde{\beta} = \frac{1}{2\sigma_\rho^2} \quad ,$$

where σ_s^2 and σ_ρ^2 are error variances of the radar derived s- and ρ- wind components, respectively. In this paper, these are computed from the expressions (Doviak et al., 1976)

$$\sigma_s^2 = \frac{\sigma_v^2(r_1^2+r_2^2)}{4d^2}$$

and

$$\sigma_\rho^2 = \frac{\sigma_v^2[r_1^2(s+d)^2 + r_2^2(s-d)^2]}{4d^2\rho^2} + \sigma_t^2 \sin^2\alpha \quad ,$$

where σ_v^2 is the assumed error variance of the independent Doppler velocity estimates, σ_t^2 is the error variance associated with the terminal velocity estimate, d is grid separation, and r_1 and r_2 are slant ranges from radars 1 and 2 to the target. Note that we have not included other possible sources of error variance as discussed in Section 2.2.

Using the definitions of the central-difference operator in Eqs. (10a), the finite-difference forms of the various analysis equations are written as follows:

Euler-Lagrange equations:

$$(U_s)_{i,j} = (\tilde{U}_s)_{i,j} + \frac{1}{4\tilde{\alpha}d}(\lambda_{i+1,j} - \lambda_{i-1,j}) \tag{17}$$

$$(U_\rho)_{i,j} = (\tilde{U}_\rho)_{i,j} + \frac{1}{4\tilde{\beta}d}(\lambda_{i,j+1} - \lambda_{i,j-1}) \tag{18}$$

Elliptic equation in λ:

$$(\lambda_{i+2,j} - \lambda_{i,j})\left(\sum_{k=1}^{km} \frac{1}{2\tilde{\alpha}}\right)_{i+1,j} - (\lambda_{i,j} - \lambda_{i-2,j})\left(\sum_{k=1}^{km} \frac{1}{2\tilde{\alpha}}\right)_{i-1,j}$$

$$+ \frac{\rho_{j+1}^2}{\rho_j}\left(\frac{\lambda_{i,j+2}}{\rho_{j+2}} - \frac{\lambda_{i,j}}{\rho_j}\right)\left(\sum_{k=1}^{km} \frac{1}{2\tilde{\beta}}\right)_{i,j+1} - \frac{\rho_{j-1}^2}{\rho_j}\left(\frac{\lambda_{i,j}}{\rho_j} - \frac{\lambda_{i,j-2}}{\rho_{j-2}}\right)\left(\sum_{k=1}^{km} \frac{1}{2\tilde{\beta}}\right)_{i,j-1}$$

$$+ 4d^2\left\{\sum_{k=1}^{km}\left[\nabla_s \tilde{U}_s + \frac{1}{\rho}\nabla_\rho(\rho\tilde{U}_\rho)\right] + F\right\}_{i,j} = 0 \quad . \tag{19}$$

Equation (7) is the constraining relationship written in finite-difference form.

Equation (19) is elliptic in λ, and must only be solved once for each (i,j) during program execution. The successive over-relaxation (SOR) technique has been chosen for obtaining the solution from Eq. (19) because of its simplicity. The expression has non-constant coefficients, reducing rate of convergence slightly. On successive passes, values of λ at each (i,j) are adjusted by adding a fraction of the gridpoint residual, R, obtained by evaluating Eq. (19). The new gridpoint estimate $\lambda^{n+1}_{i,j}$ is related to the previous estimate $\lambda^{n}_{i,j}$ by the expression

$$\lambda^{n+1}_{i,j} = \lambda^{n}_{i,j} + \left(\frac{\alpha}{\beta_{i,j}}\right) R_{i,j} \quad ,$$

where α is the over-relaxation factor and the quantity β is computed from the relation

$$\beta_{i,j} = \left(\sum_{k=1}^{km} \frac{1}{2\tilde{\alpha}}\right)_{i+1,j} + \left(\sum_{k=1}^{km} \frac{1}{2\tilde{\alpha}}\right)_{i-1,j} + \frac{\rho^2_{j+1}}{\rho^2_j}\left(\sum_{k=1}^{km} \frac{1}{2\tilde{\beta}}\right)_{i,j+1} + \frac{\rho^2_{j-1}}{\rho^2_j}\left(\sum_{k=1}^{km} \frac{1}{2\tilde{\beta}}\right)_{i,j-1}.$$

Since the sum terms are ordinarily larger than unity and geometric factors are greater than or of order unity, β for these integrations is typically larger than 4, which is appropriate for a Poisson-type elliptic equation. Based upon experimentation, a value of $\alpha = 1.3$ was used in this analysis.

Before Eqs. (17-19) can be solved, the lateral and upper boundaries of the analysis domain must be identified and flagged. A projection of the interior of the storm volume containing wind measurements is first generated on a horizontal plane. For fixed values of the quasi-horizontal indices i and j, a routine counts the number of levels in the vertical (denoted by K') at which horizontal divergences may consecutively be computed from the ground upwards. The largest value of K so determined at each gridpoint in i and j, is a first estimate of the analysis volume extent and is stored. At each array location where a non-zero K' value cannot be determined, the array element is assigned a value of zero. In the next step, the considerations of where it is prudent to specify an upper boundary condition (and vice versa) are imposed in the following semi-objective manner. The height above ground level (AGL), denoted $h_{i,j}$, is computed for each non-zero value of K'. The height $h_{i,j}$ is equivalent to the radar-visible storm top. A flag parameter F is computed from the expression $F = H_t - \tau H_t$, where H_t is the tropopause height and τ is a tolerance parameter. The parameter τ is subjectively chosen less than 0.2. For stronger and deeper convection, F is closer to H_t because the tropopause is expected to act (more or less) as a "lid" of convection in these cases. The height $h_{i,j}$ is compared to F at all points. When $h_{i,j} < F$, K' is set to zero. Effectively, the analysis will be limited to storm regions where a convective column significantly interacts with the tropopause. For columns of shallow or intermediate extent, no adjustment is performed since the chosen upper boundary condition is unlikely to apply. The upper boundary level is now defined by non-zero values of K'. The set of gridpoints for which K' = 0, adjacent to the closed region(s) for which

K' = 0, are lateral boundary points. Since non-zero elements of K' are not confined to a rectangular domain in general, the boundaries are expected to be irregular. The forcing function (fifth l.h.s. term in Eq. (19)) is computed by summing the quasi-horizontal divergences of observed winds vertically using the index K'(i,j) for the upper limit. Inspection of Eq. (19) indicates that λ varies only at points at least 2Δ grid units inside the lateral boundaries. The forcing function need be computed only at these points. The λ field may then be determined by solving Eq. (19) by the SOR technique already described.

Adjusted wind components are computed from observed winds, observational weights, and the λ field via Eq. (17) and Eq, (18). The vertical or α-component is determined from adjusted s- and ρ-components by integrating the continuity Eq. (5) upward from the specified lower boundary condition. Lastly, and as in the conventional wind analysis, the Cartesian wind components u, v, and w are computed and spatially interpolated to the Cartesian grid. The origin and x-axis of the Cartesian grid are, for convenience, coincident with those features of the cylindrical coordinate analysis grid (Fig. 7). The Cartesian wind field will not exactly satisfy the three-dimensional continuity equation at each gridpoint due to interpolation error. A variational algorithm can easily be designed and implemented to correct this deficiency, if desired. Appendix C presents such an algorithm, for reference purposes. Since accuracy of vertical velocities would not be improved by this additional step, it is not employed in this research.

2.5 Analysis Response

Spectral modification of data fields occurs during the interpolation and variational adjustment phases of the objective analysis. The response function for gridpoint adjustment is unknown. The determination of an appropriate power transfer function is complicated because a gridpoint adjustment is not solely dependent on local wind field characteristics. Experimental evidence indicates that the variational adjustment results in a systematic, modest reduction in overall variance of the U_s and U_ρ fields. Explicit low-pass filtering terms, such as those used by Wagner (1971) and McGinley (1973), are not included in the formalism. Interpolation by a distance-dependent weighting

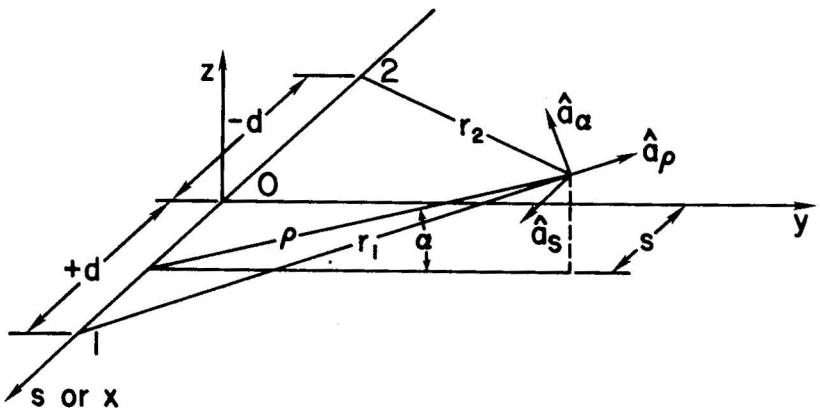

Figure 7. Cylindrical/ Cartesian coordinate systems used for dual-Doppler analysis. The radars are located at the points 1 and 2, and a_ρ, a_s, a_α are the unit normals defining the three velocity component's direction.

function acts as a low-pass spectral filter of the data field. Stephens (1967) discussed the discrete filtering response of the Cressman weight function assuming continuous data fields. He noted that, because of the discrete random nature of an actual data distribution, aliasing errors due to negative side lobes of the weighting function beyond its cutoff could be significant. Analyses of spectral modification is more difficult if irregular distribution of data locations is considered. Stephens and Polan (1971) have determined an expected form for the interpolation power transfer function for two dimensional fields, assuming the Cressman weight function and a random data distribution. Based on the successive corrections method, truncated after one pass and considering a null guess field, they obtained an estimated power transfer function for R (influence radius) = 1.75d (average separation of data locations). Their result is reproduced in Fig. (8). Assuming $d = \Delta x$ and $R = 1.75\,\Delta x$, it is apparent that waves shorter than $5\Delta x$ are damped considerably by interpolation. Waves between $2\Delta x$ and $3\Delta x$ are virtually eliminated. In these studies, $d \sim 0.70\Delta x$ and $R \sim 1.0\Delta x \sim 1.4d$. In spite of the differing values of R and d, and the fact that interpolation is actually 3-dimensional in these studies, the appropriate power transfer functions are probably quite similar. Results shown by Stephens and Stitt (1970) indicate that the random distribution model can successfully be applied to real data distributions. Doviak et al. (1976) obtained an approximate expression for normalized variance reduction resulting from application of the Cressman weighting function within a spherical influence volume of radius r_0. Assuming uniform data spacing Δd, the expression is

$$(1 - R^2)^{1/2} = \frac{0.64}{(r_0/\Delta d)^{3/2}}$$

where R^2 is the normalized variance reduction. The equation is approximate for $r_0/\Delta d < 1.5$. For one interpolation, the approximate normalized variance reduction is 0.61. Since two interpolations are performed in succession, the total analysis filtering will be somewhat greater. The combined response is determined from the product of the transfer functions of each step. We expect that the total response for $\lambda \geq 10$ km will remain strong, while heavier damping will occur for shorter wavelengths.

3. CASE STUDIES

3.1 A Comparison of Two and Three Doppler Analyses - 29 April 1977

On the afternoon of 29 April 1977, a cluster of convective cells developed ahead of a squall line advancing from the west and between the Norman, Cimarron, and CHILL Doppler radars. Coordinated data collection scans involving these radars near 1757 CST, provide an excellent opportunity for comparison of two and three Doppler radar analyses. Results of a triple Doppler study of these cells are presented in Ray et al. (1978), who include a brief synoptic weather discussion and a detailed description of the multiple Doppler objective analysis technique utilized. The WSR-57 radar 0° PPI view of the storm is presented in Fig. 9. The dual Doppler analyses utilized data collected by the Norman and Cimarron radars. The analysis grids overlap in the region of most intense convection.

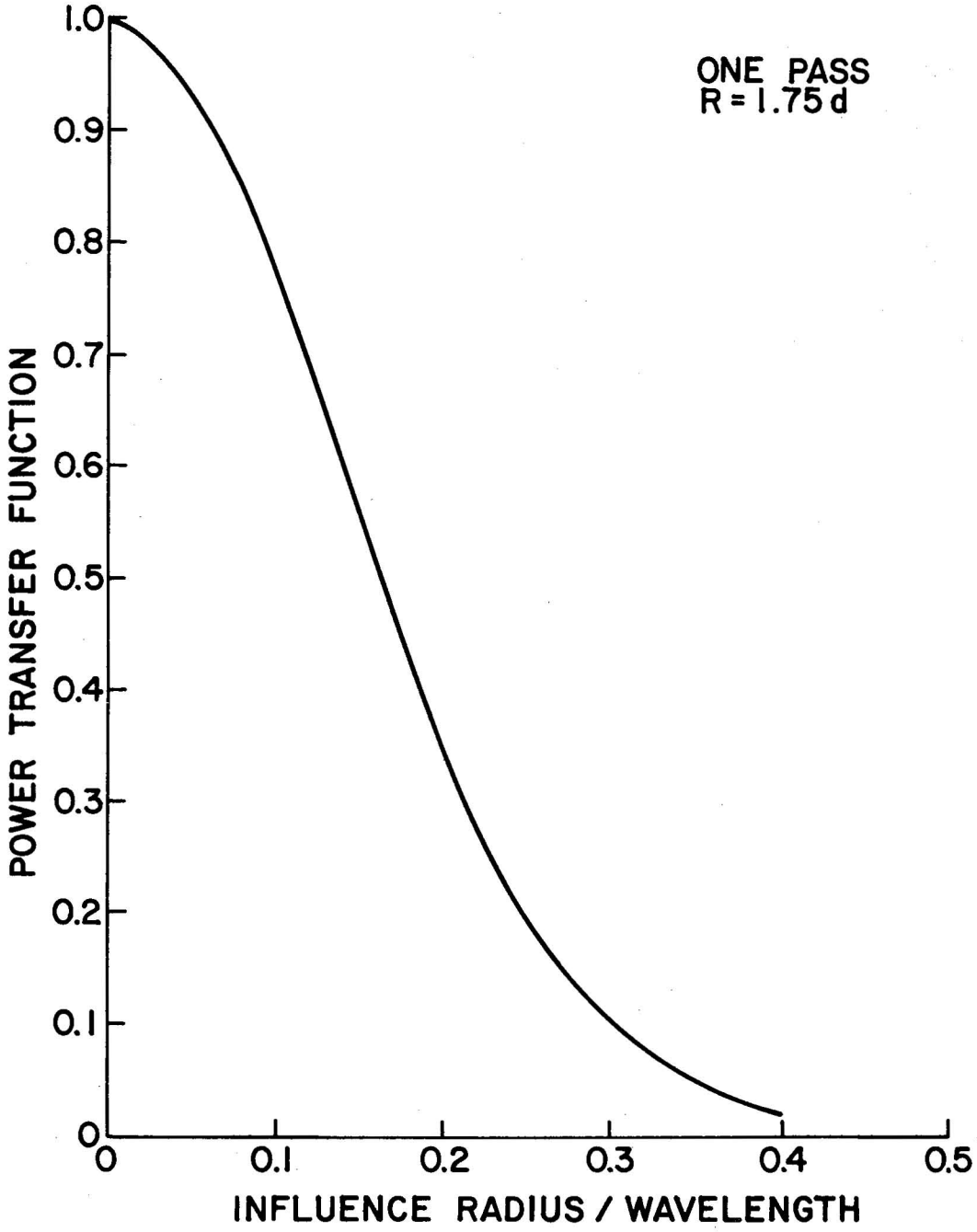

Figure 8. Power transfer function for one-pass application of the method of successive corrections with a zero guess field for (R/d) = 1.75 and d = ΔX (after Stephens and Polan, 1971).

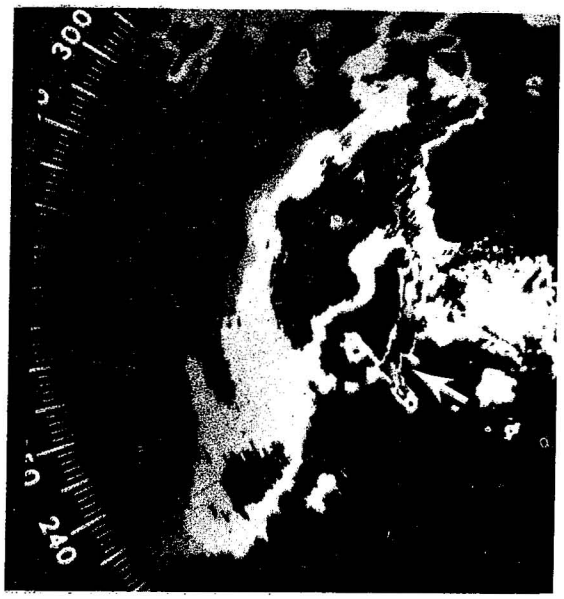

Figure 9. Norman WSR-57 integrated received power at 1757 CST on 29 April 1977. PPI display at 0° elevation. Signal contoured (weakest to strongest) as follows: dim (-103 to -98 dBm); bright (-98 to -88 dBm); black (-88 to -76 dBm); dim (-76 to -65 dBm); bright (-65 to -54 dBm). Arrow indicates cell to be studied.

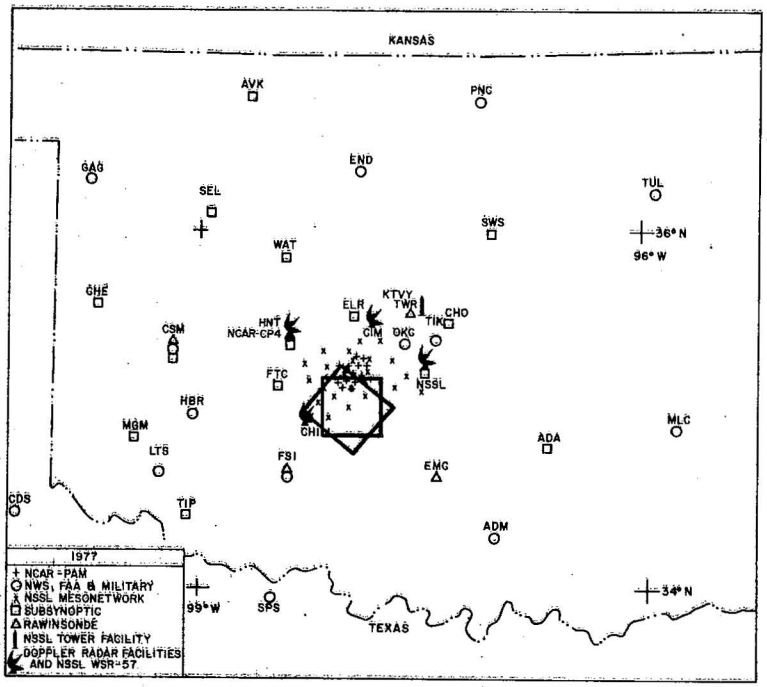

Figure 10. Schematic locating observing sites, dual Doppler domain (northeast-southwest oriented square), and triple Doppler analysis domain (north-south oriented square).

Figure 10 shows the plan view of dual Doppler (Northeast-Southwest grid orientation) and triple Doppler (North-South grid orientation) analysis grid locations with respect to the radars. Horizontal fields of wind and equivalent reflectivity obtained from the two and three radar analyses are presented in Figs. 11a-h. Dual Doppler winds (left side of page) are adjusted within the area enclosed by a heavy dashed line in Fig. 11a, with unadjusted winds outside the dashed boundary. As shown later, variations on the horizontal winds are two orders of magnitude smaller than the mean wind. Consequently, differences are not visually apparent. Storm motion (7.3 m s-1 toward 26° from N) has been removed from all velocities, and is displayed on the compass at the upper left corner of the page. Convergent flow into the region of

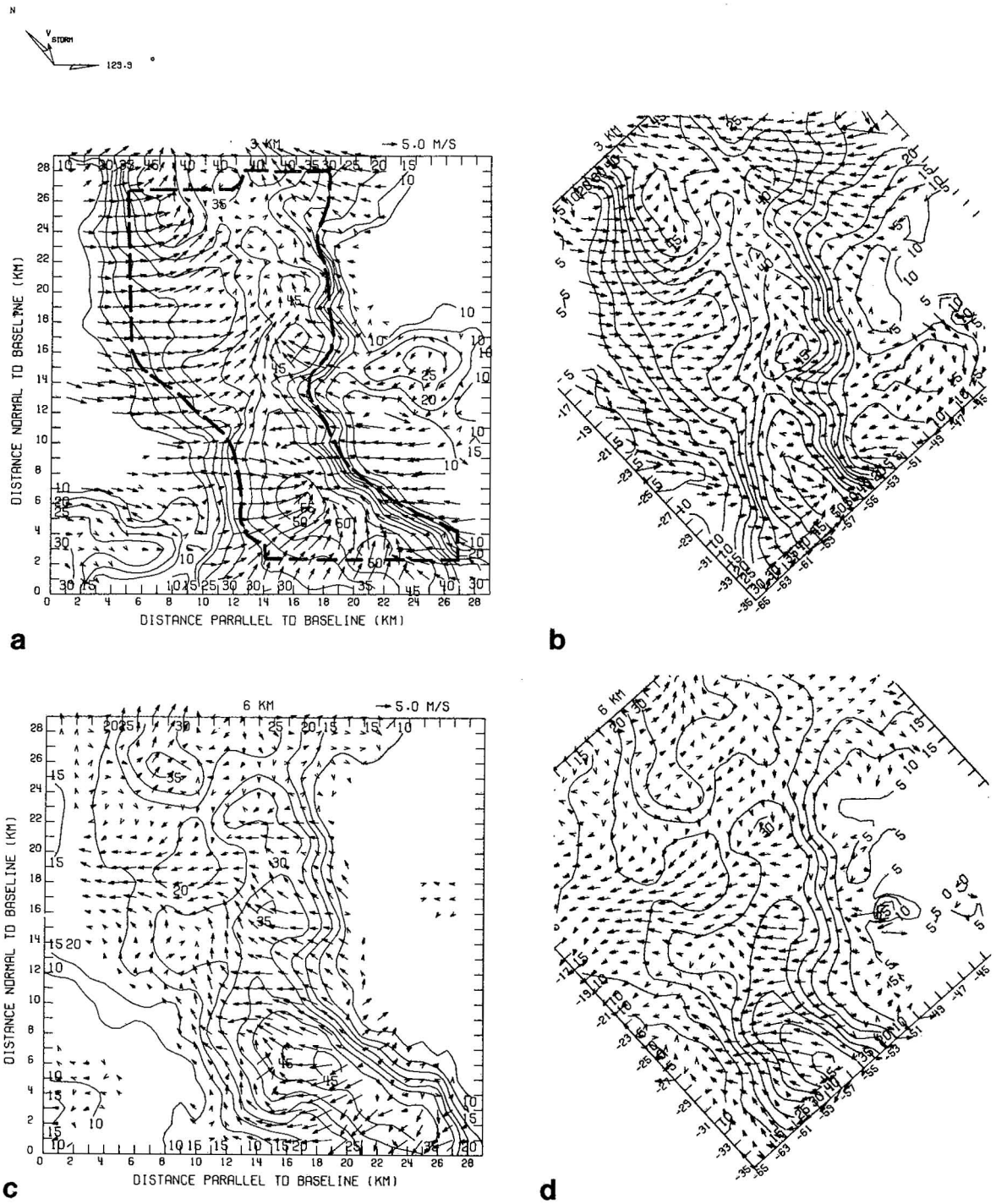

Figure 11a-h. Horizontal winds and reflectivities at 1757 on 29 April 1977. Heights are indicated above each panel. Reflectivity is contoured as 10 log (Z). Dual Doppler fields are on the left and triple Doppler fields are on the right. Mean storm motion (7.35 m s-1 toward 26° from N) component has been removed. Compass (above upper left corner of dual Doppler panels) indicates north toward upper left corner of page. Dual Doppler grid origin is in lower left corner of each panel. Triple Doppler grid origin is Norman radar site. Adjusted dual Doppler winds at 3 km are enclosed by heavy dashed line in Fig. 11a. One grid length = 5 m s-1.

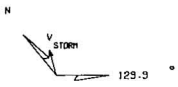
N
V STORM
129.9 °

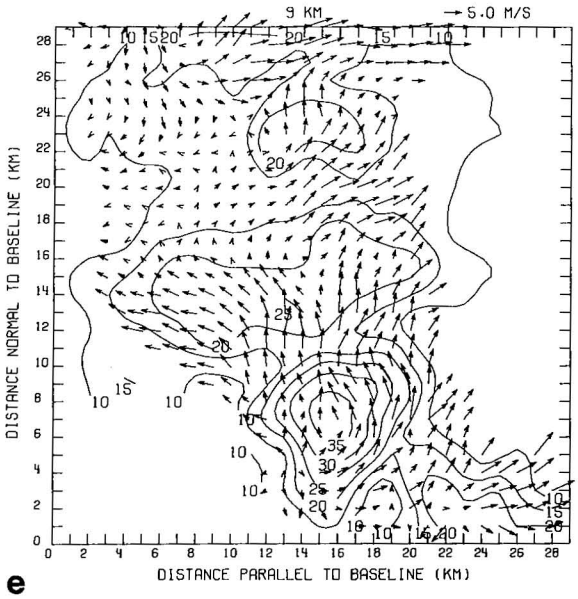
9 KM
→5.0 M/S
DISTANCE NORMAL TO BASELINE (KM)
DISTANCE PARALLEL TO BASELINE (KM)

e

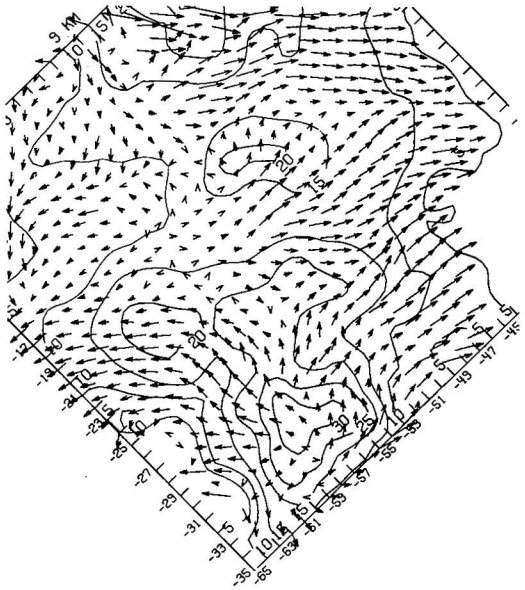
9 KM

f

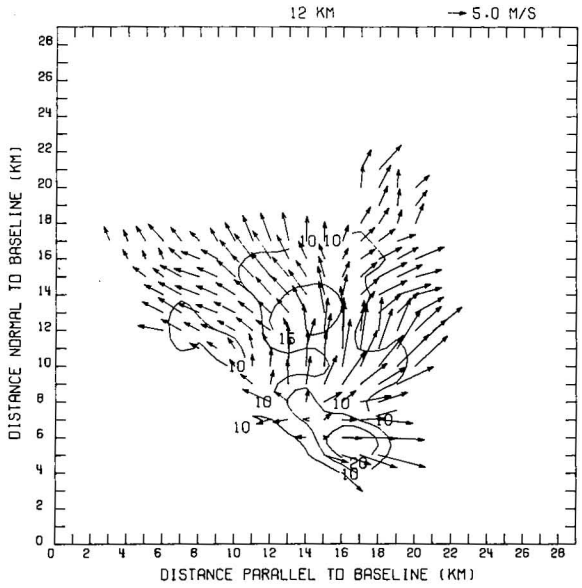
12 KM
→5.0 M/S
DISTANCE NORMAL TO BASELINE (KM)
DISTANCE PARALLEL TO BASELINE (KM)

g

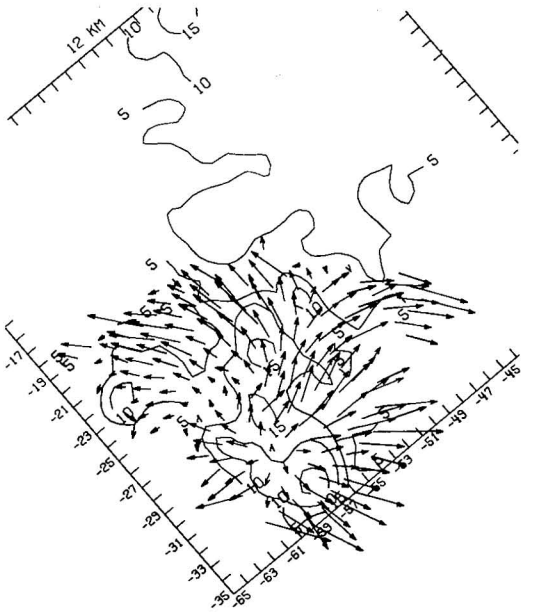
12 KM

h

high reflectivity at 3 km is quite similar for both two and three radar analyses (Figs. 11a and 11b, respectively). Weak circulations at (16, 9) and (16, 6) in Fig. 11a, are also apparent in Fig. 11b. Reflectivities generally agree to within 5 dB. At higher levels (Figs. 11g,h), the flow field as derived from two Dopplers display a relative lack of symmetry compared with the outflow as indicated by three Dopplers. The existence of a symmetric outflow plume is in accord with the presence of weak vertical shear in the environmental winds. It may be concluded that the three Doppler analysis yields quantitatively better horizontal wind fields than may be obtained from the use of two Dopplers. However, the addition of the third radar does not appear to have significantly altered the overall horizontal wind field features.

Figures 12 and 13 depict vertical cross-sections through unadjusted and adjusted dual Doppler analyses and triple Doppler analysis, respectively. Figure 12a shows a plan view of the orientation of dual Doppler cross-sections on the analysis grid while Fig. 13a performs the same function with respect to the triple Doppler analysis. Triple Doppler cross-sections lie parallel to the planes of corresponding dual Doppler cross-sections, but are shifted by small and arbitrary distances in the horizontal coordinate. The A-B cross-sections (Figs. 12b, 13b) are viewed looking to the north into the storm. Tilt and character of updraft, close relation between updraft and radar reflectivity core, the character of horizontal low level inflow and high level outflow, and the existence of horizontal rotors centered near 8 km are features common to each cross-section. Due to the upper boundary condition $w = 2\ m\ s^{-1}$ imposed by the variational analysis (Fig. 12, lower panel), signs of storm top collapse evident in the dual Doppler conventional analysis (Fig. 12, middle panel) and triple Doppler analysis are absent. Note that variationally adjusted winds have been supplemented on the storm flanks by unadjusted winds. Variationally adjusted core updrafts are slightly stronger than unadjusted or triple Doppler updrafts. Adjusted compensating downdrafts on the downshear side of the mid-level rotor are weaker than the corresponding unadjusted downdraft, but comparable to the triple Doppler-derived downdrafts. Comparison of the C-D and G-H cross-sections again indicate that a qualitative similarity exists among the three analyses. The C-D cross-section illustrates how storm top vertical velocities derived by a conventional dual Doppler analysis may be quite "noisy," characterized by large horizontal shears not present in the three Doppler fields. It is important to keep in mind that these triple Doppler vertical motions at storm top are essentially unique, measured quantities that only weakly depend on continuity or other constraints. Large horizontal shears of the vertical motion are absent from the variationally adjusted storm top wind fields. Vertical velocity errors may result from the assumption of storm top stationarity as illustrated by these cross-sections.

Figure 14 illustrates the effects of the variational adjustment procedure on the wind and divergence profile within the updraft core of the 29 April 1977 storm. Plotted results correspond to the interpolated Cartesian fields, but are nevertheless representative of the function of the variational analysis in the cylindrical coordinate system. Unadjusted profiles are dashed while adjusted profiles are solid. Variational adjustment shifts the divergence profile to achieve satisfaction of the integral

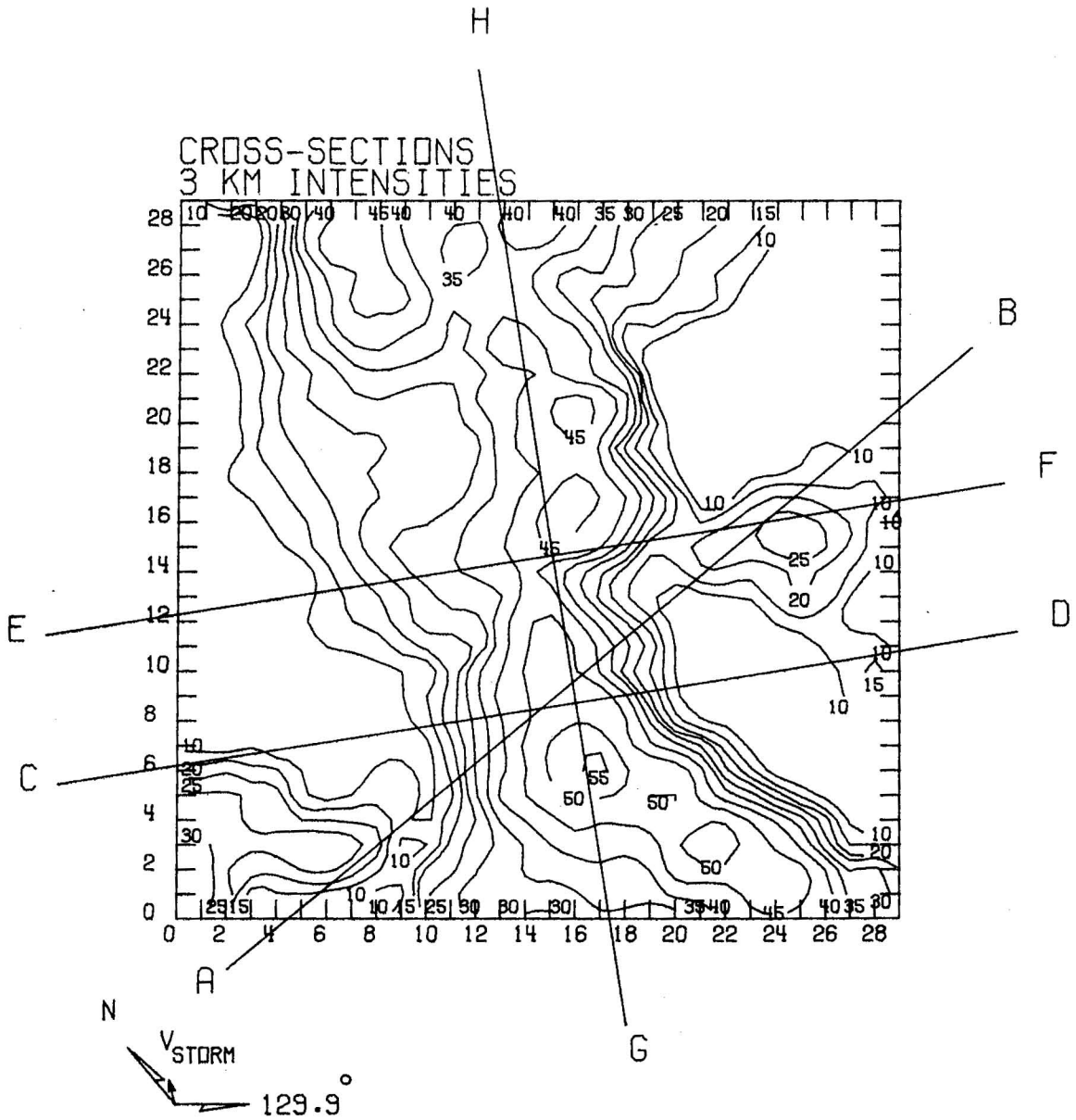

a

Figure 12a-d. Vertical cross-sections through dual Doppler analyses as indicated in Fig. 12a (north toward upper left). Top panel: reflectivity; Middle panel: unadjusted winds; Bottom panel: adjusted winds. Mean storm motion component has been removed. Arrow one grid length long equals 7 m s^{-1}.

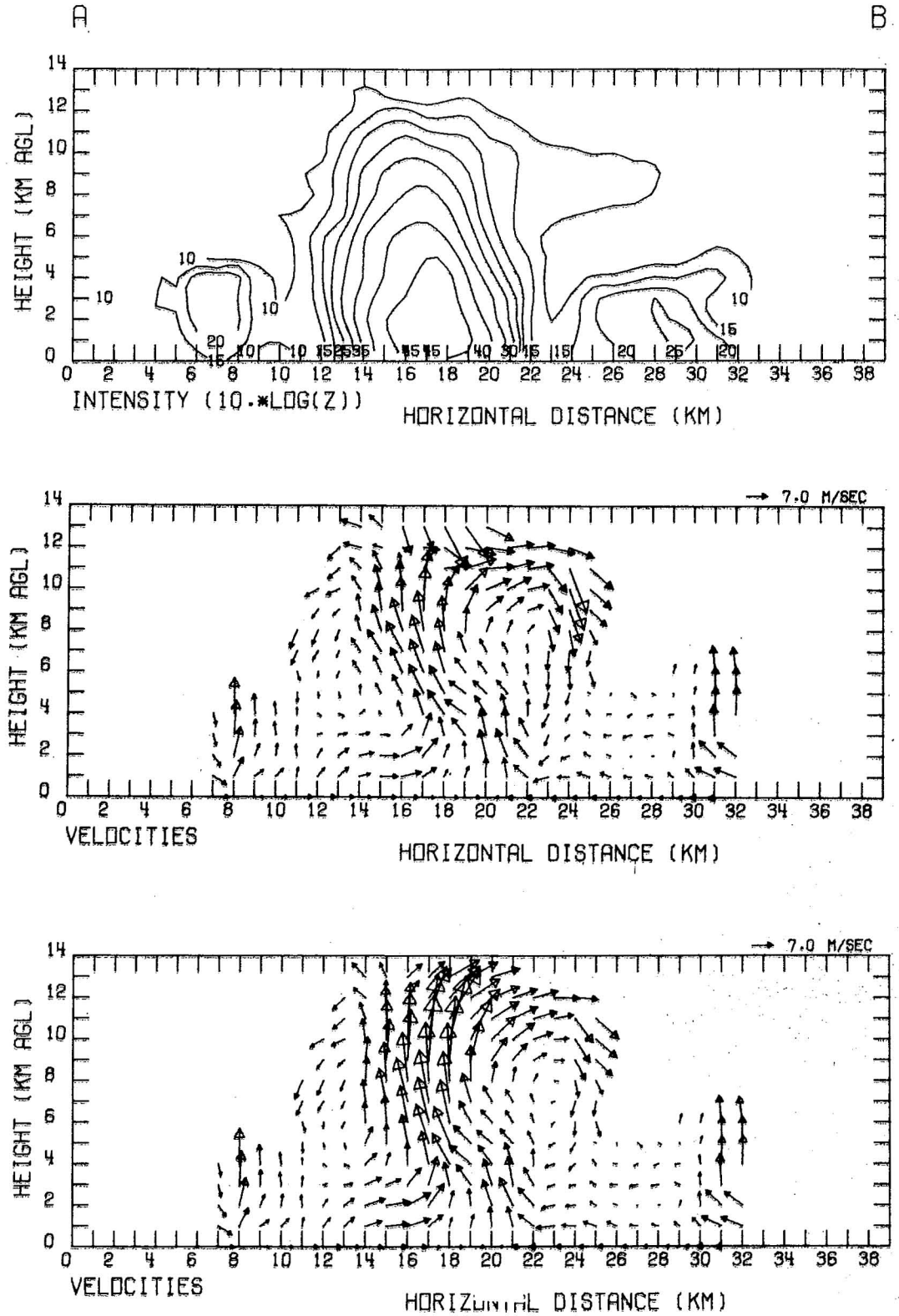
A
B
HEIGHT (KM AGL)
INTENSITY (10.*LOG(Z))
HORIZONTAL DISTANCE (KM)
7.0 M/SEC
VELOCITIES
HORIZONTAL DISTANCE (KM)
7.0 M/SEC
VELOCITIES
HORIZONTAL DISTANCE (KM)

b

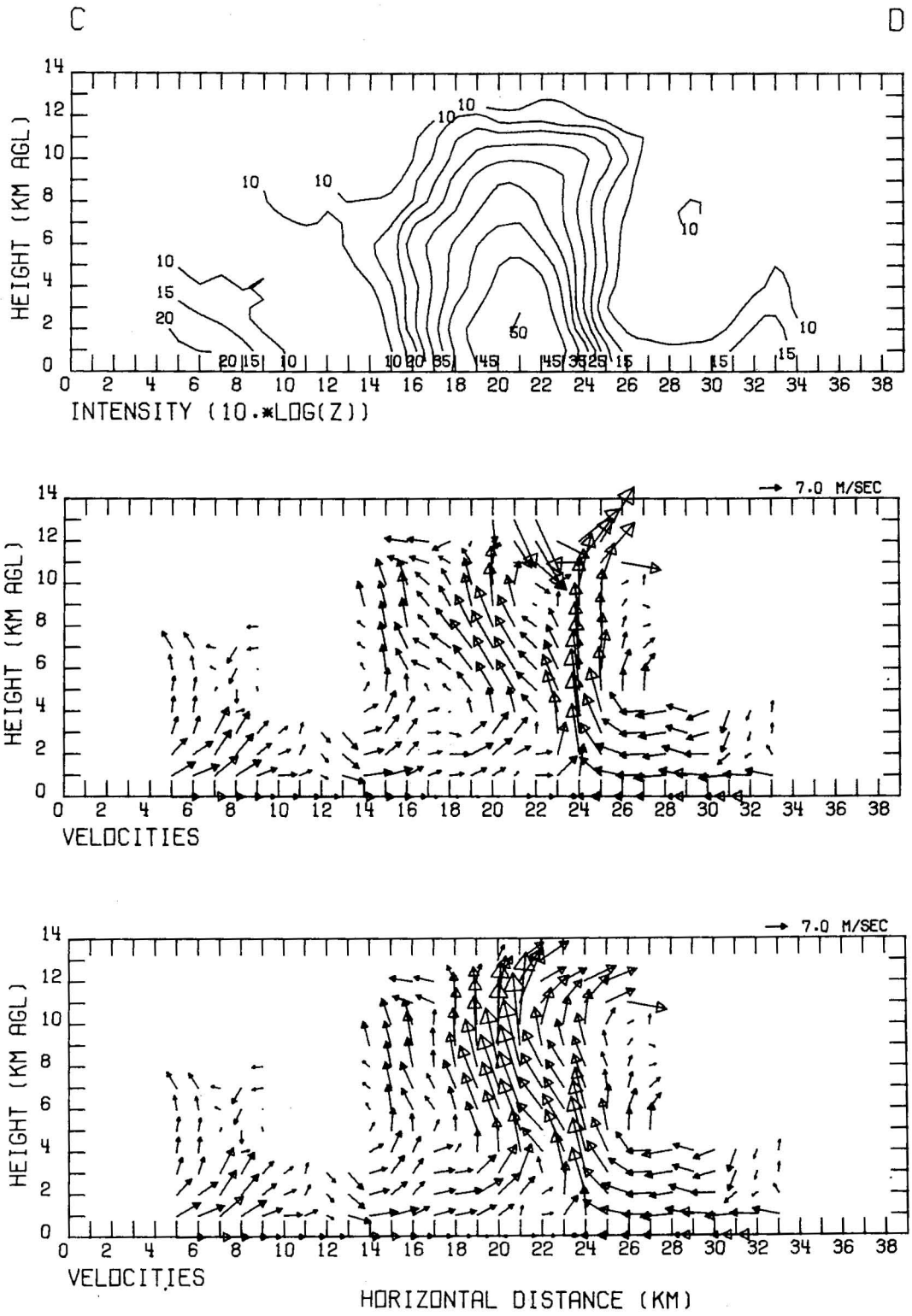
C
D
HEIGHT (KM AGL)
INTENSITY (10.*LOG(Z))
7.0 M/SEC
VELOCITIES
HORIZONTAL DISTANCE (KM)

C

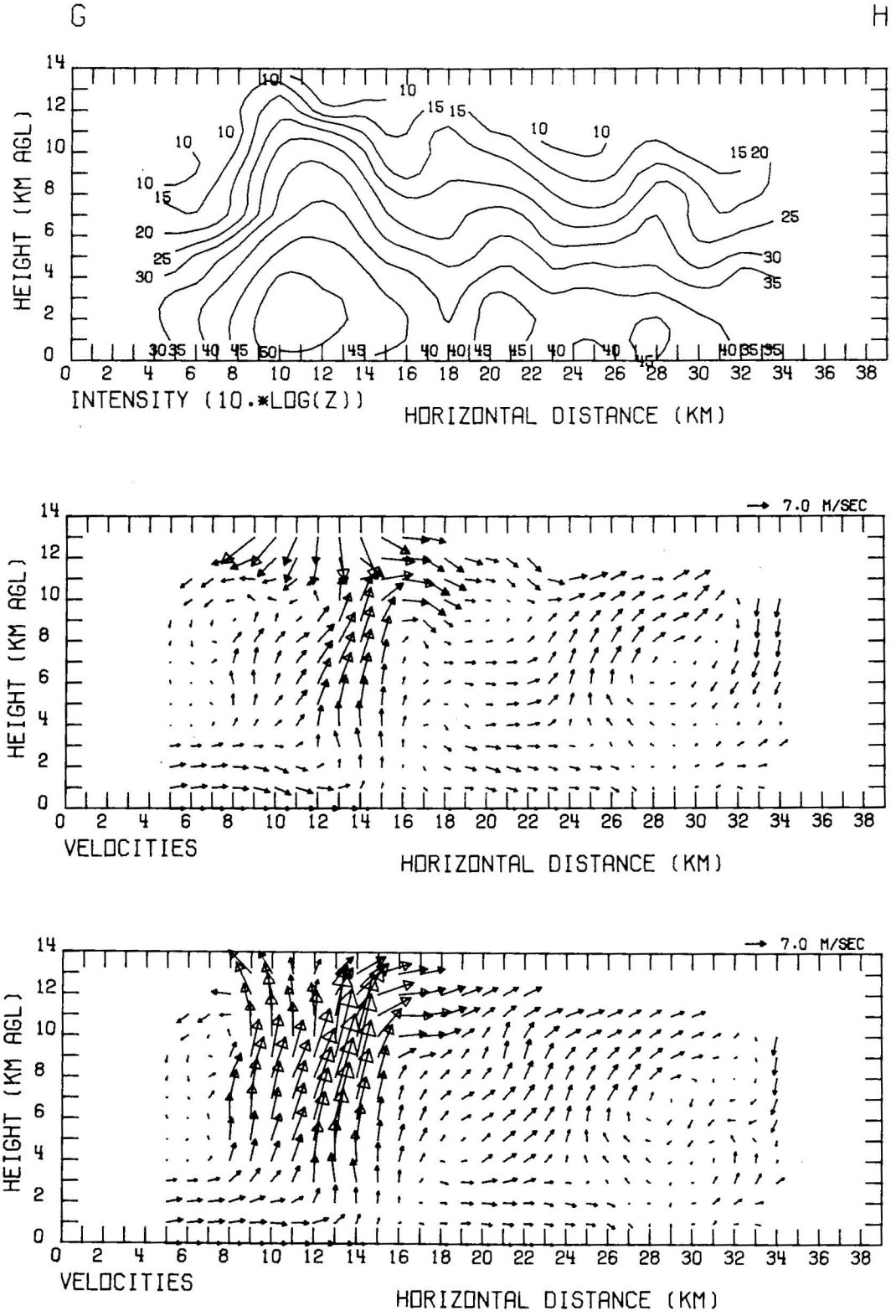
G
H
HEIGHT (KM AGL)
INTENSITY (10.*LOG(Z))
HORIZONTAL DISTANCE (KM)
7.0 M/SEC
VELOCITIES
HORIZONTAL DISTANCE (KM)
7.0 M/SEC
HEIGHT (KM AGL)
VELOCITIES
HORIZONTAL DISTANCE (KM)

d

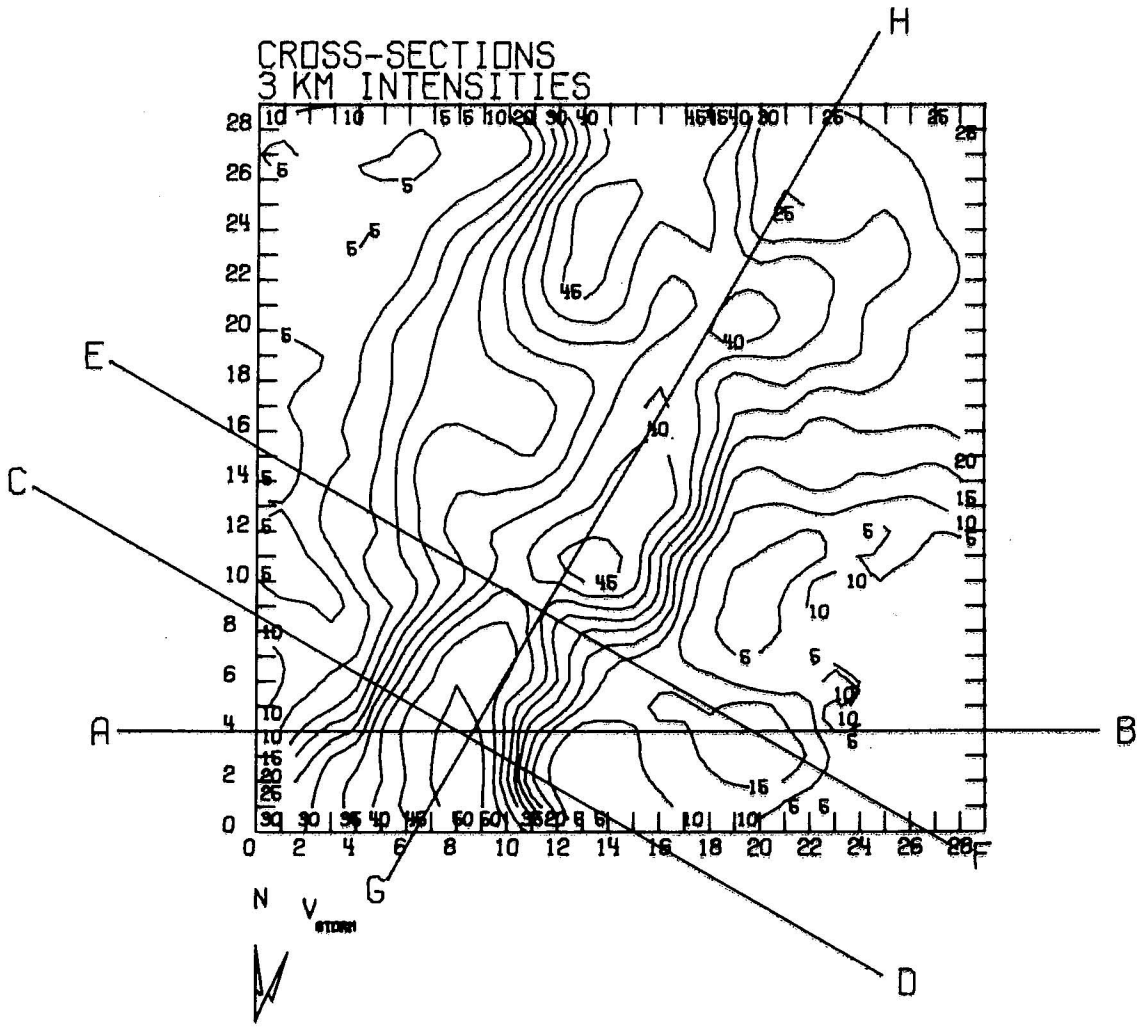

a

Figure 13a-d. Vertical cross-sections through triple Doppler analysis as indicated in Fig. 13a (north toward top of page). Upper panel: reflectivity; Lower panel: winds. Mean storm motion component has been removed. One grid length equals 7 m s^{-1}.

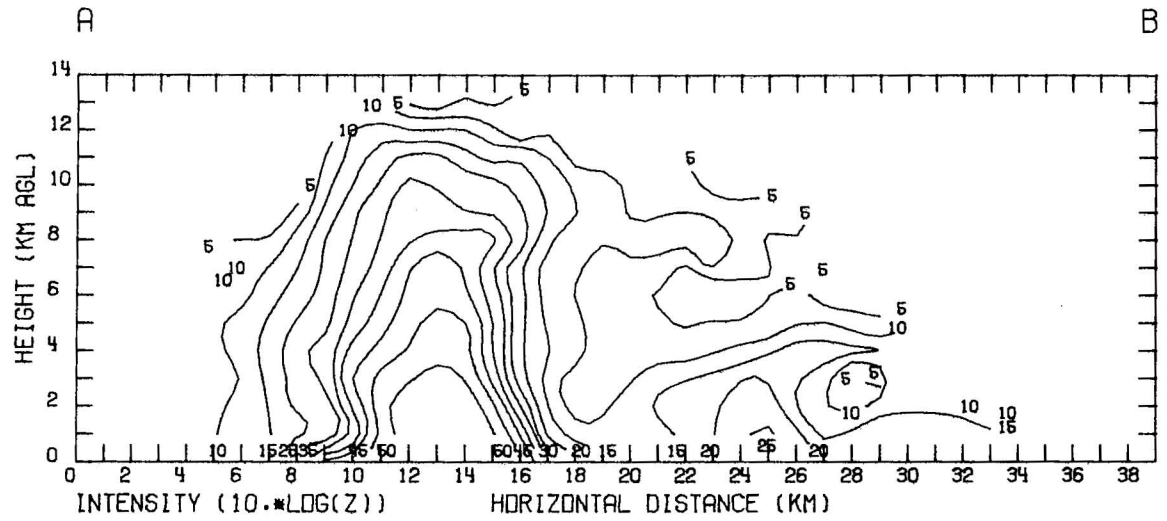
A
B
HEIGHT (KM AGL)
INTENSITY (10.*LOG(Z))
HORIZONTAL DISTANCE (KM)

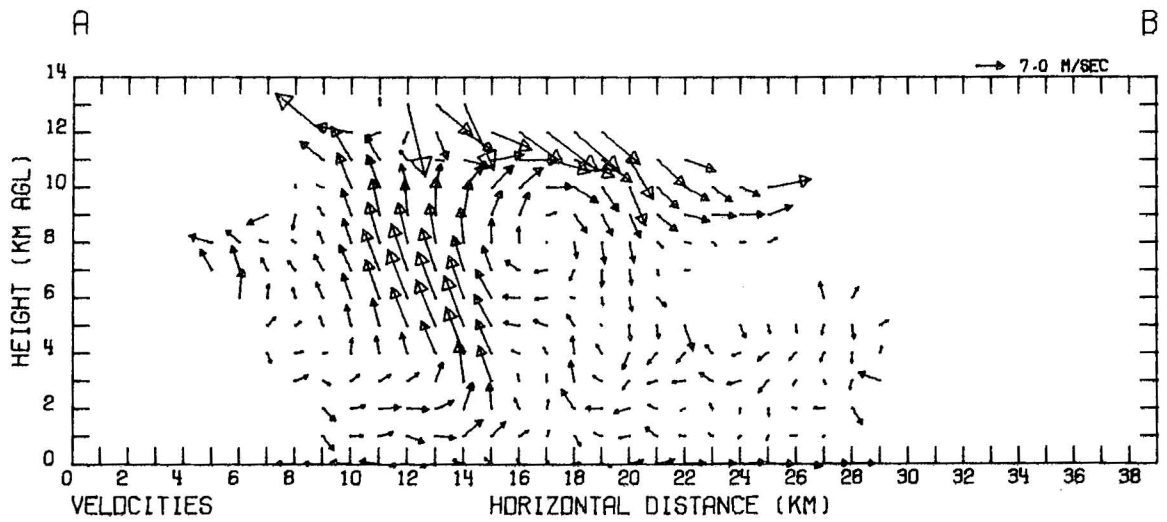
A
B
7.0 M/SEC
HEIGHT (KM AGL)
VELOCITIES
HORIZONTAL DISTANCE (KM)

b

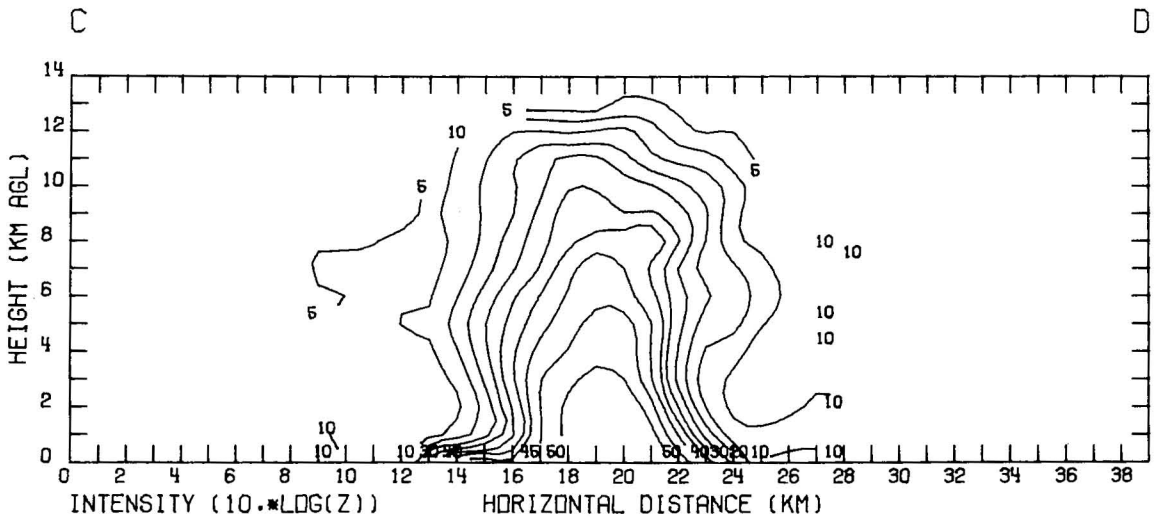
C
D
HEIGHT (KM AGL)
INTENSITY (10.*LOG(Z))
HORIZONTAL DISTANCE (KM)

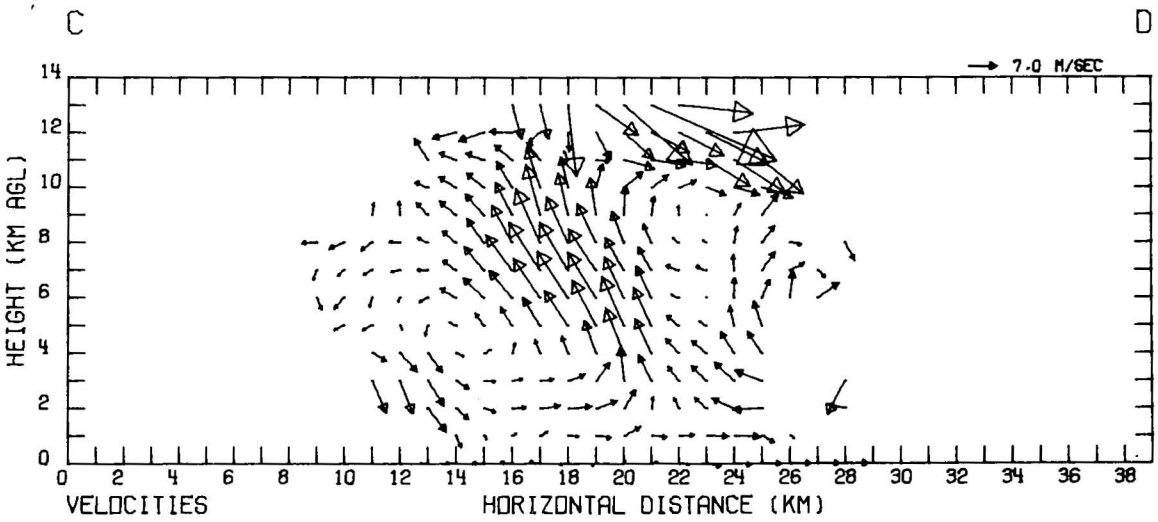
C
D
7.0 M/SEC
HEIGHT (KM AGL)
VELOCITIES
HORIZONTAL DISTANCE (KM)

C

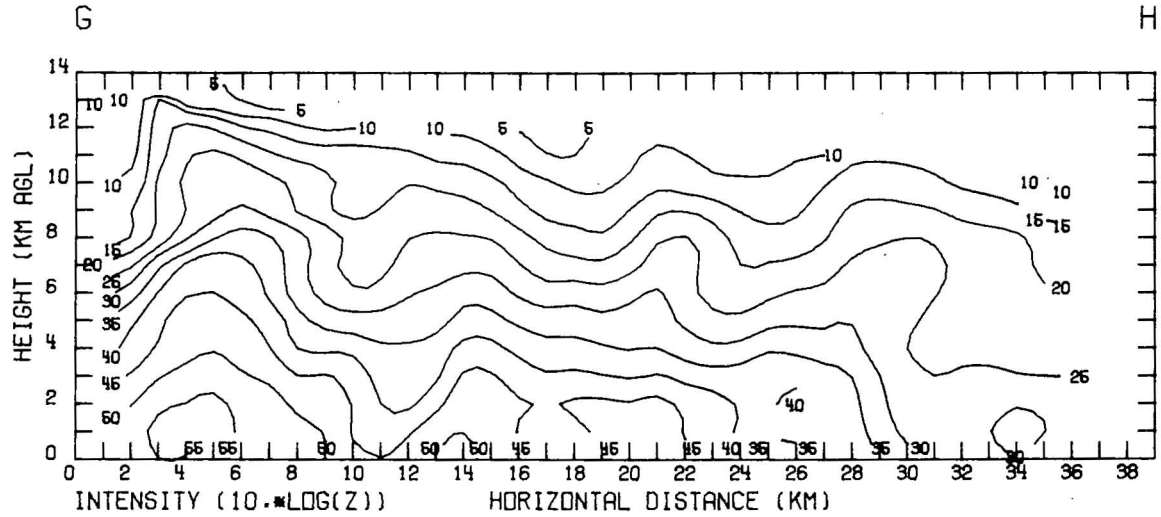
G
H
HEIGHT (KM AGL)
INTENSITY (10.*LOG(Z))
HORIZONTAL DISTANCE (KM)

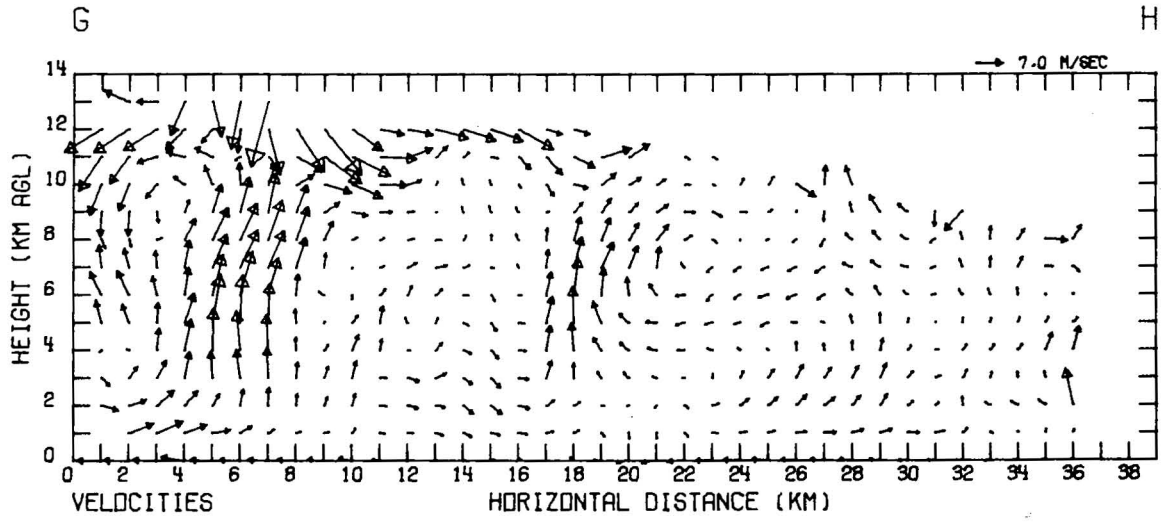
G
H
7.0 M/SEC
HEIGHT (KM AGL)
VELOCITIES
HORIZONTAL DISTANCE (KM)

d

constraint. Observational error which increases with altitude, results in greater horizontal wind and divergence adjustment at higher levels. In the illustration, the maximum updraft has increased in response to the increase in area under the divergence profile below 8 km. Since the shape of the divergence profile is not greatly modified, the shape of the resulting updraft profile is essentially conserved.

The distribution of the means of coplane wind adjustments with elevation for the dual Doppler variational analysis, is shown in Fig. 15. The absolute values of adjustments are used to compute the mean. Since the radar azimuths from Norman and Cimarron (respectively at locations 1 and 2 in Fig. 9) to the storm are nearly at right angles with the radar baseline, the ρ-component is well determined in comparison to the s-component. Consequently, ρ-component wind adjustment is of the order of the assumed Doppler velocity error variance. The ρ-component wind adjustment increases with coplane elevation angle in response to the increasing contribution of the error in terminal velocity estimation. The s-component wind adjustment is constant with elevation because the s-component is completely determined by the radar measurements. Irregularities of coplane mean adjustment at high elevation are due to fluctuations in radial distance as radars tilt out of

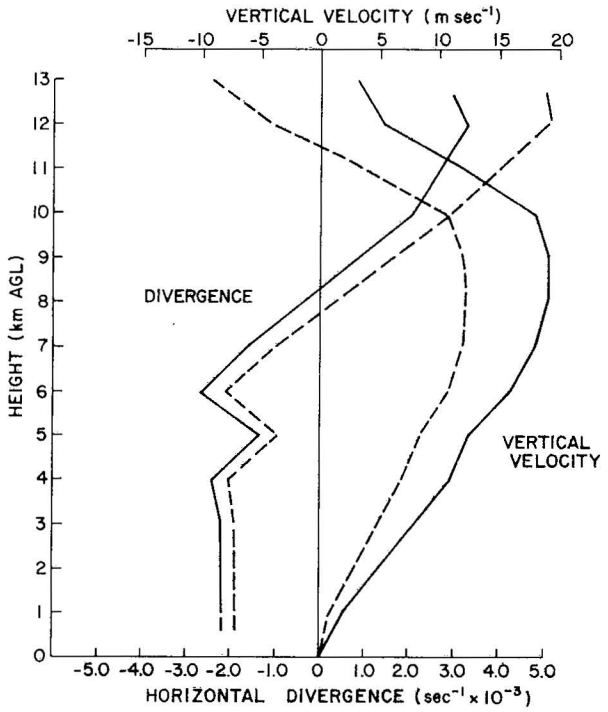

Figure 14. Vertical profiles of vertical velocity and horizontal divergence within core region of 29 April storm. Profiles of unadjusted quantities are dashed curves while corresponding adjusted profiles are solid.

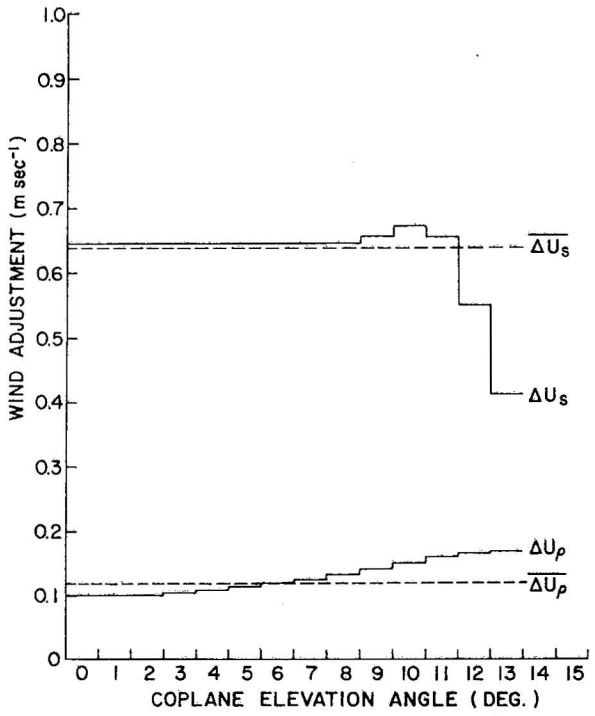

Figure 15. Distribution of means of coplane wind adjustments with elevation angle for dual Doppler variational analysis. Overbar denotes storm volume mean quantity.

the storm. Storm volume mean adjustments, indicated by horizontal dashed lines, are both of the same order as the assumed measurement errors.

Figures 16 and 17 show comparisons of vertical velocity profiles derived by the two and three Doppler analysis techniques, at two select locations within the main storm updraft. Figure 16 indicates a vertical velocity peak on the storm south flank at low levels, while Fig. 17 indicates that the updraft peak has risen to high levels over the storm core. These observations are consistent with the general configuration of the storm flow field, which indicates a main updraft tilted to the north. The "R1" profile was obtained from three Doppler observations by the "Step One" analyses of Ray et al. (1978). In this intermediate analysis step, the three Doppler wind fields weakly satisfy continuity within the influence volume surrounding each gridpoint while strongly depending upon the observations. The "R4" profile results from the application of continuity as a strong constraint through the "Step Four" analysis routine (Ray et al., 1978). The "ZU" and "ZA" profiles

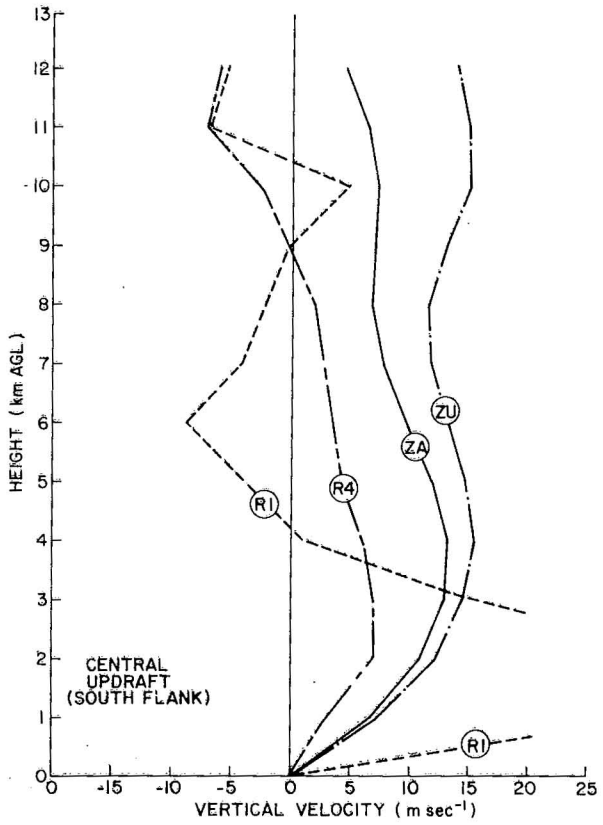

Figure 16. Vertical velocity profiles from two and three Doppler analyses within the central updraft on the 29 April storm's south flank. Labels R1 and R4 correspond to three Doppler steps one and four, respectively. Labels ZU and ZA correspond to two Doppler unadjusted and adjusted analysis, respectively.

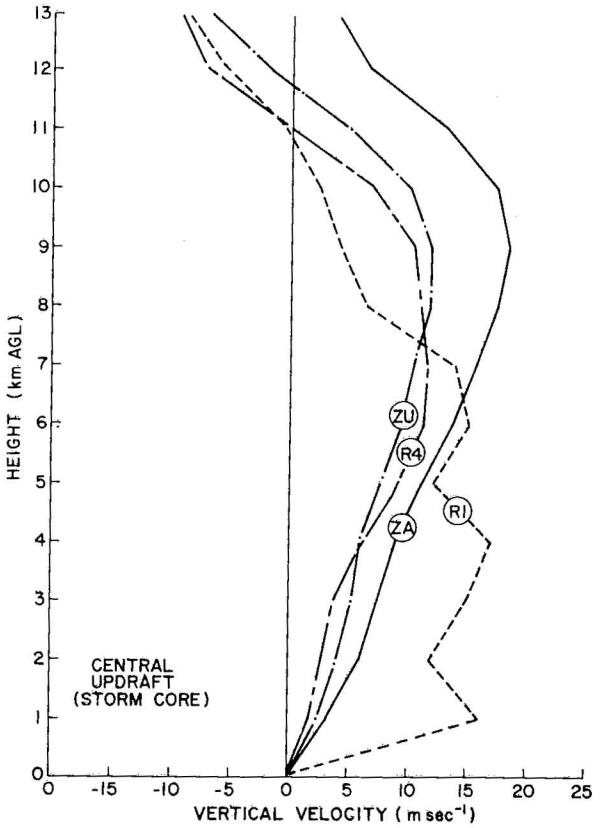

Figure 17. Same as in Fig. 16, but within storm core.

are derived from, respectively, the dual Doppler conventional and variational analyses. The striking similarities between the shapes of two and three Doppler vertical velocity profiles, reflects the qualitative similarities between the horizontal wind (hence divergence) fields as previously discussed. In the storm core central updraft, the two Doppler unadjusted vertical velocity profile agrees very closely with the three Doppler profile. In the south flank of the updraft, the adjusted two Doppler profile is closer to the three Doppler profile than is the unadjusted two Doppler profile. These observations illustrate that the "accuracy" of the dual Doppler variational objective analysis results are dependent upon the accuracy of the assumed kinematic upper boundary condition.

3.2 A Comparison of Two and Four Doppler Analyses - 20 May 1977

An outbreak of convective storms on the afternoon and evening of 20 May and early morning of 21 May 1977 produced a total of 16 tornadoes in Oklahoma. The tornadic Del City storm moved from southwest Oklahoma into the multiple Doppler network near 1700 CST when it developed a single Doppler convergence signature. Data collected from the Del City storm by four Doppler radars between 1736 and 1747 has been used to generate two and four radar analyses for comparison. The four Doppler analysis technique is presented in Ray et al. (1978). The two and four Doppler analyses in this study utilized data collected by the Cimarron and CHILL Radars. Information from the Norman radar and the 5 cm NCAR CP-4 radar (located near Hinton, OK, 88 km at 287° from Norman) completed the data set for the four Doppler analysis. The Norman Doppler 0° PPI view of the Del City storm at 1736 is presented in Fig. 18. The plan view of dual Doppler (northwest-southeast grid orientation) and four Doppler (north-south grid orientation) analysis grid locations with respect to the radars is shown in Fig. 19. The analysis grids have been located to overlap in the region of most intense convection.

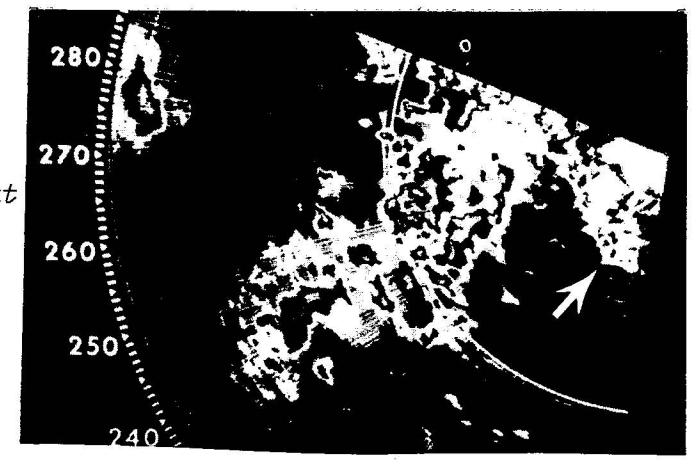

Figure 18. Reflectivity (log Z) at Norman Doppler at 1740 CST on 20 May 1977. Range marks every 20 km. Arrow indicates cell to be studied.

Horizontal fields of wind and equivalent reflectivity obtained from the two and four radar analyses are presented in Figs. 20a-h. Dual Doppler winds (left side of page) are adjusted at all points except on lateral boundaries. Variations on the horizontal winds are at least one order of magnitude smaller than the mean wind so that differences are not visually apparent. Four Doppler fields (right side of page) and dual Doppler fields directly across the page are located at a common altitude. Storm motion (15.1 m s^{-1} toward 35° from N) has been removed from all velocities and is displayed on the compass at the upper left corner of the page. At 4 km (Figs. 20a,b), a north-south oriented confluence band is evident toward the upper right corner while strong cyclonically curving inflow predominates. At 7 km (Figs. 20c,d), axes of anticyclonic and cyclonic curvature appear in the upper right corner and in the reflectivity gradient to the left side, respectively. At 10 km (Figs. 20e,f), strong diverging outflow on the right is flanked by a cyclonic shear zone on the left and flow toward the bottom of the page. The 12 km (Figs. 20g,h) winds are strongly divergent. Twin outflow centers are located in Fig. 20g near the points (17,22) and (19,16) and in Fig. 20h near the points (-25,-20) and (-20,-22). The colocation of these two sets of points highlights the strong similarities between the horizontal wind fields derived from two and four radar observations. Reflectivities generally agree to within 5 dB. We conclude that the use of two additional radars in the wind analysis does not appear to significantly alter the large scale horizontal wind features.

Figures 21 and 22 depict vertical cross-sections through the unadjusted and adjusted dual Doppler analyses and the four Doppler analysis, respectively. Figure 21a shows a plan view of the orientation of dual Doppler cross-sections on the analysis grid while Fig. 22a performs the same function with respect to the four Doppler analysis. Four Doppler cross-sections lie parallel to

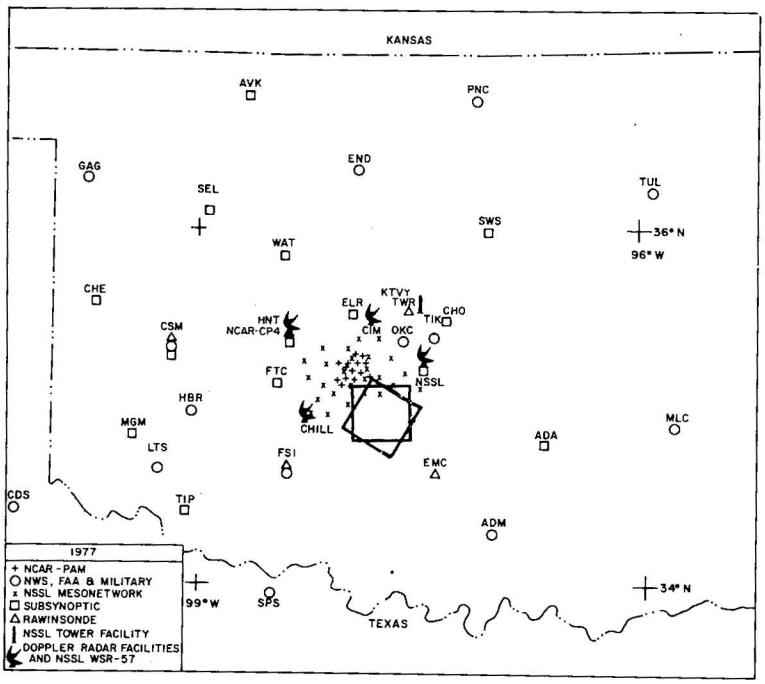

Figure 19. Schematic locating observing sites, dual Doppler analysis domain (northwest-southeast oriented square), and four Doppler analysis domain (north-south oriented square).

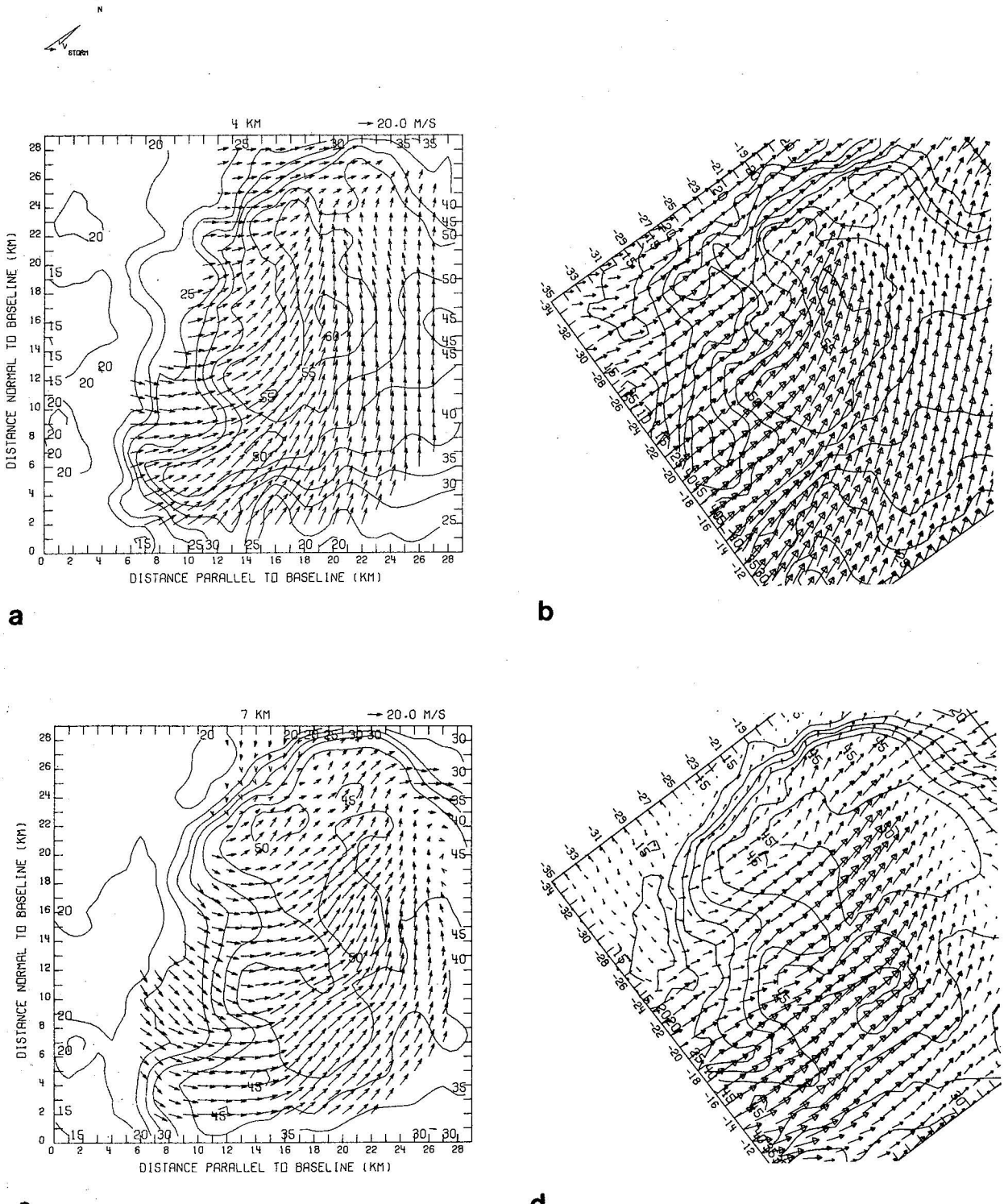

Figure 20a-h. Horizontal winds and reflectivities at 1740 on 20 May 1977. Heights are indicated above each panel. Reflectivity is contoured as 10 log (Z). Dual Doppler fields are on the left and four Doppler fields are on the right. Mean storm motion (15.1 m s^{-1})

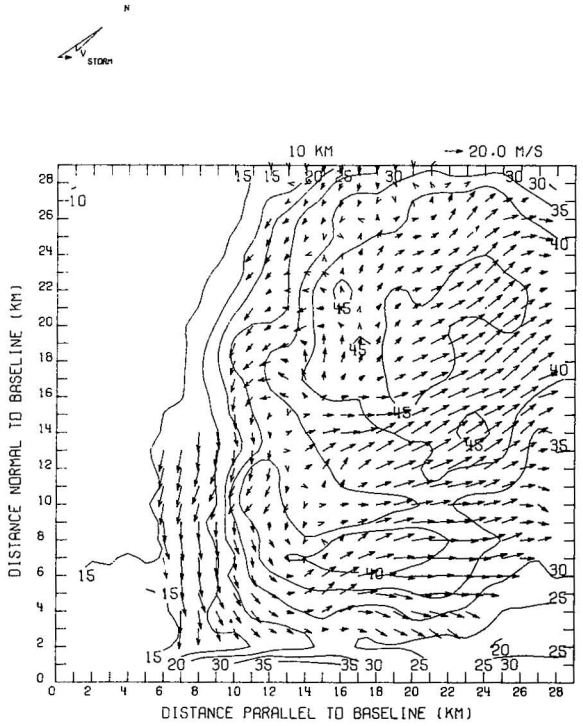

e

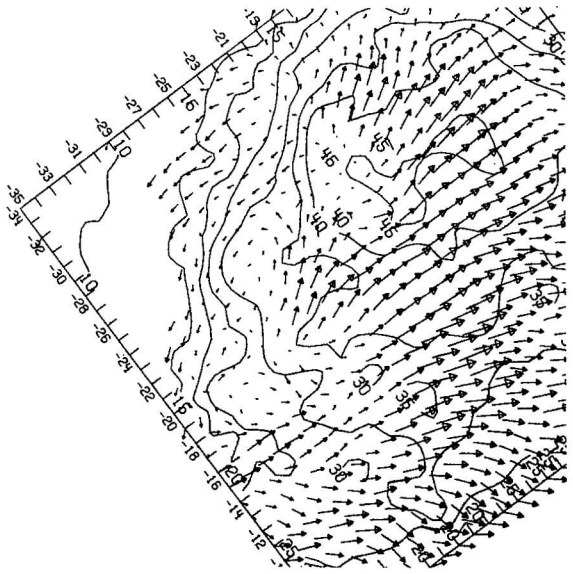

f

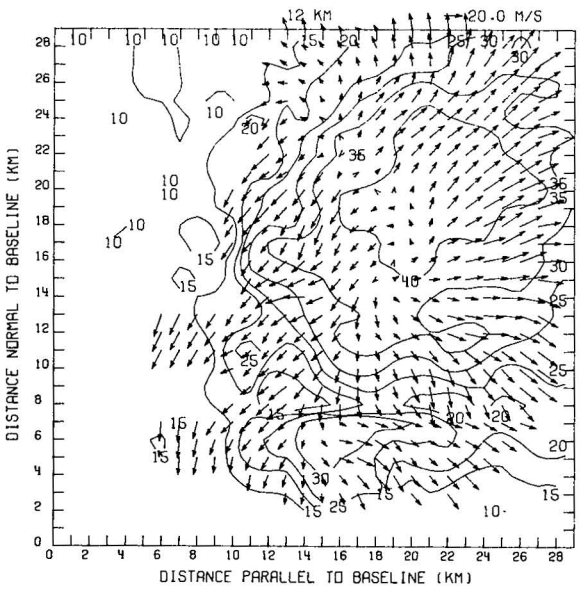

g

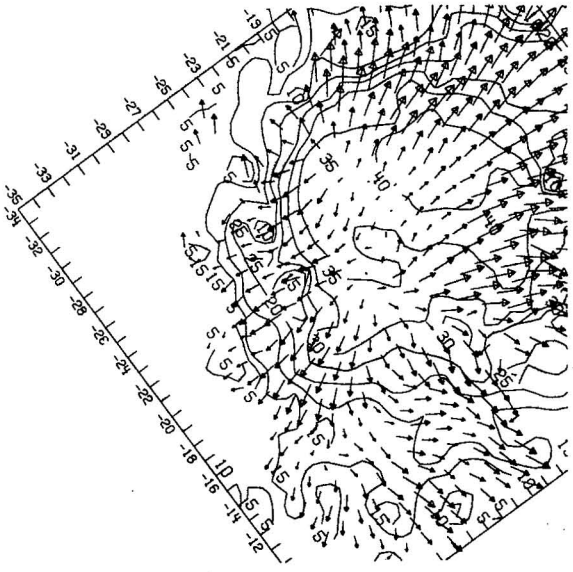

h

toward 35° from N) component has been removed. Compass indicates north toward upper right. Dual Doppler grid origin is in lower left corner of each panel. Four Doppler grid origin is Norman radar site. Arrow one grid length long equals 20 m s^{-1}.

the planes of corresponding dual Doppler cross-sections, but may be shifted by small and arbitrary distances in the horizontal coordinate. The A-B cross-sections (Figs. 21b,22b) are viewed looking to the northwest in the storm. Strong low level convergence associates with a 10 m s^{-1} updraft at (20,1) in Fig. 21b and (12,1) in Fig. 22b. Corresponding reflectivity fields are also quite similar and feature a maximum aloft near 4 km and a core profile canted strongly to the northeast. Indication of storm top collapse from unadjusted dual Doppler winds (Fig. 21b, middle panel) is not evident in the four Doppler wind field (Fig. 22b). As a result of the upper boundary condition ($w = 2$ m s^{-1}) imposed by the variational analysis (Fig. 21b, lower panel), good agreement exists between adjusted two Doppler and four Doppler fields. Neither dual Doppler analysis yields low level downdrafts as strong as those in the four Doppler analysis. The C-D crosssections (Figs. 21c,22c) are viewed looking west. The core of the storm outflow as seen from the four Doppler analysis (gridpoint (24,13) in Fig. 22c) and from the adjusted dual Doppler analysis (gridpoint (28,13) in Fig. 21c, lower panel) contains weak updrafts. The corresponding feature in the unadjusted dual Doppler analysis (Fig. 21c, middle panel) contains strong downdrafts. High level downdrafts in the unadjusted dual Doppler analysis (gridpoint (23,13) in Fig. 21c, middle panel) and four Doppler analysis (gridpoint (18,13) in Fig. 22c) are similar. The constant upper boundary condition used in the variational analysis precludes depiction of this feature. The G-H cross-sections (Figs. 21d,22d) are viewed looking southwest. Strong low level inflow on the left side and pronounced horizontal convergence in the vicinity of gridpoint (20,1) are common features of all three velocity cross-sections. The strong downdraft in the unadjusted dual Doppler analysis around gridpoint (20,13) in Fig. 21d (middle panel) is not present in the adjusted dual Doppler analysis (Fig. 21d, lower panel) or the four Doppler analysis (Fig. 22d). We conclude that the variational adjustment has resulted in improved estimates of vertical velocities, primarily because the conventional analysis often disagreed with the four Doppler analysis as to location and strength of downdrafts near the storm top.

Figure 23 illustrates the effects of the variational adjustment procedure on the wind and divergence profile within the updraft of the Del City storm. Plotted results, which correspond to the interpolated Cartesian fields, adequately represent the wind field in cylindrical coordinates. Unadjusted profiles are dashed while adjusted profiles are solid. The variational adjustment effectively shifts the divergence profile to achieve satisfaction of the integral constraint. The maximum updraft has increased in response to the increase in area under the divergence profile below 10 km.

Figure 24 shows the distribution of the coplane mean wind adjustment with elevation for the dual Doppler variational analysis. Storm volume mean adjustments, indicated by the horizontal dashed line, are nearly one order of magnitude larger than assumed Doppler velocity error variances. Due to the relatively wide radar spacing and the close proximity of the northwest side of the analysis grid to the radar baseline, radials are not perpendicular. Locally, large errors in the derived wind result in the large mean adjustments. The increase of ρ-component wind adjustment with the coplane elevation angle is more pronounced than in the 29 April case because the range of elevation angles is much greater.

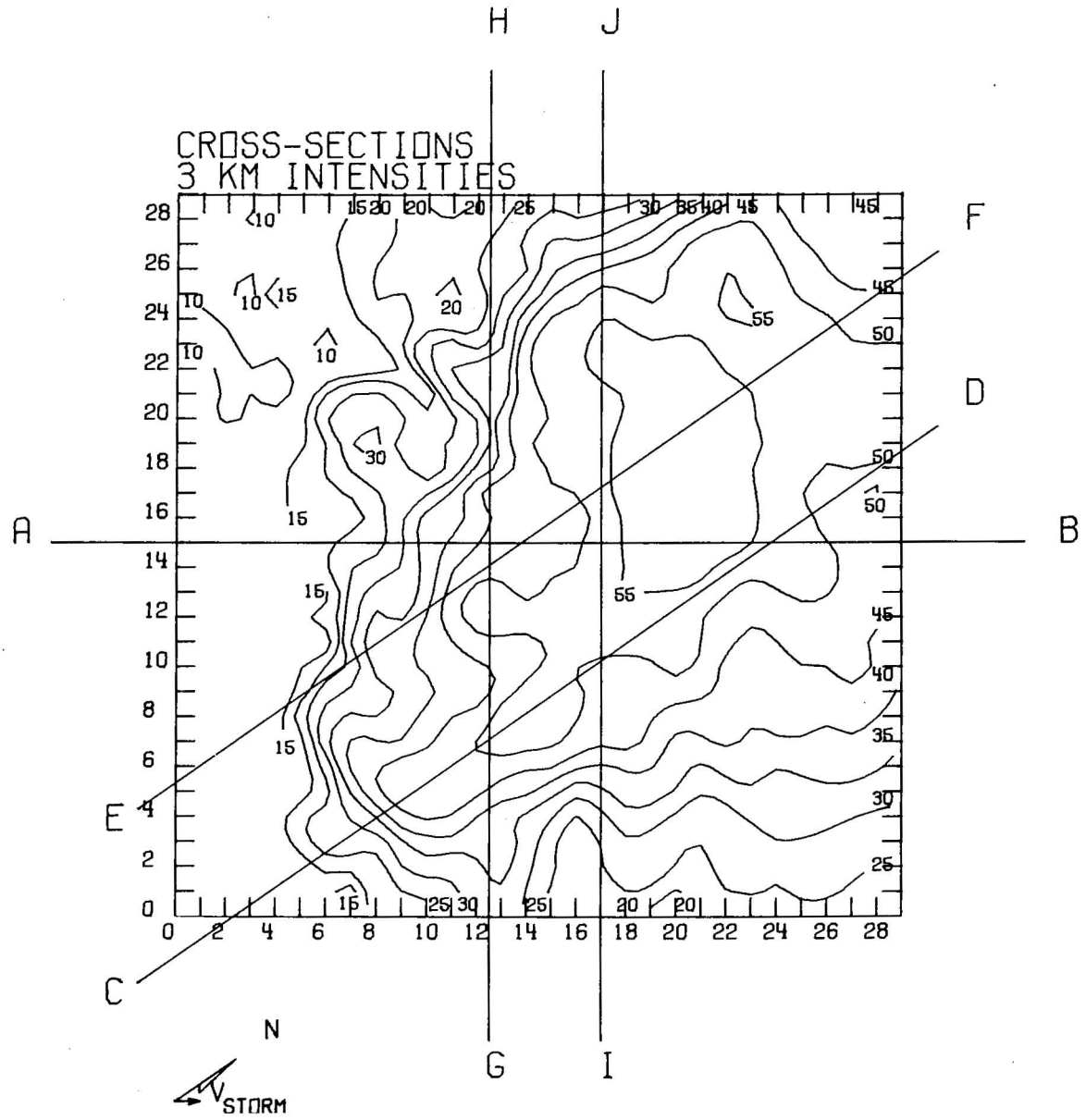

Figure 21a-d. Vertical cross-sections through dual Doppler analyses as indicated in Fig. 21a (north toward upper right). Top panel: reflectivity; Middle panel: unadjusted winds; Bottom panel: adjusted winds. Mean storm motion component has been removed. Arrow one grid length long equals 15 m s^{-1}.

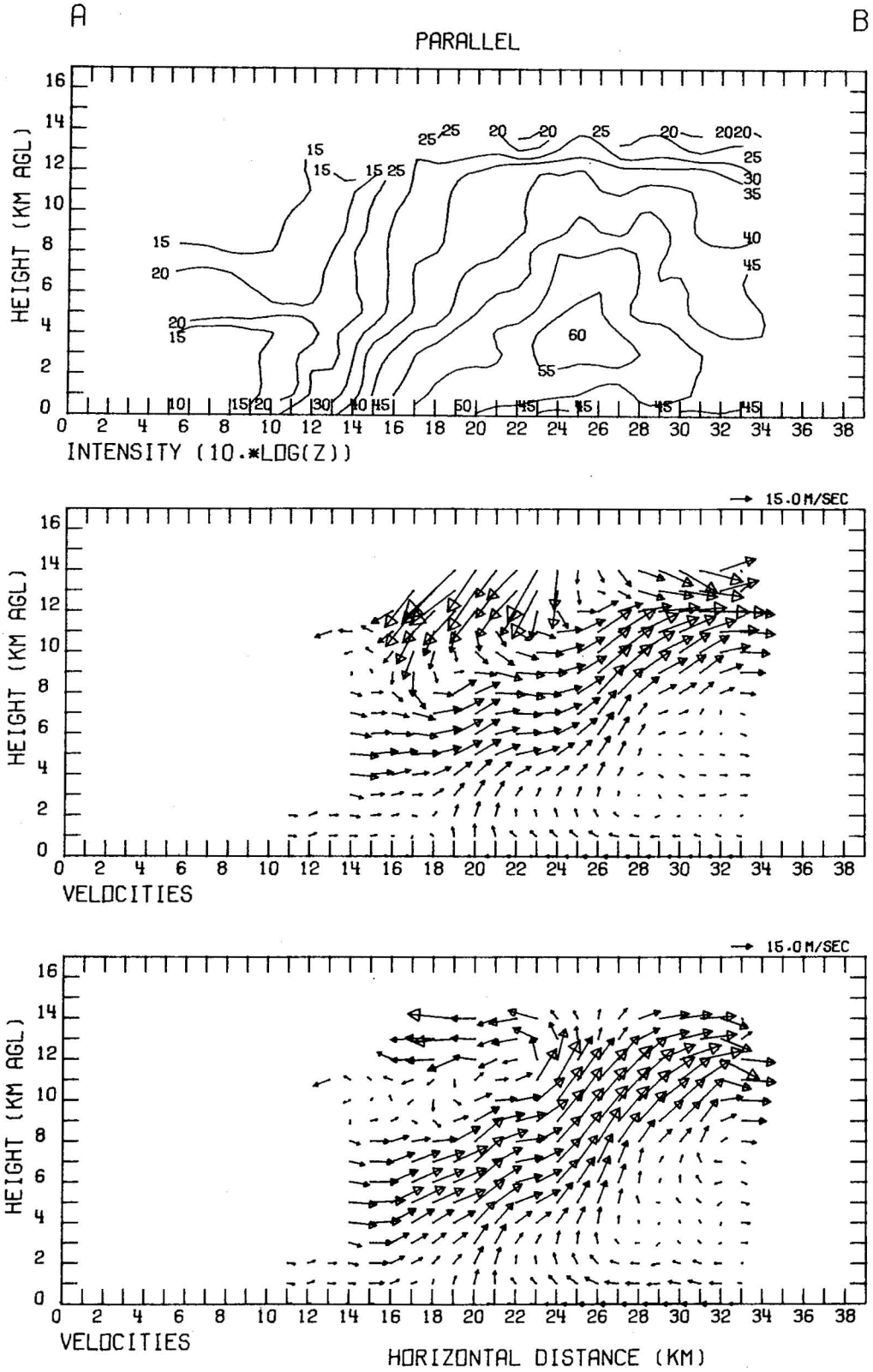
A
B
PARALLEL
HEIGHT (KM AGL)
INTENSITY (10.*LOG(Z))
15.0M/SEC
VELOCITIES
HORIZONTAL DISTANCE (KM)

b

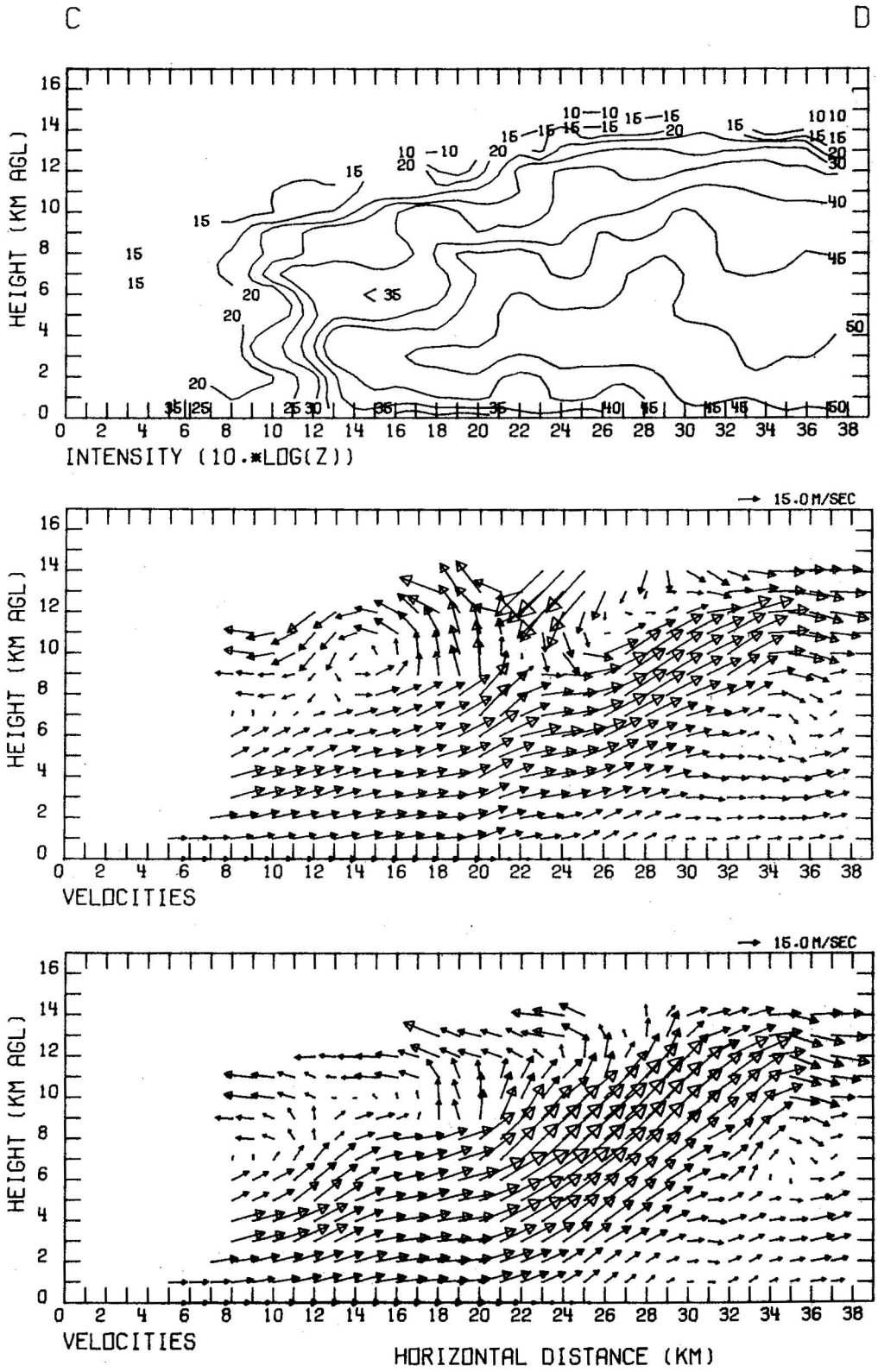
C
D
HEIGHT (KM AGL)
INTENSITY (10.*LOG(Z))
< 35
→ 15.0 M/SEC
VELOCITIES
HORIZONTAL DISTANCE (KM)

C

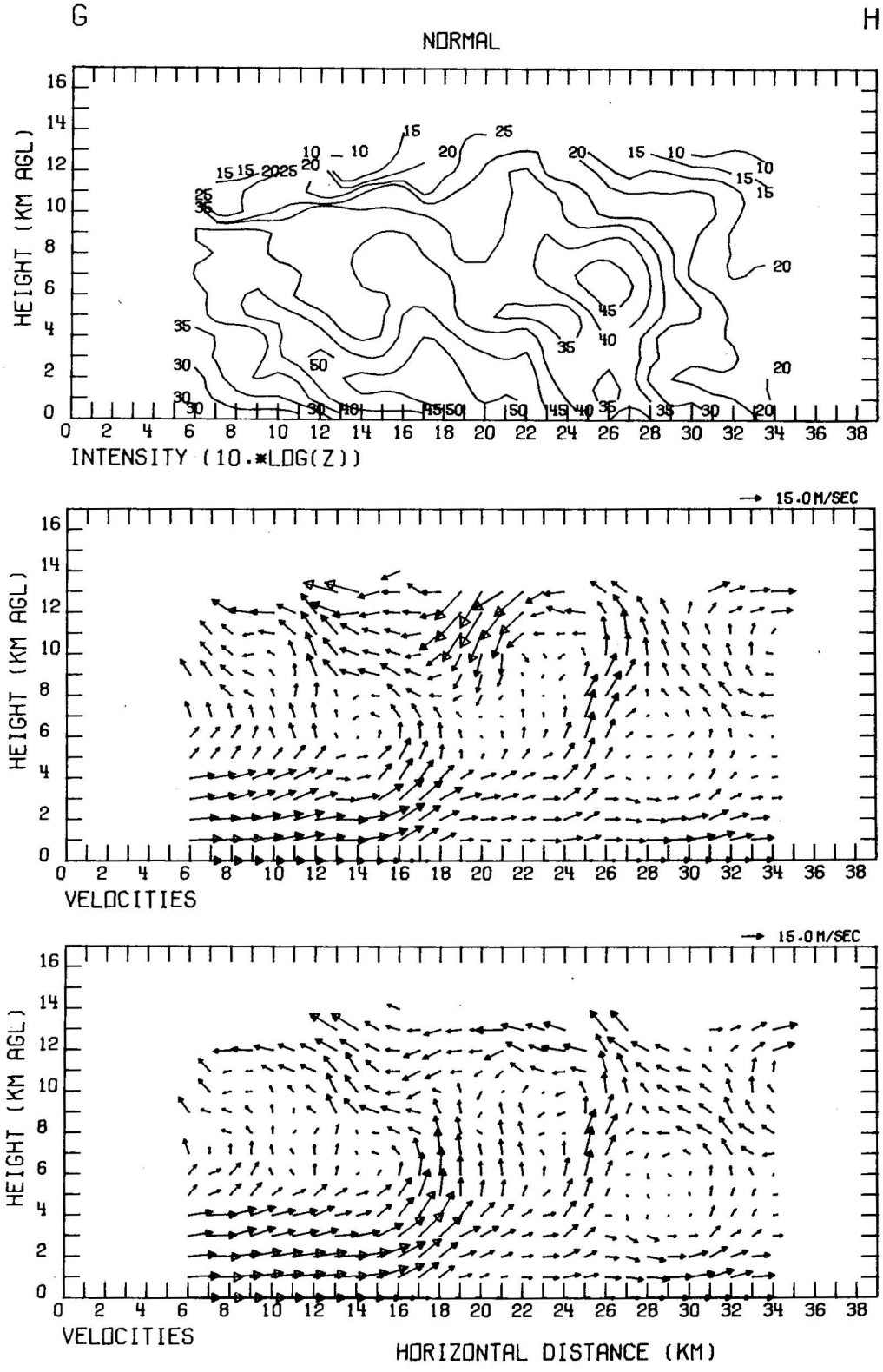
G
H
NORMAL
HEIGHT (KM AGL)
INTENSITY (10.*LOG(Z))
15.0M/SEC
VELOCITIES
HORIZONTAL DISTANCE (KM)

d

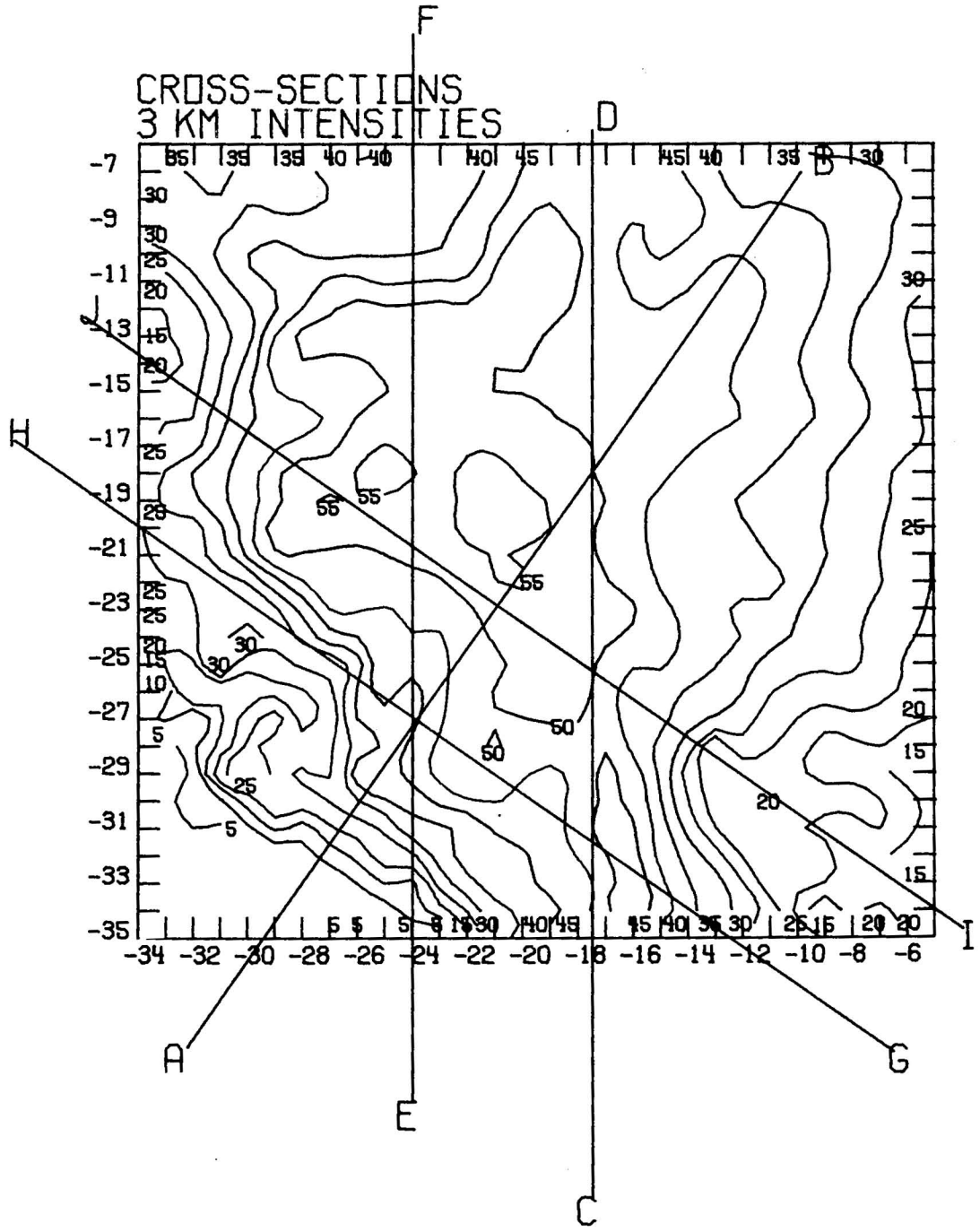

a

Figure 22a-d. Vertical cross-sections through four Doppler analysis as indicated in Fig. 22a (north toward top of page). Upper panel: reflectivity; Lower panel: winds. Mean storm motion component has been removed. Arrow one grid length long equals 15 m s^{-1}.

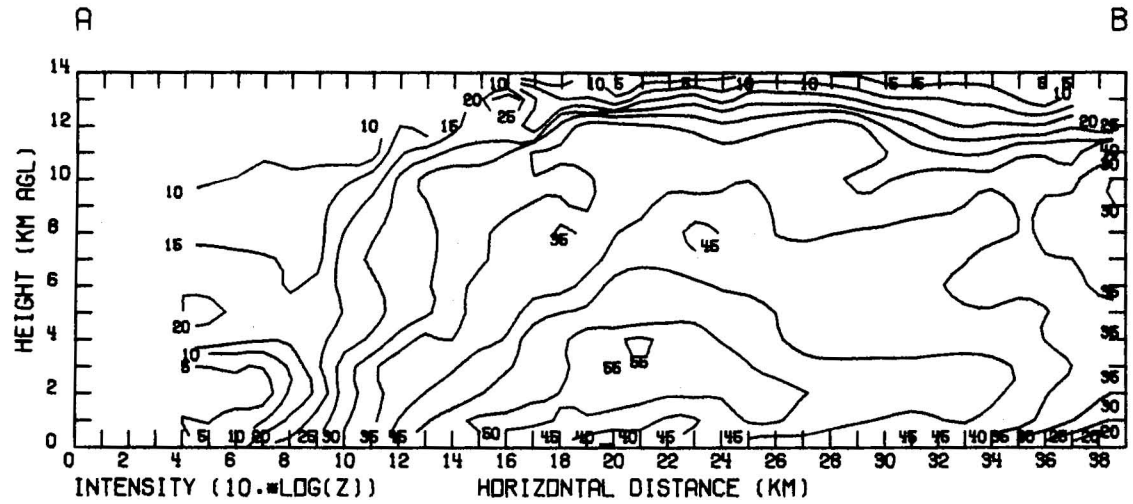
A
B
HEIGHT (KM AGL)
INTENSITY (10.*LOG(Z))
HORIZONTAL DISTANCE (KM)

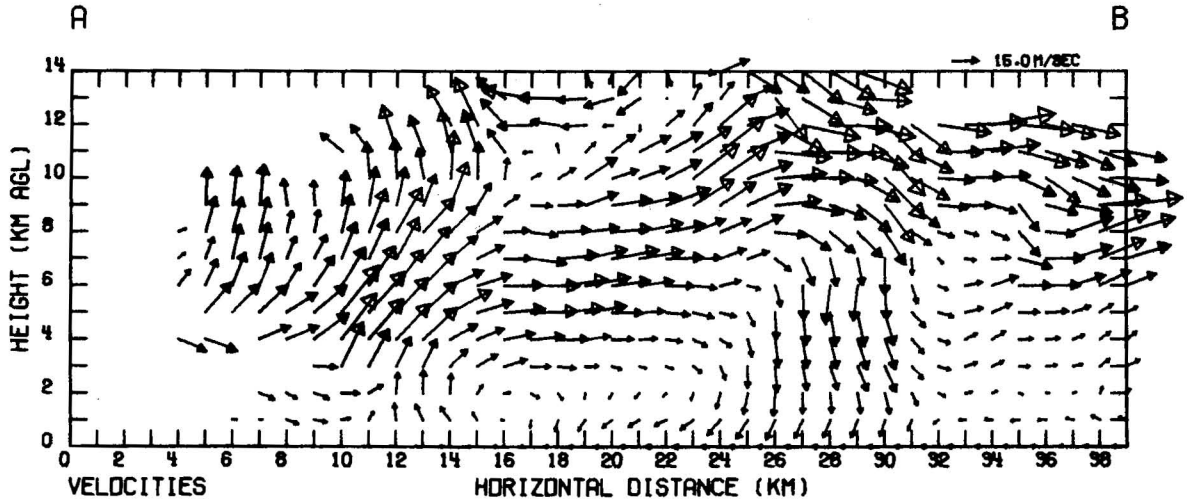
A
B
15.0M/SEC
HEIGHT (KM AGL)
VELOCITIES
HORIZONTAL DISTANCE (KM)

b

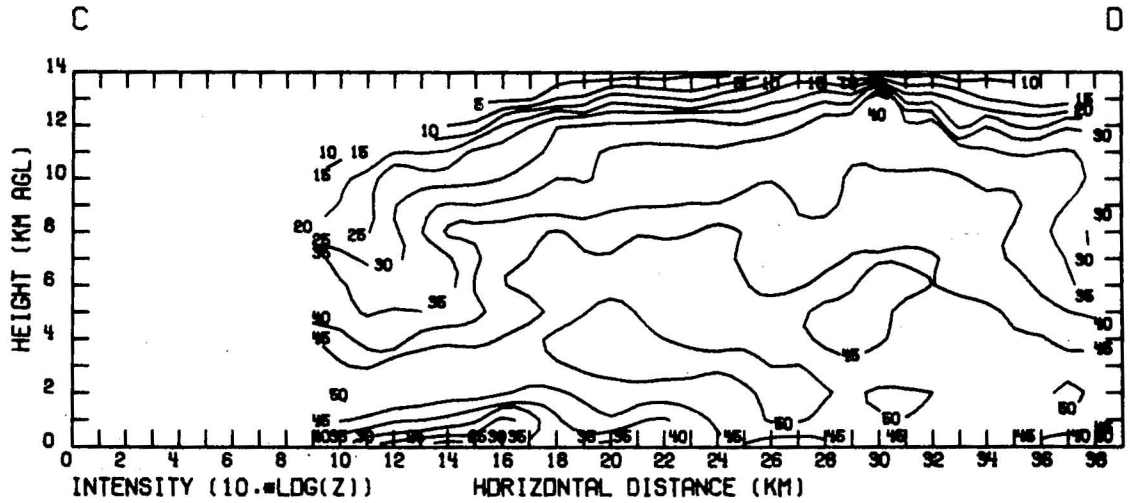
C
D
HEIGHT (KM AGL)
INTENSITY (10.*LOG(Z))
HORIZONTAL DISTANCE (KM)

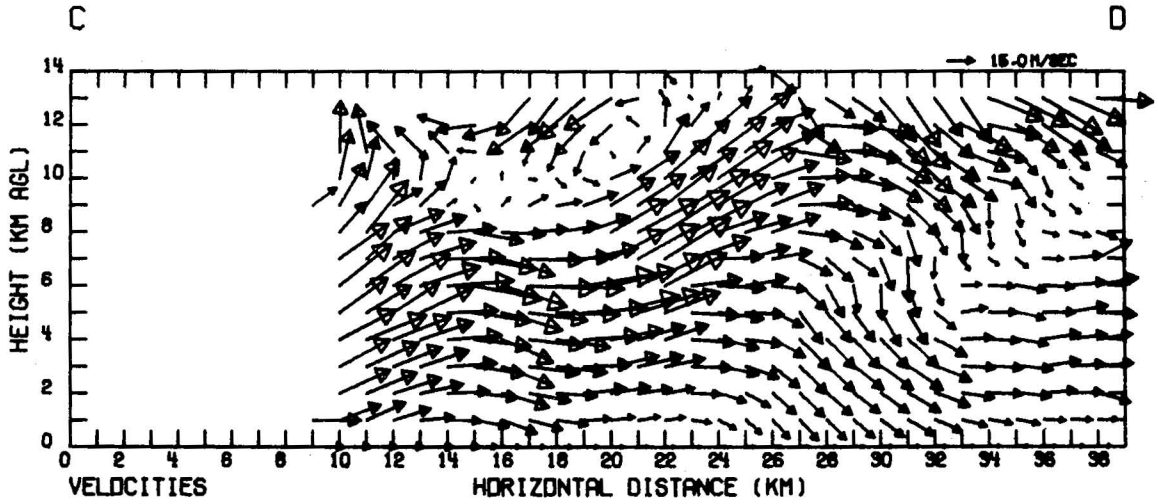
C
D
15.0 M/SEC
HEIGHT (KM AGL)
VELOCITIES
HORIZONTAL DISTANCE (KM)

C

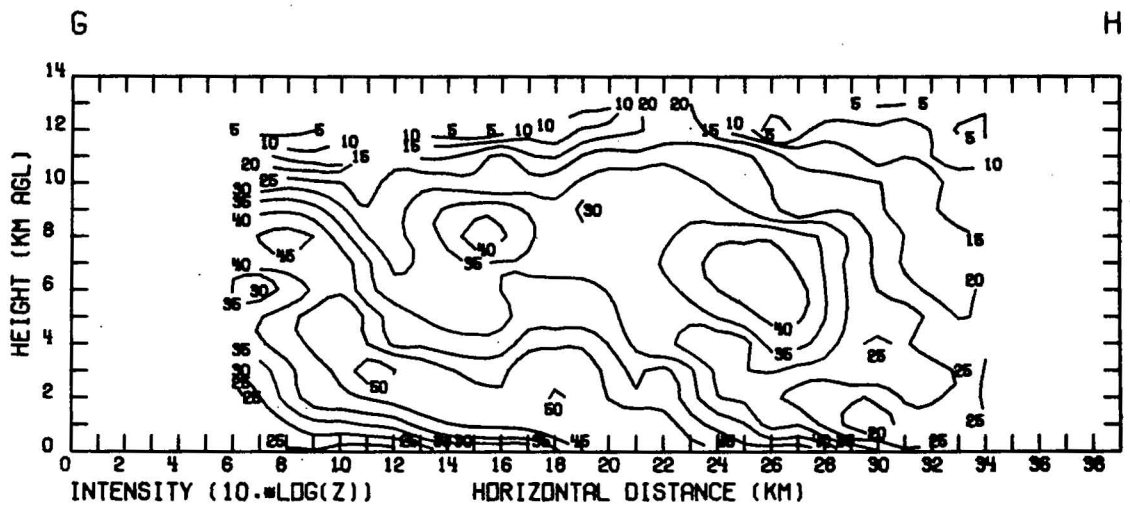
G
H
HEIGHT (KM AGL)
INTENSITY (10.*LOG(Z))
HORIZONTAL DISTANCE (KM)

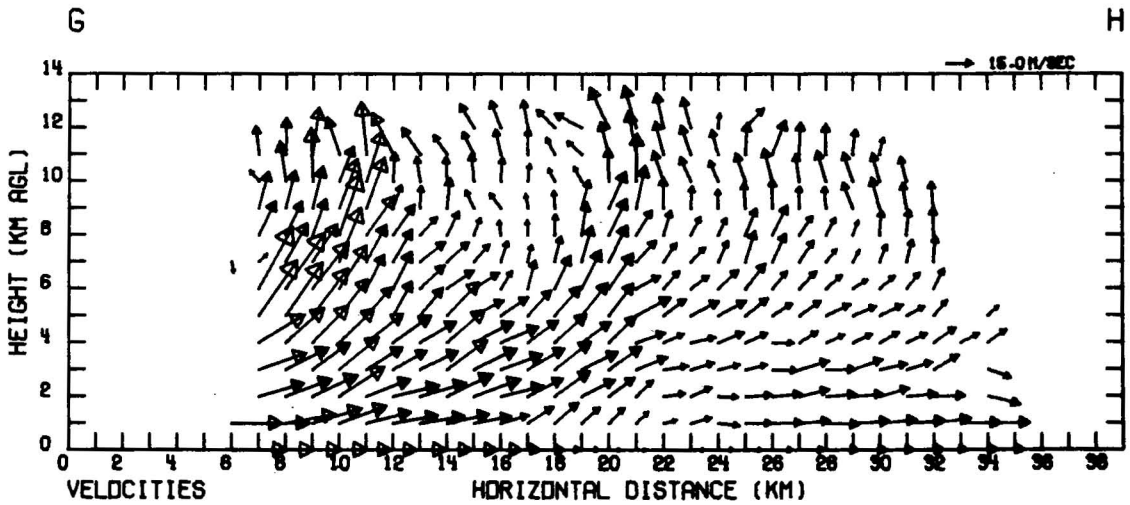
G
H
15.0M/SEC
HEIGHT (KM AGL)
VELOCITIES
HORIZONTAL DISTANCE (KM)

d

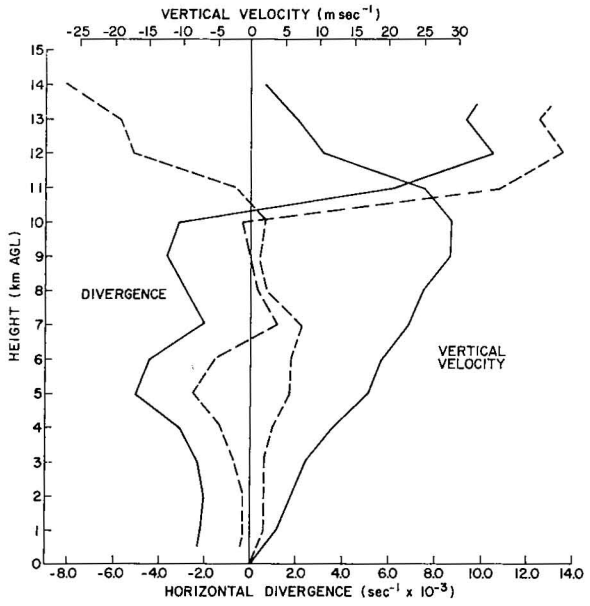

Figure 23. Vertical profiles of vertical velocity and horizontal divergence within core region of 20 May storm. Profiles of unadjusted quantities are dashed while corresponding adjusted profiles are solid.

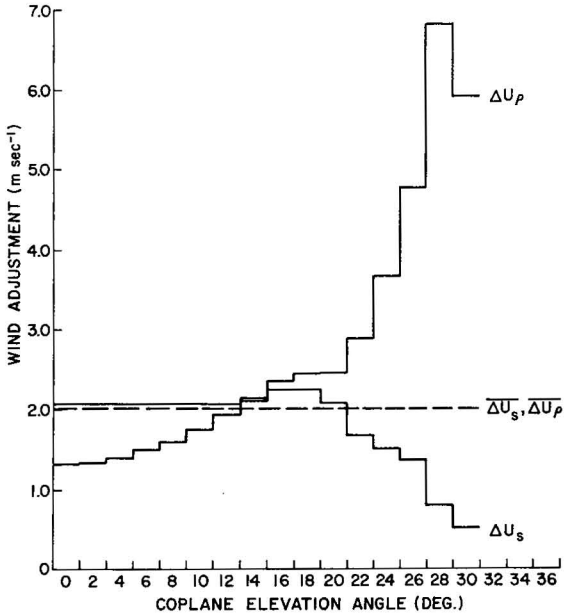

Figure 24. Distribution of means of coplane wind adjustments with elevation angle for dual Doppler variational analysis. Overbar denotes storm volume mean quantity.

Figures 25 and 26 show comparisons of vertical velocity profiles derived by the two and four Doppler analysis techniques at two locations within the storm updraft. Figure 25 shows updrafts in the inflow region of the storm (southeast flank) while Fig. 26 indicates downdrafts beneath updrafts within the storm reflectivity core. The "R4" profile results from objectively analyzed four Doppler observations modified by the application of continuity as a strong constraint. The "ZU" and "ZA" profiles are derived from the dual Doppler conventional and variational analyses, respectively. Figure 25 shows that the variational analysis has eliminated the spurious high level downdraft. Adjusted dual Doppler and four Doppler profiles show good agreement. Results in Fig. 26 illustrate that dual Doppler winds and divergences have been smoothed more than four Doppler winds during interpolation. Despite the small disagreements between adjusted dual Doppler and four Doppler profiles in low levels and at storm top, peak updrafts are in excellent agreement. These illustrate that the variational analysis yields the greatest improvement in estimated vertical velocities in the case where conventional dual Doppler derived vertical velocities are excessively large in the vicinity of the storm top.

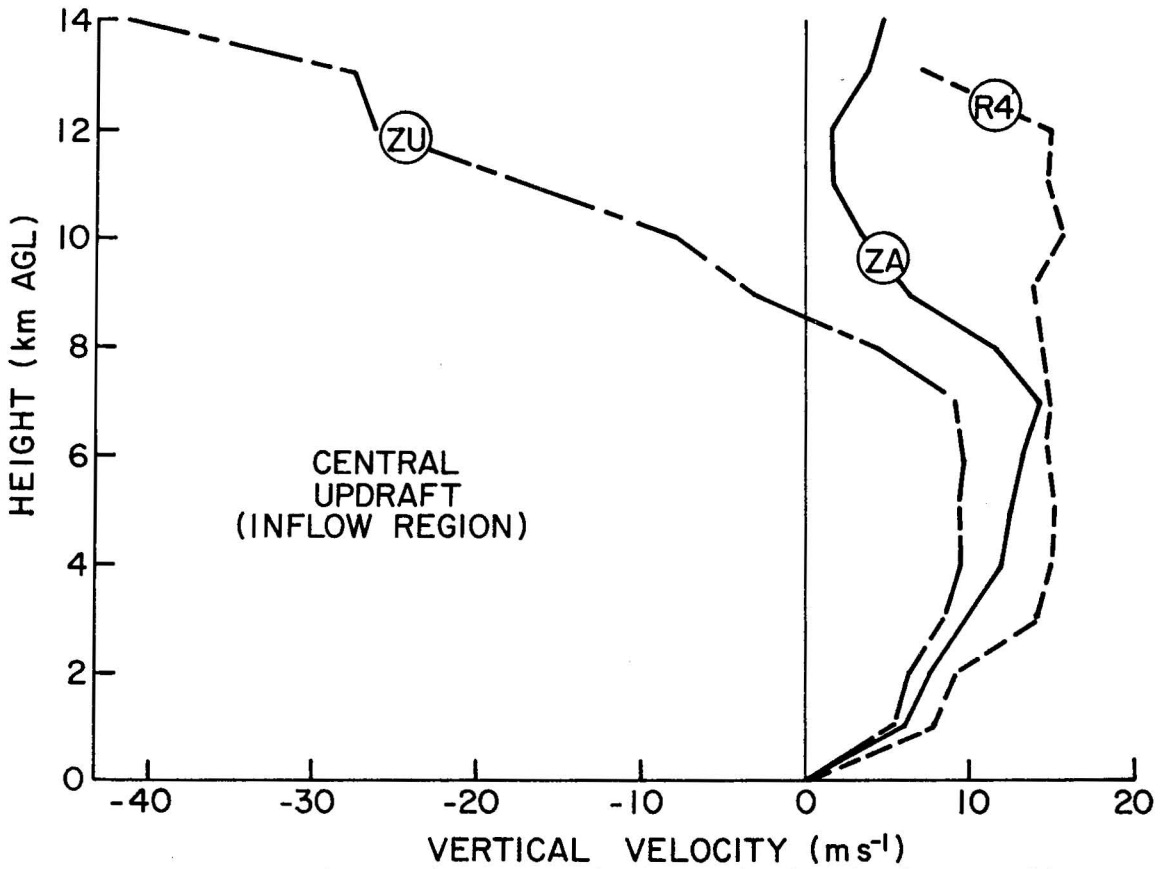

Figure 25. Central updraft (inflow region) vertical velocity profiles from two and four radar analyses. Label R4 corresponds to four Doppler Step 4 analysis, while labels "ZU" and "ZA" correspond to two Doppler unadjusted and adjusted analyses, respectively.

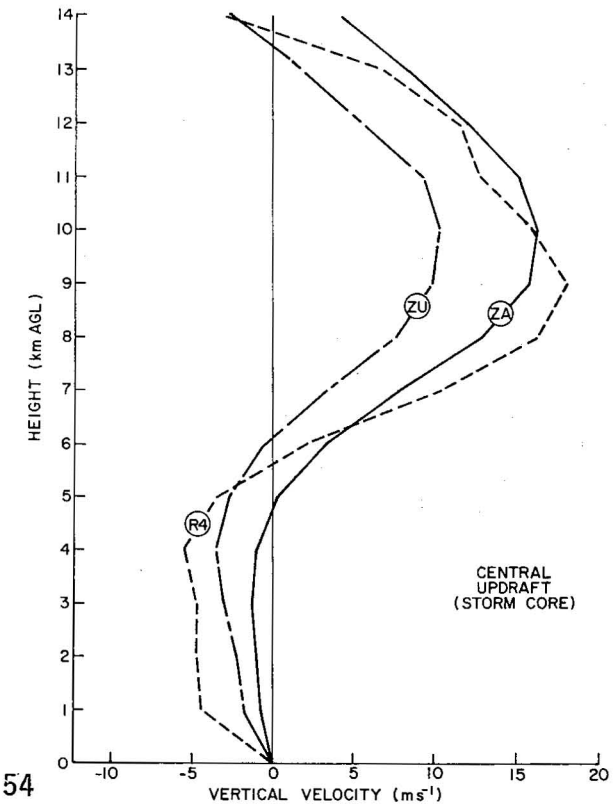

Figure 26. Same as in Fig. 25, but within storm core.

3.3 Case History - 28 May 1977

3.3.1 Introduction

On the afternoon of 28 May 1977, an isolated severe thunderstorm developed near Wynnewood in south central Oklahoma. The storm was unusual in that it produced large hail while moving slowly in a southerly direction, nearly 90° to the right of mid- and upper-tropospheric winds. Storm evolution was documented by dual Doppler and WSR-57 radar data, time-lapse movie footage, many still photographs obtained by ground intercept teams, and a limited number of infrared and visual satellite photographs. Other data included hail samples collected in real time by a ground chase vehicle within the precipitation shaft, and air samples and atmospheric parameters recorded on an instrumented aircraft flying near cloud base.

3.3.2 Synoptic Discussion

The principle features of the upper level flow are illustrated in Figs. 27 and 28. During the early morning of the 28th, the 850 mb analysis (Fig. 27a) showed a trough extending from the Dakotas southwestward to the Texas Panhandle. A closed circulation was indicated over western Oklahoma and eastern portions of the Panhandle. A belt of weak southerly winds to the east of the trough carried warm, moist air from the Gulf of Mexico over central Oklahoma. A dry intrusion was evident at 850 mb in southwestern Oklahoma. The morning 500 mb analysis (Fig. 28a) indicated that difluent flow with two branches was present over extreme eastern Kansas and southern Missouri. The northern branch was characterized by cyclonic curvature in relation to an advancing shortwave trough over the northern Rocky Mountains (not shown in Fig. 28a). The southern branch curved anti-cyclonically from western Texas across central Oklahoma. A minor shortwave trough in extreme eastern Oklahoma preceded warm advection over central and western Oklahoma and the eastern Panhandle region. Surface features on the morning of the 28th (not shown) generally reflect the 850 mb features.

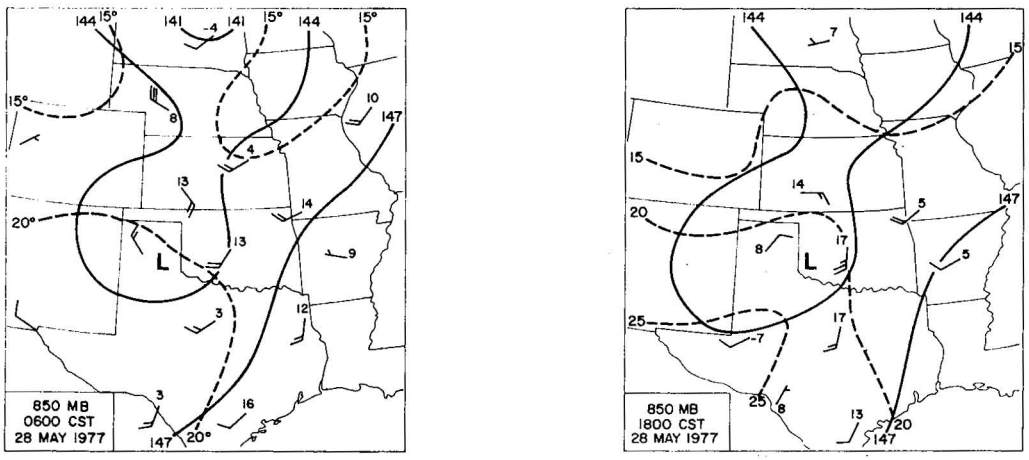

Figure 27. 850 mb analyses for 28 May 1977. Height contours (decameters) are solid. Isotherms (C) are dashed. Wind speeds are in knots. Dew-points (C) are plotted at selected stations.

A composite chart depicting major map features (Miller, 1972) was constructed to summarize the atmospheric state at 0600 CST on the morning of the 28th (Fig. 29). In Fig. 29a, jets are indicated by broad arrows. Maximum jet wind speeds (knots) are indicated at the arrow tail. The zig-zag broad line denotes a significant difluence zone. Solid arrows denote 850 mb jets. Hatched arrows and wavy line are respectively the 500 mb jet and zone of maximum anticyclonic shear. Cross-hatching denotes a 200 mb feature. In Fig. 29b, a wavy solid line indicates the 850 mb moist ridge. The thin line with hatching on one side indicates boundary of significant moisture at the 700 mb level. Solid dashed lines correspond to the 700 mb dryline while open dash-dot lines indicate the position of the same feature at the 850 mb level. To incorporate 12 hour LFM forecast information valid at 1800 on 28 May, thin lines show isopleths of absolute vorticity while the closed spiked curve indicates the expected region of maximum positive vorticity advection (PVA). Overlapping of 200 mb and 500 mb jets over Oklahoma coupled with a moderate dry intrusion over southern Oklahoma and dry overrunning of the 850 mb moist jet, are factors which in concert are very favorable to the development of deep convection. Speed shear is marginal over Oklahoma. Upper level anti-cyclonic shear zones have been associated with severe weather. These factors together indicate a likelihood of isolated severe storms in Oklahoma, east of the low level dry intrusion, by mid afternoon. In the absence of an upper level disturbance, these storms would not be expected to achieve tornadic intensity. With the arrival of the shortwave by 1800, storms might produce tornadoes. Horizontal warm advection at 500 mb (Fig. 28a) and probable weak subsidence on the right front quadrant of the 500 mb speed maximum, will actually decrease convective potential during the early afternoon in southern Oklahoma. The 850 mb and 500 mb charts for 1800 are presented in Figs. 27b and 28b respectively. At 850 mb, the moist ridge had shifted over central Oklahoma following the migration of the sub-synoptic low into western Oklahoma. Winds at Oklahoma City had backed 40° in 12 hours and intensified by 5 knots while the dewpoint temperature had risen 4 degrees. The rise of dewpoint temperature over north central Texas just east of the dry intrusion was nearly 14 degrees. Vigorous warm advection extended from SW Texas northeastward into

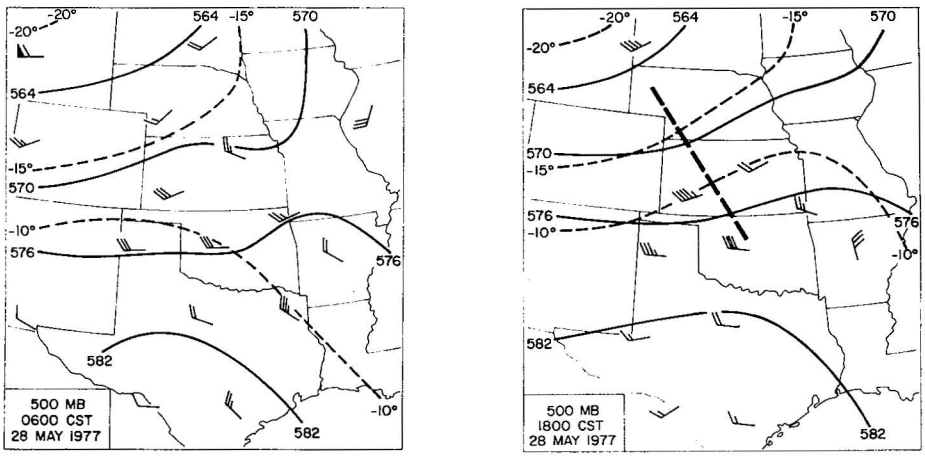

Figure 28. 500 mb analyses for 28 May 1977. Height contours (decameters) are solid. Isotherms (C) are dashed. Wind speeds are in knots. Heavy dashed line denotes shortwave.

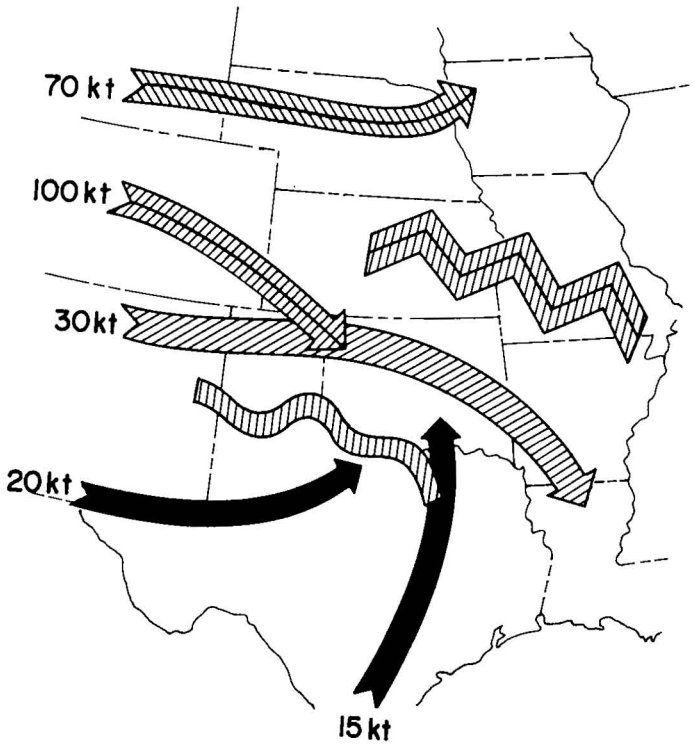

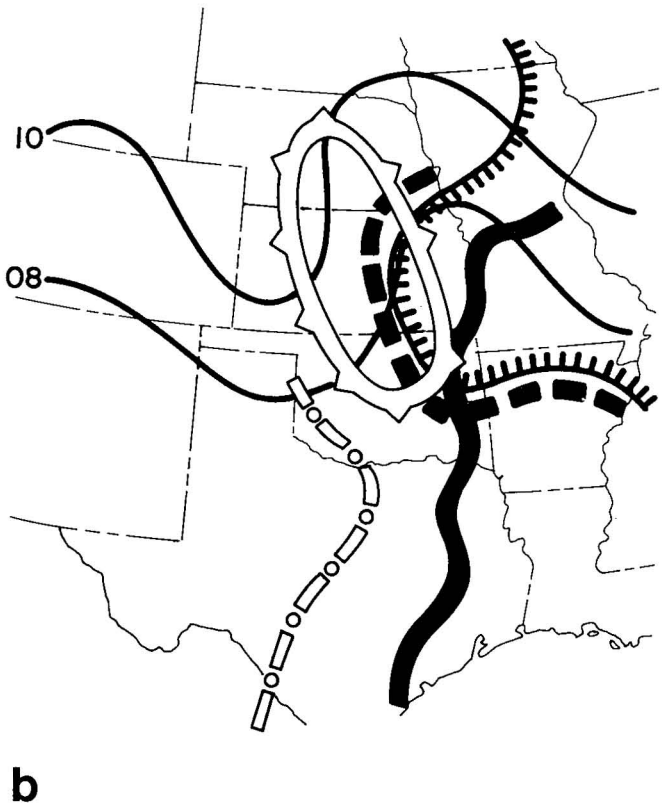

Figure 29. Composite chart for 28 May 1977. Upper panel: winds. Jets and wind maxima (arrows), difluence zone (zig-zag line), and anticyclonic shear zone (wavy line) at 850 mb (solid), 500 mb (hatched), and 200 mb (cross-hatched). Wind maximum (knots) at arrow tail. Lower panel: moisture and vorticity. Position of 850 mb moist ridge shown by solid, wavy line. Drylines at 850 mb/700 mb represented by open dash-dot and solid dashed lines, respectively. Thin line with tick marks encloses region of significant 700 mb moisture. Isopleths of absolute vorticity ($s^{-1} \times 10^{-5}$) and region of maximum PVA (closed, spiked curve) are derived from 12 hr. LFM forecast.

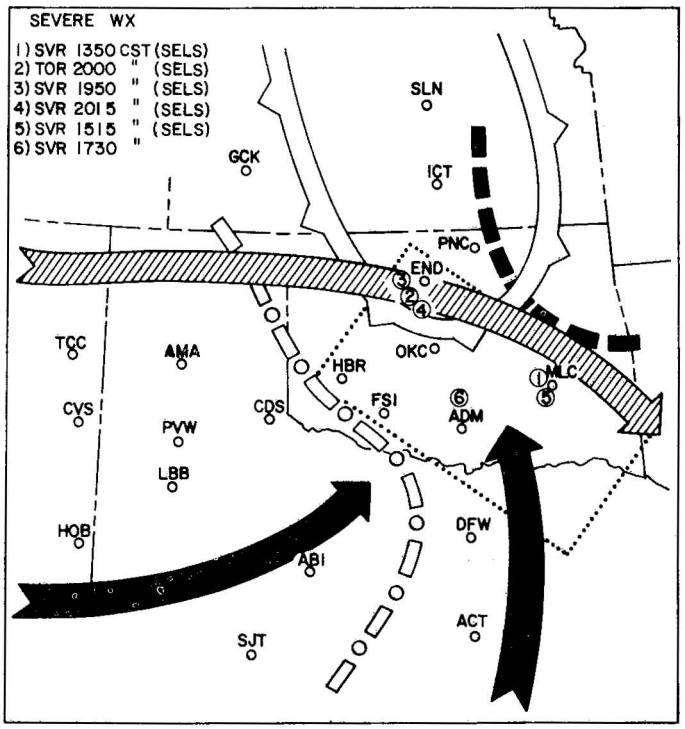

Figure 30. Relation of severe weather to major map features. Area of watch #158 is outlined with dots. Numbered circles show locations of corresponding events tabulated in upper left corner of figure. Selected upper air features are reproduced from Fig. 29.

the sub-synoptic low. The short wave trough had entered western Kansas and northwestern Oklahoma, and was characterized by moderate cyclonic speed shear and weak cyclonic curvature. Despite the advancing short wave, 500 mb heights over Oklahoma had experienced a net 12-hour increase because of warm air advection from the surface through 500 mb.

Figure 30 illustrates the relation of major map features to severe weather occurrences in Oklahoma on 28 May. The area enclosed by small dots corresponds to tornado watch number 158 issued by the National Severe Storms Forecast Center (NSSFC) at 1649, valid from 1700 to 2100. Severe events 1, 5, and 6 (which is the subject of this case study) occurred before the watch was issued. A tornado touched down near 2000 at Fairview, Oklahoma (event 2), within the watch box. This event was presumably triggered as a consequence of PVA east of the advancing shortwave. Event 6, characterized by large hail production, is conspicuously isolated both in space and time from the tornadic storm in NW Oklahoma. Among the conclusions drawn in the next section, is an apparent link between events 1 and 5 and the triggering of event 6, hereafter called the Wynnewood storm.

Surface map features for 1500 28 May are depicted in Fig. 31. A sub-synoptic low centered in SW Oklahoma was flanked on the west by a moderate intensity dryline and on the northeast by a mesoscale cold front induced by the thunderstorms in eastern Oklahoma. The scalloped curve encloses anvil cirrus of these thunderstorms as they appear from satellite photos (Fig. 32). The existence of a bubble high in extreme southeastern Oklahoma, western Arkansas, and southwestern Missouri is indicated from conditions at McAlester, Okla. (MLC), Fayetteville, Ark. (FYV), Springfield, Mo. (SGF), and Fort Smith, Ark. (FSM). The latter two stations are not plotted. The anvil cloud of the Wynnewood storm in south-central Oklahoma is clearly evident in the

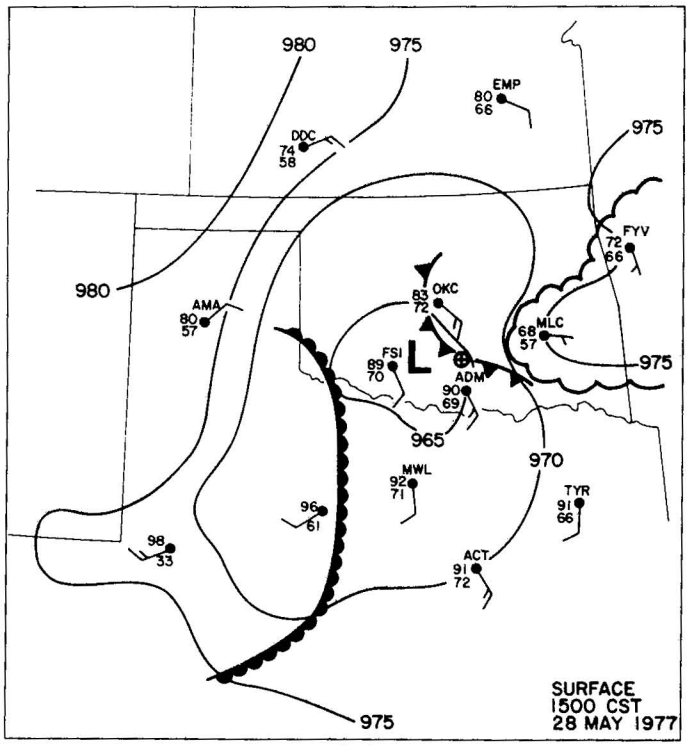

Figure 31. Surface weather features. Isopleths of altimeter setting (in) are labeled by suppressing both the left-most two and the decimal point. Curve faced with half-circles depicts dry line while spiked curve represents a mesoscale cold front. Scalloped curve encloses area of anvil cirrus. Winds (knots), temperature (C), and dewpoint (C) are shown at each station. Fiducial mark shows position of Wynnewood storm's first development.

GOES satellite photograph at 1700 (Fig. 32c). Also noted is a continuous north-south oriented band of cumulus and towering cumulus in northern Texas and southern Oklahoma that lies along the west flank of the Wynnewood anvil cloud. The cloud band may have been associated with a mesoscale confluence zone. The fiducial mark on the mesoscale cold front just north of ADM represents the location of first convective development of the Wynnewood storm. Figures 32a and 32b show a well defined arc-cloud along the leading edge of the mesoscale cold front. This arc-cloud moved southward at approximately 20 knots, and by 1500 (Fig. 32b) was producing towering cumulus along its southernmost portions. Figure 32c indicates that northeastern and central Oklahoma were entirely cloud free, while southern and western parts of Oklahoma experienced varying amounts of cumulus cloud cover.

The pronounced differences in low-level wind and atmospheric stability across Oklahoma as indicated by the observations, are illustrated by composite soundings in Figs. 33 and 34. Figure 34 shows profiles of temperature, moisture, and winds on a schematic skew T-log p chart based on radiosonde releases at 1330 from Fort Sill, Ok. (FSI) and the KTVY (TVY) instrumented tall tower located in Oklahoma City. Plotted soundings have been truncated above 500 mb. Surface temperature at TVY was 7° lower than at FSI. TVY wind was from 100°, as compared to FSI wind direction of 140°. At this time the mesoscale cold front had passed through Oklahoma City, explaining the differences between conditions at each station in low levels. Inversions at both sites between 800 and 900 mb capped a moist layer 75-100 mb thick. Temperature lapse rates beneath the inversion indicate that dry convective conditions prevailed within the boundary layer. Cumulus formation at each station purely from buoyancy considerations was unlikely, since a parcel rising from the boundary layer would encounter significant amounts of negative buoyancy

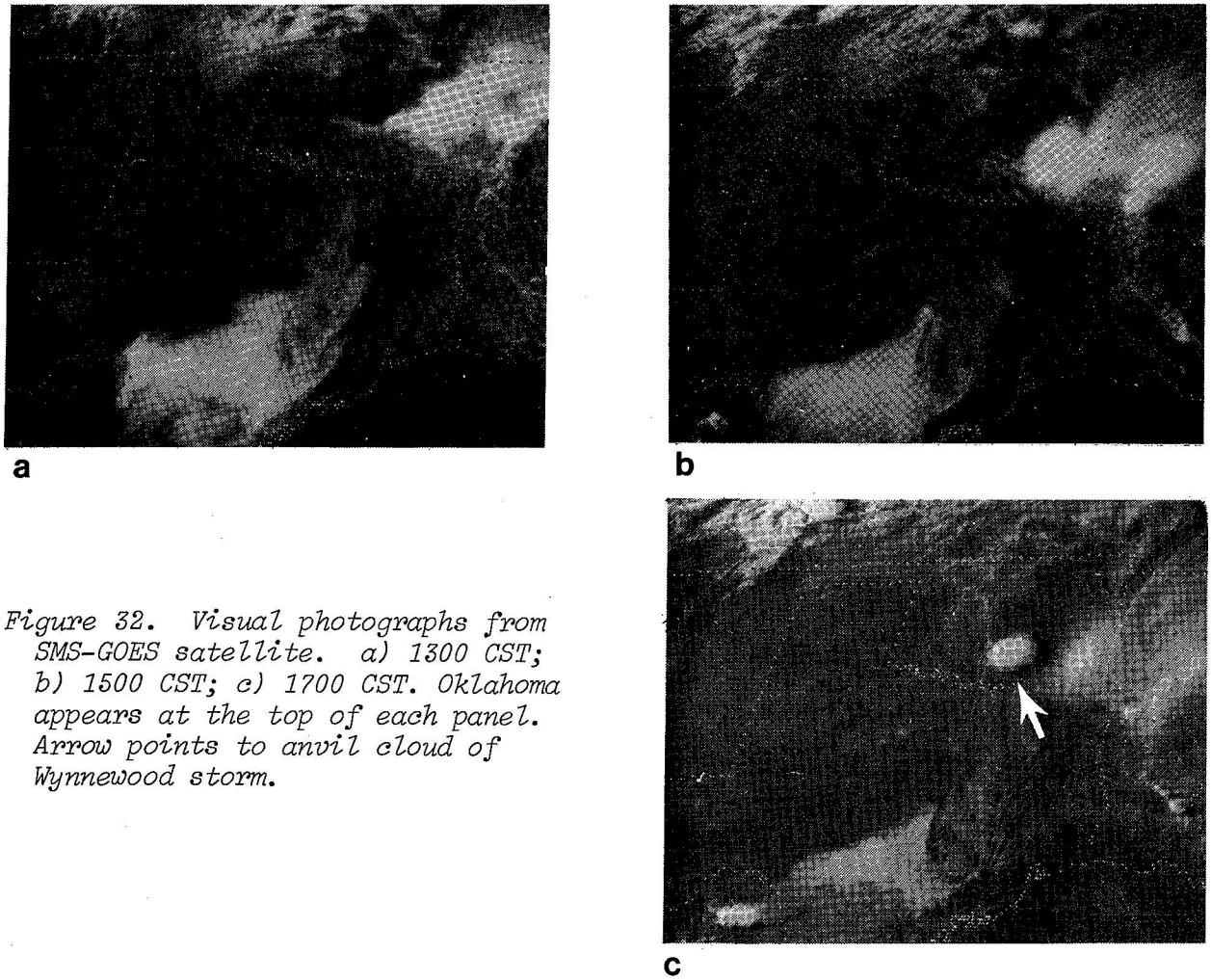

Figure 32. Visual photographs from SMS-GOES satellite. a) 1300 CST; b) 1500 CST; c) 1700 CST. Oklahoma appears at the top of each panel. Arrow points to anvil cloud of Wynnewood storm.

before the lifting condensation level (LCL) or level of free convection (LFC) could be attained. Winds at TVY and FSI were southerly below the inversion, rapidly veering to a westerly direction above. Figure 33 depicts soundings taken at Elmore City, Ok. (EMC) at 1330 and 1641. They are particularly representative of conditions on the high level upwind flank of the Wynnewood storm. The EMC 1330 sounding is quite similar to the FSI sounding in Fig. 34, especially in terms of depth of moist layer and near dry-adiabatic boundary layer, surface temperature, conditional instability, and wind profile. A significant difference is the relative weakness of the capping stable layer at 1330 over EMC. Between 1330 and 1641 at EMC, the moist layer deepened dramatically from a top near 850 mb to approximately 710 mb. The weak stable layer was nearly eliminated in this 3-hour period. Since the LCL and LFC nearly coincided, instability could rapidly be achieved. The lifted index was -7 at 1641, hence vigorous updrafts could be realized. In summary, thermodynamic conditions were most favorable for the onset of deep convection during mid-afternoon in south-central Oklahoma.

A hodograph derived from the EMC 1330 sounding is presented in Fig. 35. Pronounced veering with height and weak speed shear, are evident. The storm motion was from 15° at 5.4 m s^{-1} between 1610 and 1830, as determined from visual correlation of successive WSR-57 PPI photographs. The cloud-bearing layer extended from 1 to 13 km AGL (see Fig. 33). The mean wind of the

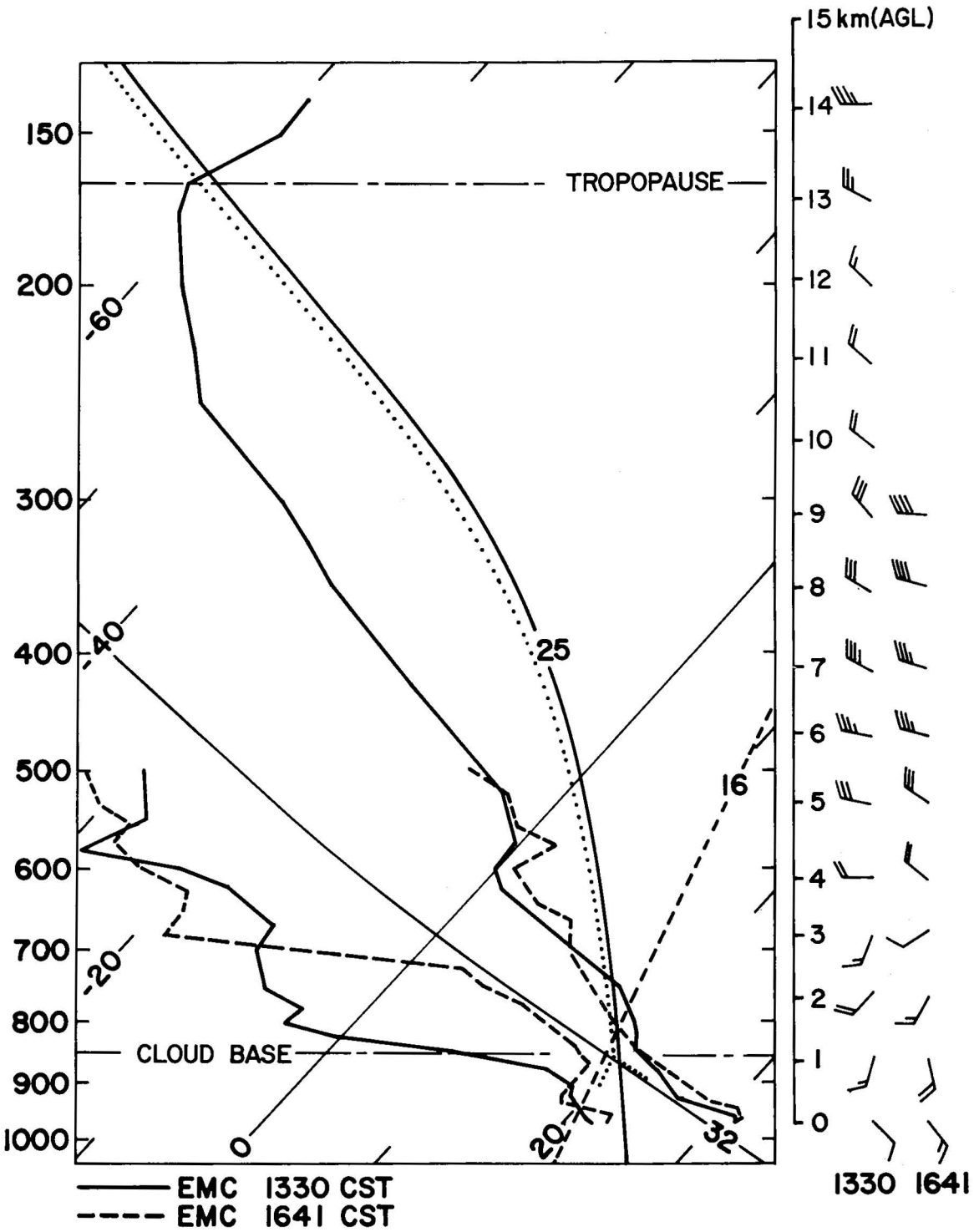

Figure 33. Composite of EMC soundings on schematic skew T-log p diagram. Solid profiles are for 1330 while dashed profiles are for 1641. Dotted lines are temperature and dewpoint profiles from parcel theory. Winds (right margin) are in knots.

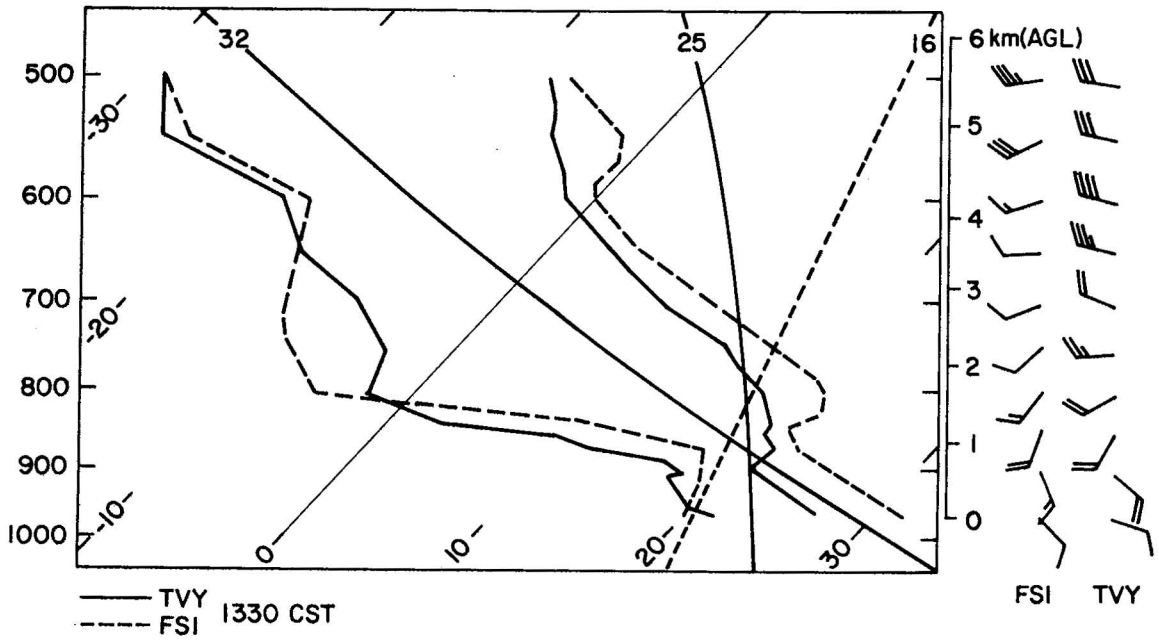

Figure 34. Composite of FSI and TVY soundings. All labeling is the same as in Fig. 33, except that FSI sounding is dashed while TVY sounding is solid. Both soundings have been truncated above 500 mb.

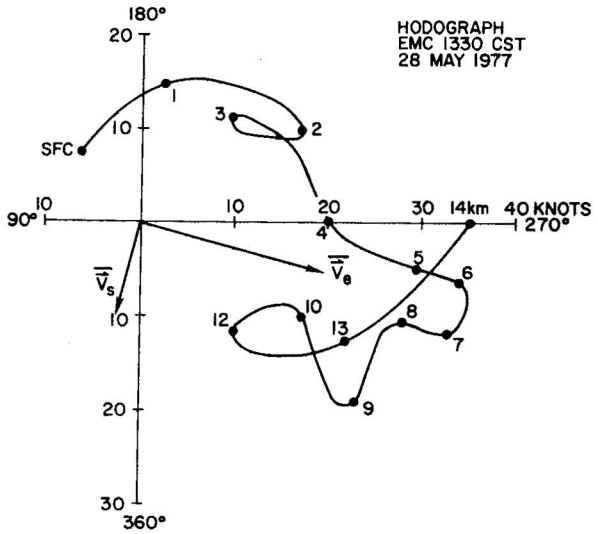

Figure 35. Wind hodograph from EMC sounding. Date and time appear in upper right corner. Speed (knots) and direction of mean wind ($\bar{V}_e$) and storm movement ($\bar{V}_s$) are indicated.

cloud-bearing layer, based on a vector average of winds at 1 km intervals in the vertical, was determined to be from 285° at 10 m s^{-1}. The Wynnewood storm moved 90° to the right of the mean wind. This anomalous motion must be due to propagation. The corresponding propagation vector is from 85° at roughly 12 m s^{-1}. Photographs taken by ground intercept teams (Fig. 36) and time lapse photography from NSSL indicated that the most intense and persistent cloud development occurred on the storm's west and southwest flanks. This observation lends support to the conclusion that westward propagation was responsible for the extreme right-moving tendency of the Wynnewood storm.

b

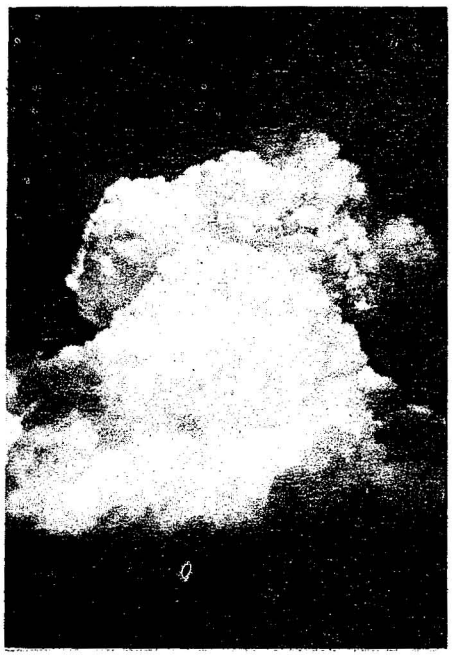

a

c

Figure 36. Convection on west flank of Wynnewood storm as viewed by ground intercept teams. a) near Elmore City, OK at 1655 looking east; b) near Lindsay, OK at 1720 looking southeast; c) near Elmore City, OK at 1810 looking southwest. NSSL-OU Tornado Intercept Project Photos.

3.3.3 Echo Evolution

Dual Doppler radar data was collected from the Wynnewood storm between 1720 and 1845 CST. Satellite photos, ground intercept team observations, and WSR-57 PPI photographs establish that sustained deep convection commenced at 1515 and ended between 1830 and 1900. The WSR-57 first echo appeared at 1530 in cloud mid-levels. Recall that vigorous penetrating tower activity was noted from time lapse photos near this time. The lead time between onset of deep convection and formation of hydrometeors of radar-detectable size, was approximately 15 minutes. Between 1530 and 1600, the main echo grew in areal coverage while elongating along the direction of the mean wind. Initial echo motion was quite slow and in the direction of the mean wind. Near 1600, a small echo rapidly developed on the NW or upwind flank of the main echo. By 1610, this echo had become detached while the main echo turned abruptly towards the south. The small, break-away echo became elongated and moved with the mean wind until 1645 when it rapidly collapsed. The small echo was then downwind of the large echo relative to the low level inflow, and its demise probably resulted from being cut off from the supply of potentially unstable low level inflow. After 1550, small echos began appearing southwest of the main echo, initially separated from the south flank of the main echo

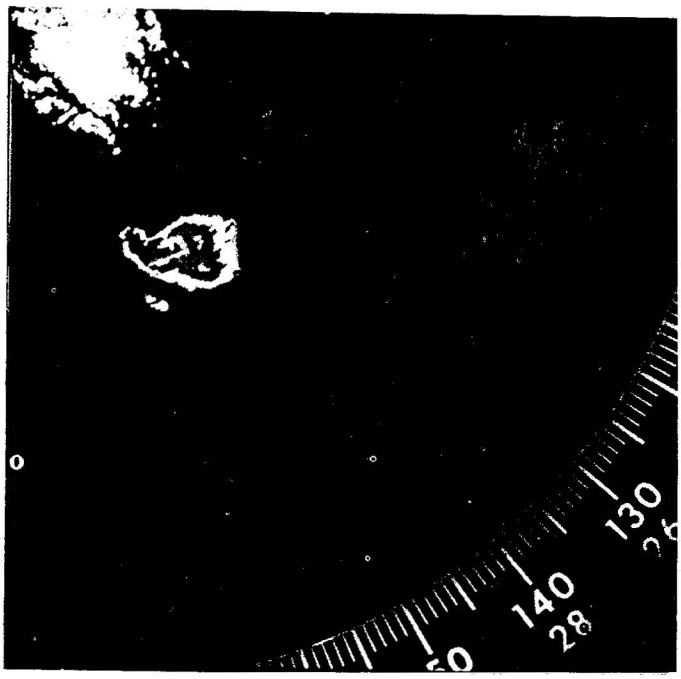

Figure 37. Norman WSR-57 integrated received power at 1719 on 28 May 1977. PPI display at 0° elevation.

by between 5 and 10 km. Once formed these echoes proceeded to rapidly merge with the main echo. Between 1550 and 1800, five such initially discrete echoes formed. The merger was evidently the result of the larger cell overtaking the small cell since the average merger velocity was nearly identical to the main echo motion vector. The storm motion vector remained nearly constant between 1610 and 1830. The main echo was observed to propagate continuously at all times. From these observations it is concluded that storm propagation was essentially a result of continuous generation of new convection on the southwest and west flanks of the large cell, with discrete propagation playing a minor role in determining storm motion. After 1830, the echo decreased in intensity and turned toward the east (by 1900, mid- and upper-level winds had backed from WNW to W). Maximum storm intensity was evidently between 1700 and 1730 when a fourth level WSR-57 echo maximum (equivalent to intensities ranging between 58 and 64 dBz) formed in storm mid-levels and eventually descended to the ground. The WSR-57 0° PPI view of the storm at 1720 appears in Fig. 37. This maximum disappeared at 1730 and did not reappear during the remainder of the storm's lifetime. Observations from ground observers at Norman indicated that all precipitation was from stratiform anvil cloud by 1900. Although the 0° PPI echo only gradually diminished, it was apparent that deep convection had ceased by 1900.

3.3.4 Presentation of Dual Doppler Fields

Radial velocity and reflectivity information obtained by the Norman and CHILL Doppler radars from the Wynnewood storm have been objectively analyzed. In this section, results of the variational objective analysis corresponding to coordinated tilt sequences centered at 1719, 1743, 1800, 1816, and 1832 are presented with discussion. The map locating surface observing sites and the analysis grid position at 1719 are shown in Fig. 38. It is apparent that data collection did not commence until the storm reached the stage of greatest intensity and that late observations correspond to the period of net storm

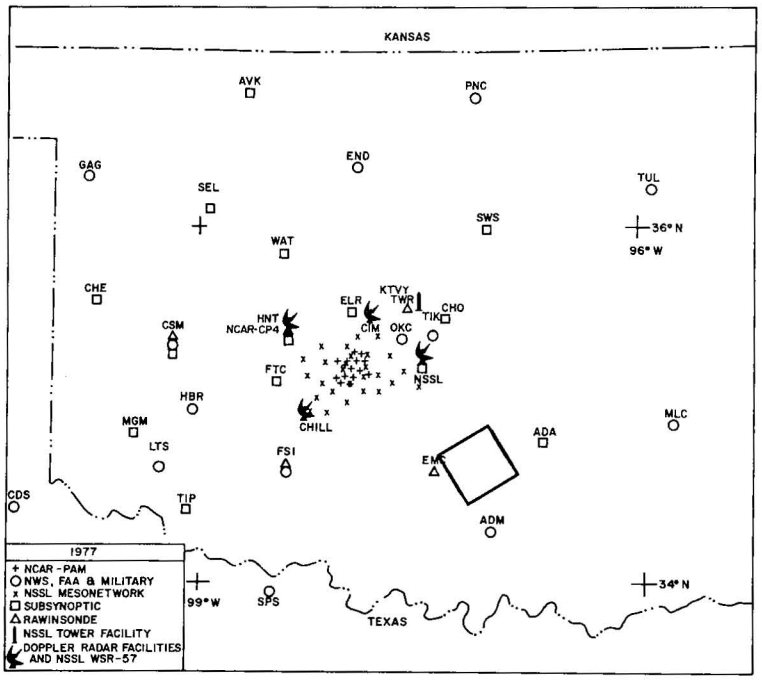

Figure 38. Schematic locating observing sites and dual Doppler analysis domain (northwest-southeast oriented square).

decline. The Norman Doppler collected usable data for returned, range-normalized log signal intensity greater than or of order unity. Returned signals at the CHILL were thresholded such that, in essence, information at gates for which intensity dropped below order 15 dBz was rejected. The peripheries of the storm echo are not well-defined in the dual Doppler analyses as a consequence. In addition, the effort to determine winds in and above weak reflectivity inflow regions of the storm, e.g., flanking line, is severely hampered. Conventionally derived wind estimates are displayed only in low and mid-storm levels, and then only when adjusted wind estimates are unavailable. Extremes of unadjusted vertical velocities in storm core regions will be referred to for comparison with adjusted vertical velocities.

Figure 39 contains displays of storm-relative horizontal winds and equivalent reflectivities in selected horizontal planes at 1719. Figure 40 is composed of selected vertical cross-sections of storm-relative winds within the section and equivalent reflectivities, at 1719. As indicated in Fig. 39a (2 km plane), two strong cells are centered at the coordinates (13, 16) and (2, 18), hereafter referred to as Cells I and II, respectively. Low numerals will be assigned to older cells. Cell I has higher intensities, greater horizontal and vertical extent, and is more erect than Cell II. Strong divergence and convergence zones are associated with Cell I at 2 km, and are centered at (13,13) and (10,13), respectively. Their order of magnitude is 7×10^{-3} s^{-1}. At mid-levels (Figs. 39b,c) an area of locally high southerly momentum centered at (11,16) exists within the upshear side of Cell I. This area coincides with strong updrafts. Strong westerly winds on the storm's south and north flanks are nearly identical to mid-level environmental winds as revealed by the Elmore City 1641 sounding (Fig. 33). A pronounced wake flow extends roughly 20 km downstream from Cell I at 7 km. Locally high values of positive relative vorticity exist on the southwest flank of Cell I, roughly 6 km from the core. A characteristic value of

relative vorticity in this region is 1 x 10^{-3} s^{-1}. At 7 km, a closed anticyclonic eddy is located roughly 4 km downstream of the core of Cell I, with generally high values of anticyclonic relative vorticity in existence on the east and northeast flanks of Cell I. The negative relative vorticity within the eddy is -1.2 x 10^{-2} s^{-1}. Flow diverges around Cell I on its upshear side. The circulation associated with Cell I is strongly asymmetric. Air flows from the south into Cell I, while the strong north-flank jet flows smoothly past Cell I. A pronounced reflectivity gradient on the north flank of Cell I appears to be closely related to the jet location. At the 13 km level (Fig. 37d) which corresponds to the tropopause, intense divergence is found with Cell I while weaker divergence and some upshear flow are found in Cell II. A region of positive vorticity in the outflow at (9, 11) is associated with a divergence of -7 x 10^{-3} s^{-1}. This magnitude is also typical of divergences in the north flank outflow, which has relatively little vorticity associated with it. The horizontal winds in Cell II exhibit a veering with height and downshear divergence at upper levels. Although horizontal momentum in low-levels of Cells I and II is southerly, Cell II is characterized by appreciably more westerly momentum than Cell I at mid-levels. A prominent feature of the reflectivity structure of Cell I in low and mid-levels are the two ridges of high reflectivity extending downshear with the south and north flank jets. They are separated by a finger-like intrusion of weak echo that reaches upstream toward Cell I and coincides with the wake of Cell I. This reflectivity pattern may be partly due to differential horizontal advection of hydrometeors.

Figure 40 shows selected vertical cross-sections at 1719. Figure 40a offers a plan view of each section with the 3 km horizontal intensity contours superimposed to provide reference to key storm features. Letters denote cross-section lateral boundaries. The A-B section in Fig. 40b is viewed looking west-southwest i.e. upshear. Horizontal southerly inflow forms a layer from the surface to 4 km. High-level outflow resides in a 3 km deep layer. Two nearly erect updraft plumes separated by 8 km are apparent. The northernmost updraft has a maximum of 46 m s^{-1} at 9 km, just above the low level precipitation shaft and underneath the outflow plume near 15 km. Weak updrafts are observed to the north of the strong reflectivity gradient and below 6 km. The southern updraft has a peak value of 39 m s^{-1} at 10 km. The regional peak updraft, with the value of 61 m s^{-1} at 11 km, is not contained in the A-B plane. The core of maximum reflectivity tilts slightly towards the south with height. The 55 dBZ contour extends to 11 km, while outlining a mid-level overhang extending south from the core a distance of 4 km. The north flank gradient is essentially vertical through 9 km. Horizontal protuberances of weak reflectivity extending away from the core to the south and north (see for example Fig. 40c above 6 km) are the radar-visible core of the expanding storm anvil. They are formed by the injection of hydrometeors into the upper levels by the strong updrafts, and their subsequent advection outward in the outflow layer. Settling of hydrometeors following the motion results in echo tops that slope downward and away from the outflow center. Section C-D, oriented roughly south-to-north and parallel with storm motion, is quite similar to section A-B. The maximum equivalent reflectivity associated with Cell I is 64 dBZ at 7.0 km. Strong updrafts coincide with highest reflectivities. The local updraft maximum of 43 m s^{-1} is achieved immediately above the maximum reflectivity at an altitude of 8.0 km. The updraft within Cell I tilts from south to north with increasing

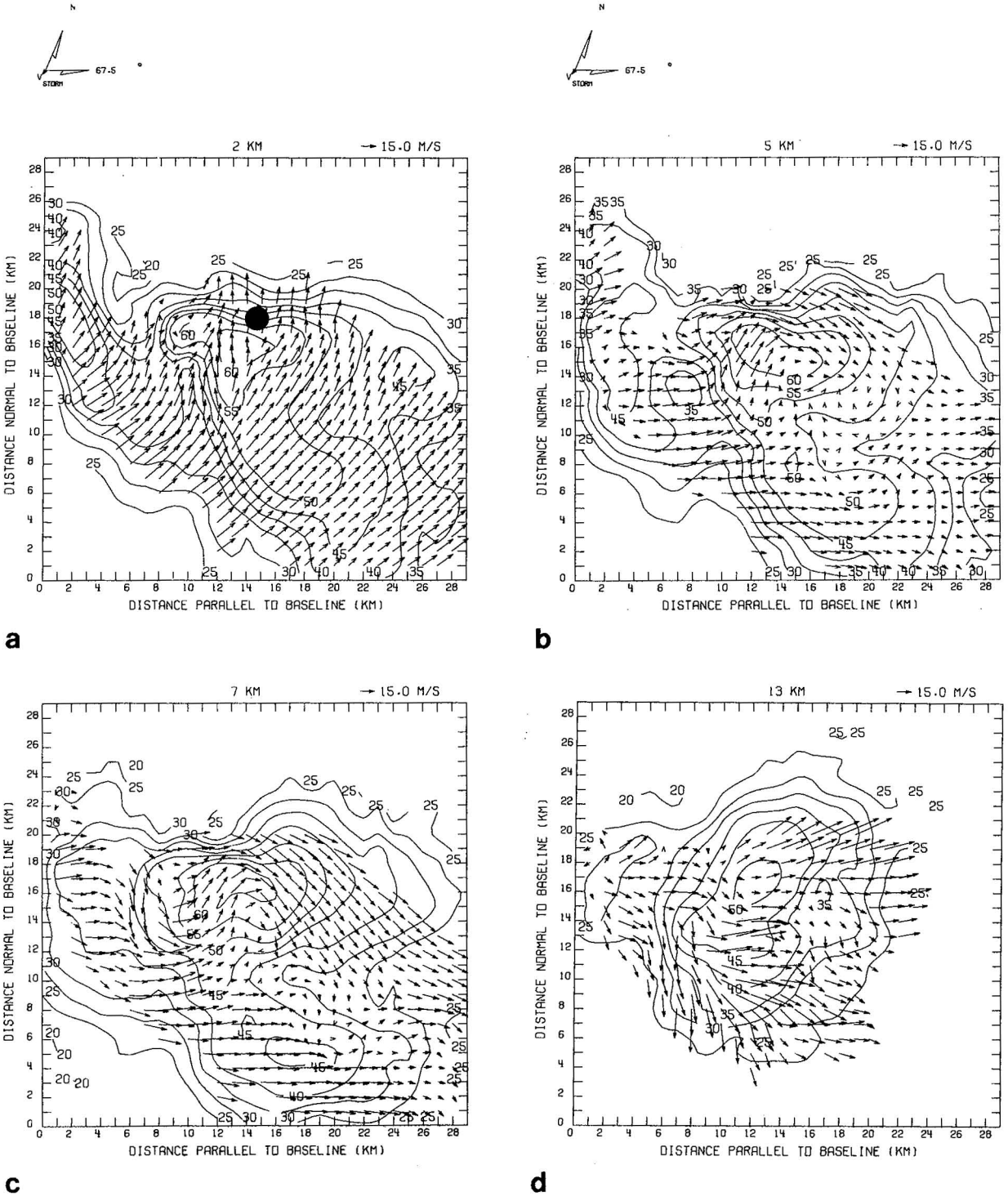

Figure 39. Horizontal winds and reflectivities from two Doppler variational analysis at 1719. Heights are indicated at top of each panel. One grid length equals 15 m s^{-1}. Reflectivity is contoured as 10 log (Z). Mean storm motion (5.4 m s^{-1} toward 195°) component has been removed. Compass indicates north toward top of page. Grid origin is in lower left corner of each panel.

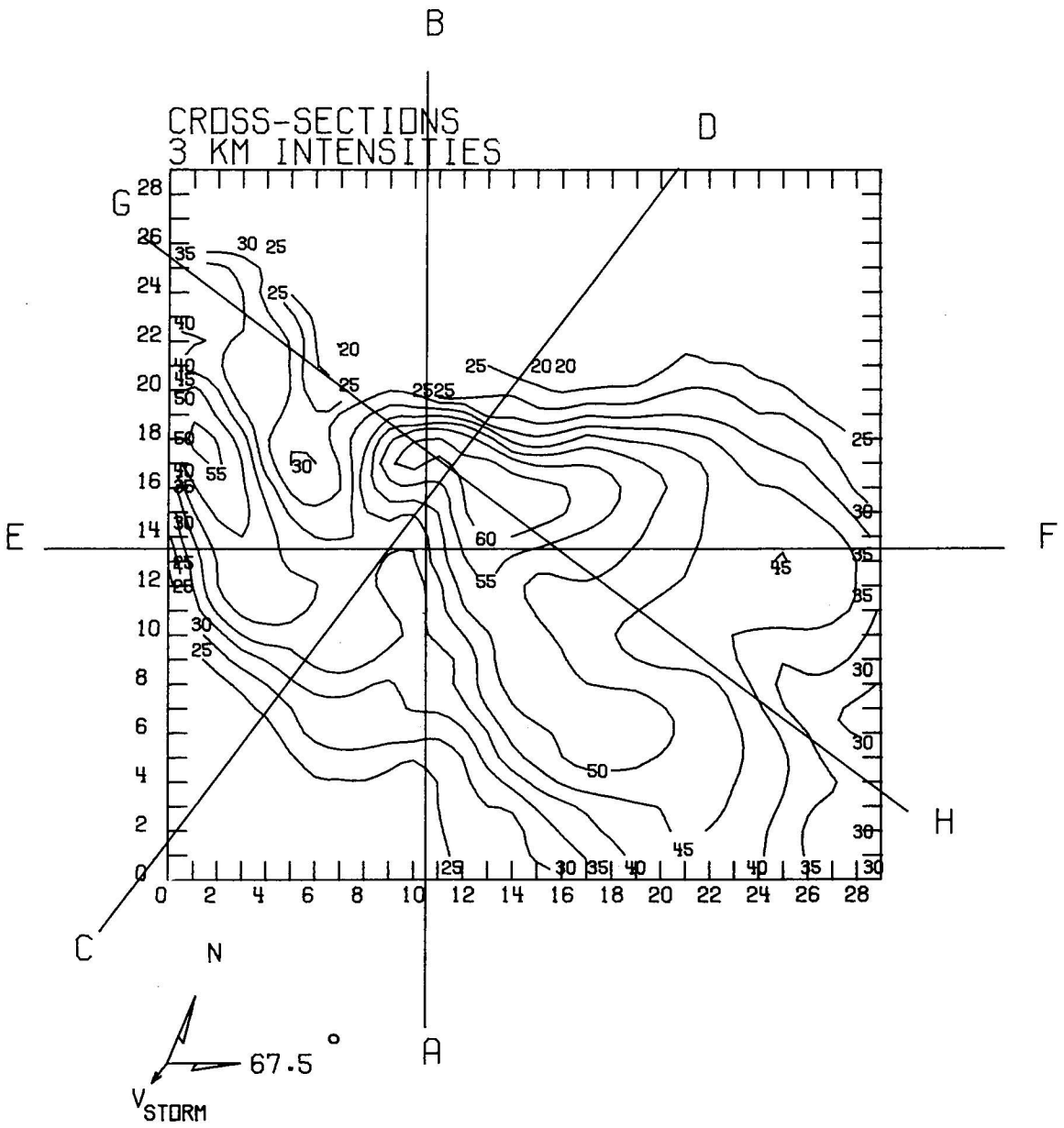

a

Figure 40a-e. Vertical cross-section through two Doppler analysis at 1719 as indicated in Fig. 40a. Upper panel: reflectivity contoured as 10 log (Z); Lower panel: winds. Mean storm motion component has been removed. Velocity vector length scale in upper right corner.

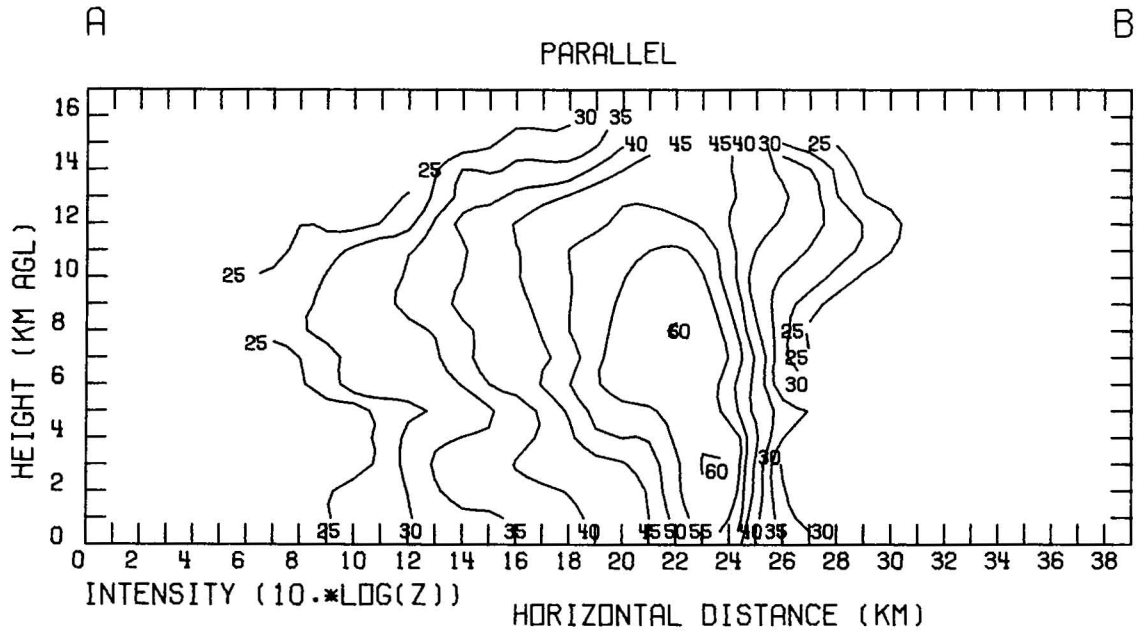
A
B
PARALLEL
HEIGHT (KM AGL)
INTENSITY (10.*LOG(Z))
HORIZONTAL DISTANCE (KM)

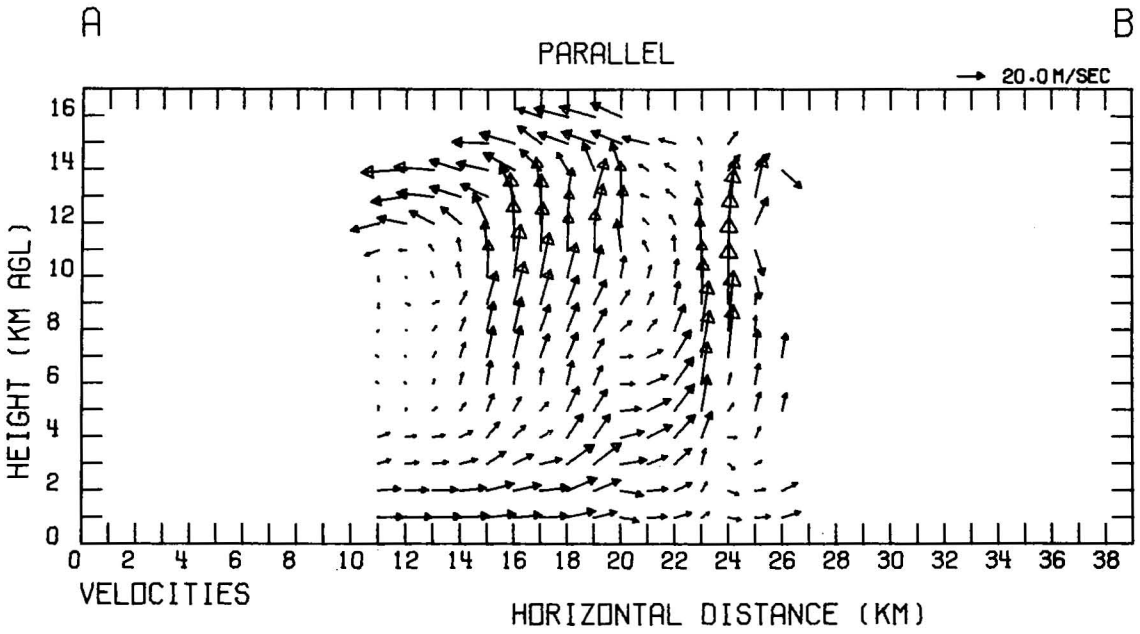
A
B
PARALLEL
20.0 M/SEC
HEIGHT (KM AGL)
VELOCITIES
HORIZONTAL DISTANCE (KM)

b

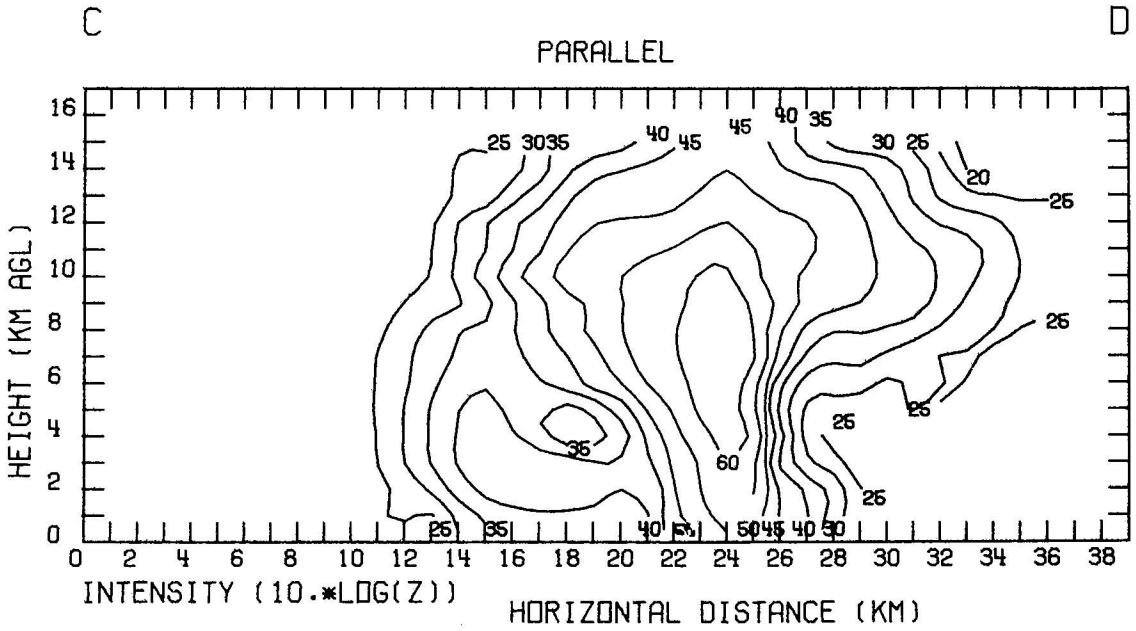
C
D
PARALLEL
HEIGHT (KM AGL)
INTENSITY (10.*LOG(Z))
HORIZONTAL DISTANCE (KM)

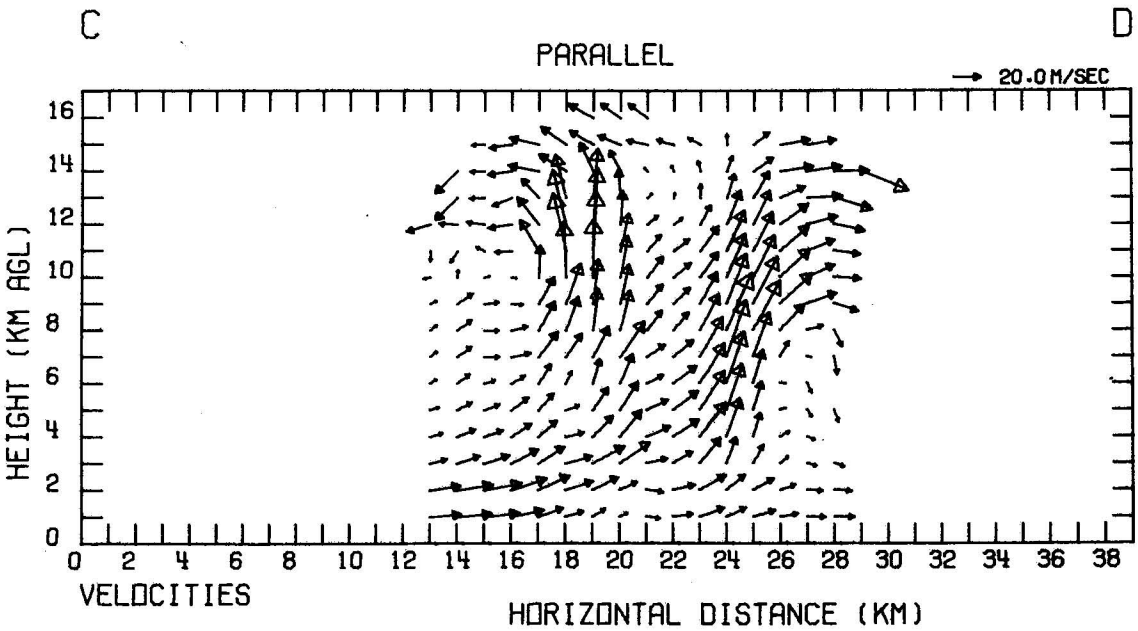
C
D
PARALLEL
20.0 M/SEC
HEIGHT (KM AGL)
VELOCITIES
HORIZONTAL DISTANCE (KM)

C

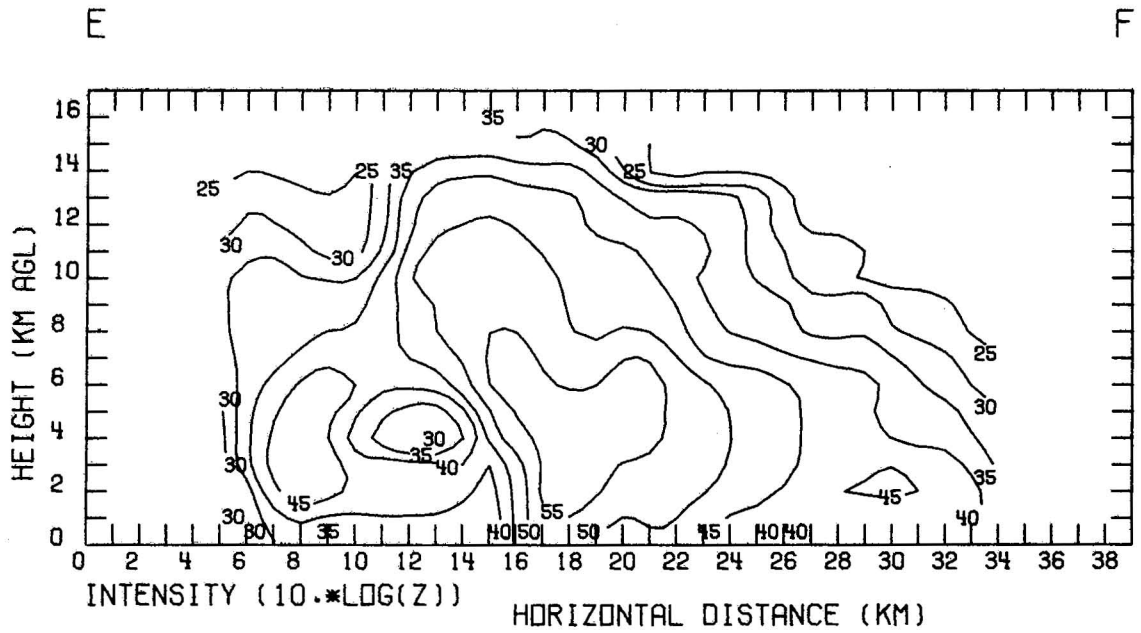
E
F
HEIGHT (KM AGL)
INTENSITY (10.*LOG(Z))
HORIZONTAL DISTANCE (KM)

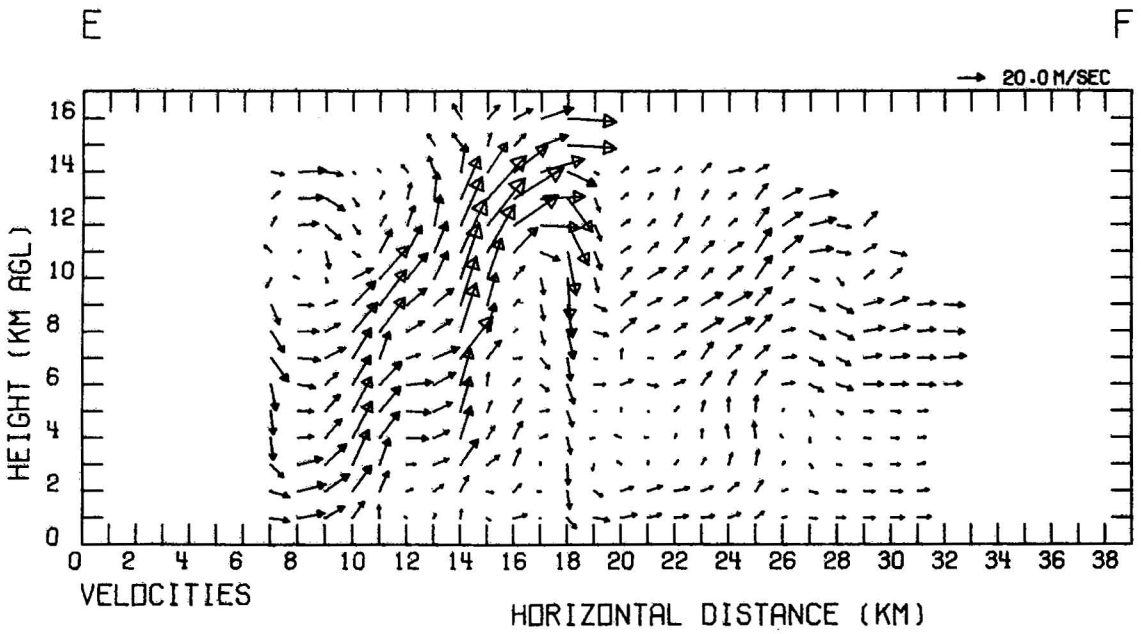
E
F
20.0 M/SEC
HEIGHT (KM AGL)
VELOCITIES
HORIZONTAL DISTANCE (KM)

d

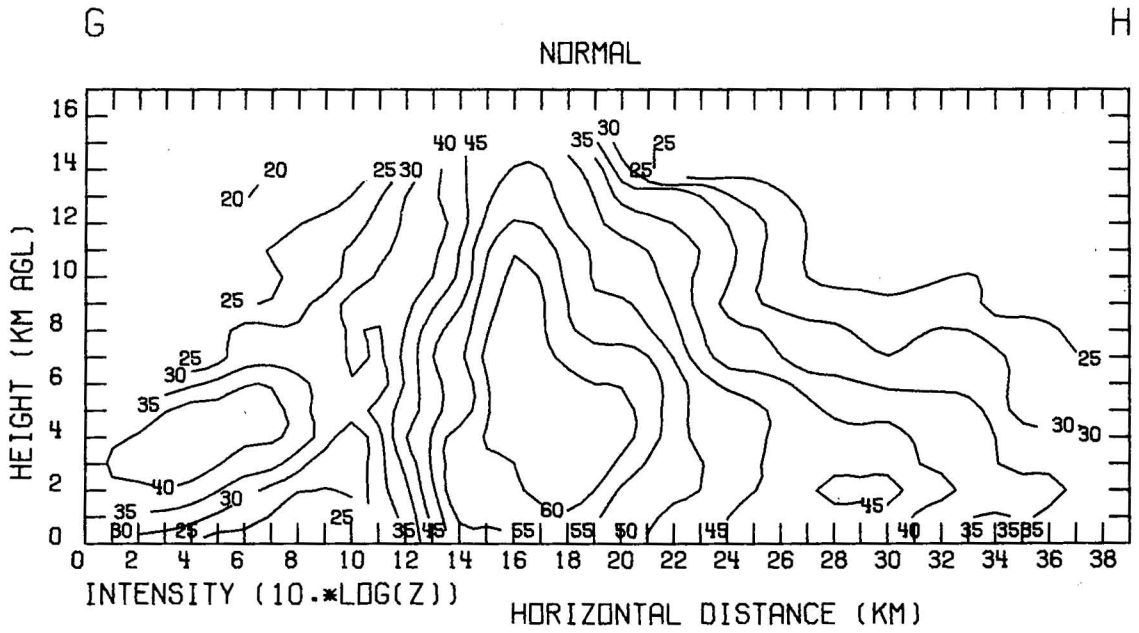
G
H
NORMAL
HEIGHT (KM AGL)
INTENSITY (10.*LOG(Z))
HORIZONTAL DISTANCE (KM)

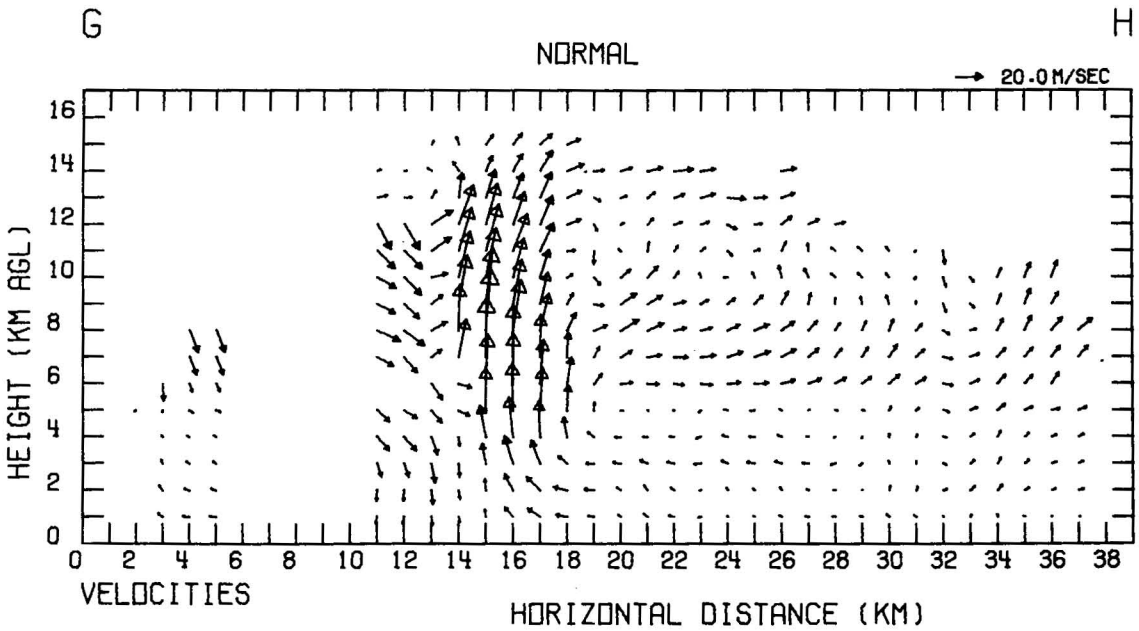
G
H
NORMAL
20.0 M/SEC
HEIGHT (KM AGL)
VELOCITIES
HORIZONTAL DISTANCE (KM)

e

altitude, extending above the north flank reflectivity gradient. At high levels this updraft diverges outward, forming a deep, strong northward outflow layer extending from 8 km to 15 km AGL. Since winds at all levels within and to the north of Cell I are southerly, precipitation in the northern portion of the anvil probably originated in Cell I. Figure 40d is the view looking NW. Intense convection originates on the storm southwest flank in Cell II. The outflow from the updraft in Cell I is predominantly to the northeast. The storm scale updraft resulting from the combination of Cell I and Cell II updrafts tilts downshear roughly 30° within the plane. The strongest plumes tend to be more erect. A strong, deep, compensating downdraft is located 4 km downshear from the Cell I updraft. A portion of this downdraft does extend to the ground although its greatest width and intensity (3 km, -42 m s^{-1}) occurs near 11 km. Strong updrafts on the west side of Cell I are associated with a reflectivity maximum aloft, while downdrafts to the east allow the precipitation core to descend to the ground. Consequently, Cell I reflectivity structure tilts to the west with height. The updraft appears to be a region of hydrometeor generation and accumulation, based on the correlations between high level reflectivity maximum and strong updrafts. Cell II, on the storm southwest flank, is in the developing stage. Maximum updraft and equivalent reflectivity there (not in the E-F section) are respectively 28 m s^{-1} at 4 km and 56 dBZ at 3 km. The top of Cell II tilts downshear. Figure 40e is the view looking north-northeast, normal to the storm motion. The intense, erect updraft (maximum of 46 m s^{-1} at 8 km) in Cell I coincides precisely with the columnar, vertical reflectivity core (highest maximum is 64 dBZ at 7.0 km). Flow converges into the updraft on its east flank through 4 km. A layer of westerlies from 6 km to 9 km corresponds to the north flank jet (Fig. 39c) which sweeps around the blocking updraft and enters the thunderstorm echo in the downstream wake region. Horizontal flow converges at the upshear flank of the updraft at all levels except near 14 km in the outflow layer. The slope of the radar-visible storm top downshear from Cell I suggests that significant numbers of hydrometeors are carried downstream. The pronounced upshear-flank reflectivity gradient may be partly maintained by the horizontal wind convergence.

Figures 41 and 42 show storm state at 1743. Cell I is collapsing, while Cell II on the storm west flank now contains the strongest convection. In Fig. 41a, diffluence in the vicinity of (14, 17) is associated with downdraft remnants of Cell I. A new echo merging with the storm's southwest flank is located at (3, 7). Low level winds are generally from the south. At mid-levels, reflectivity maxima at (9, 20) and (16, 17) are respectively the core of Cell II and the collapsing top of Cell I. Strong veering of environmental winds is reflected in the wind profile within the merging cell at (3, 7). Westerly winds flank the storm on the north and south. As at 1719, the north flank jet enters the storm in a strong reflectivity gradient. A well-developed wake return current flows directly toward Cell II from as far as 14 km downshear, and over much of its course directly opposes the flanking jets. Cyclonic curvature within the merging cell at 7 km may be due to flow around the blocking updraft in Cell II. An anticyclonic eddy is evident at mid-levels near (17, 15), immediately downshear from the collapsing top of Cell I. There is pronounced divergence at 13 km, and the outflow source near (9, 17) coincides with the maximum reflectivity. The C-D cross-section (Fig. 42c) shows the principal updraft tilted from south to north in the plane, with a

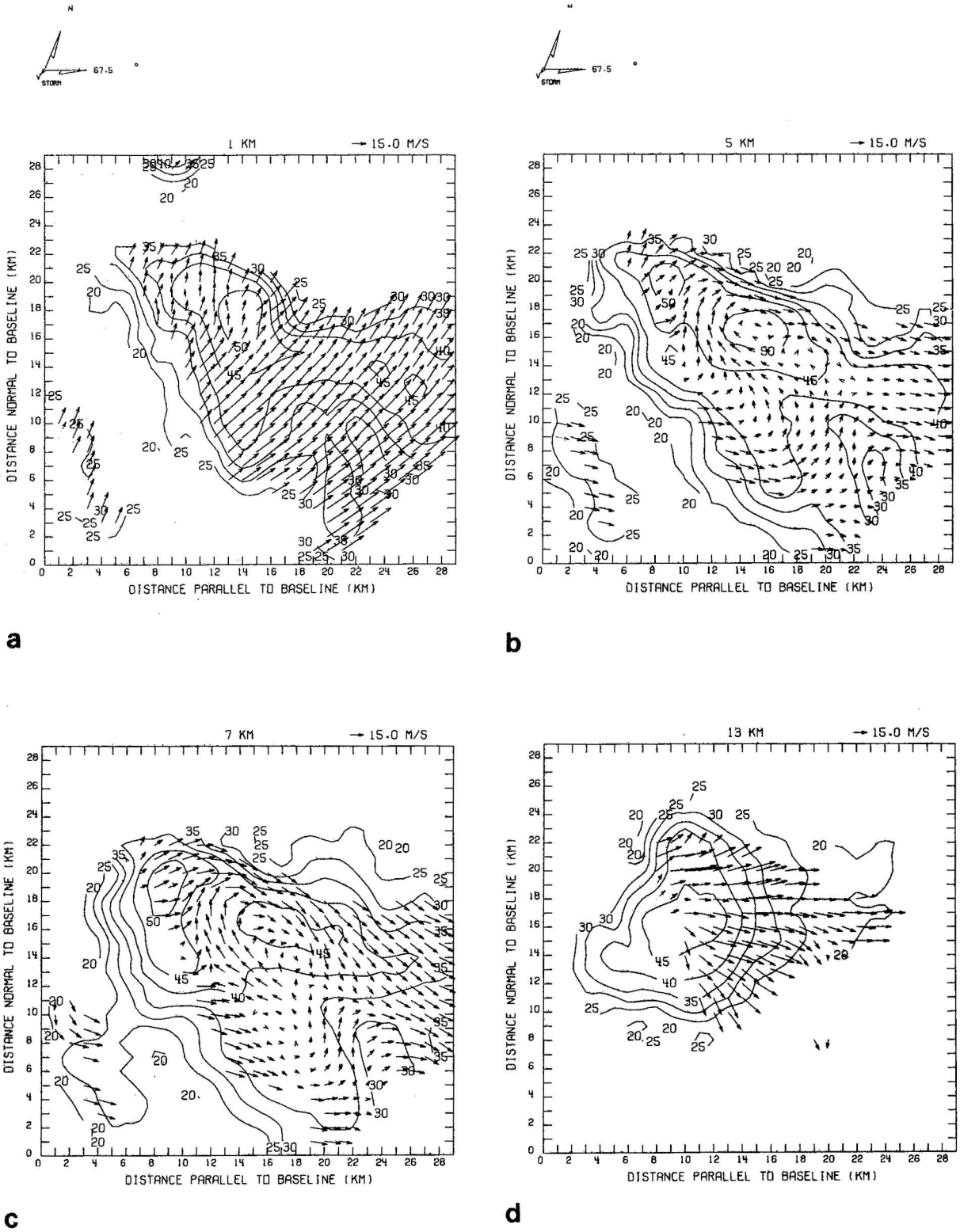

Figure 41. Same as in Fig. 39, but at 1743.

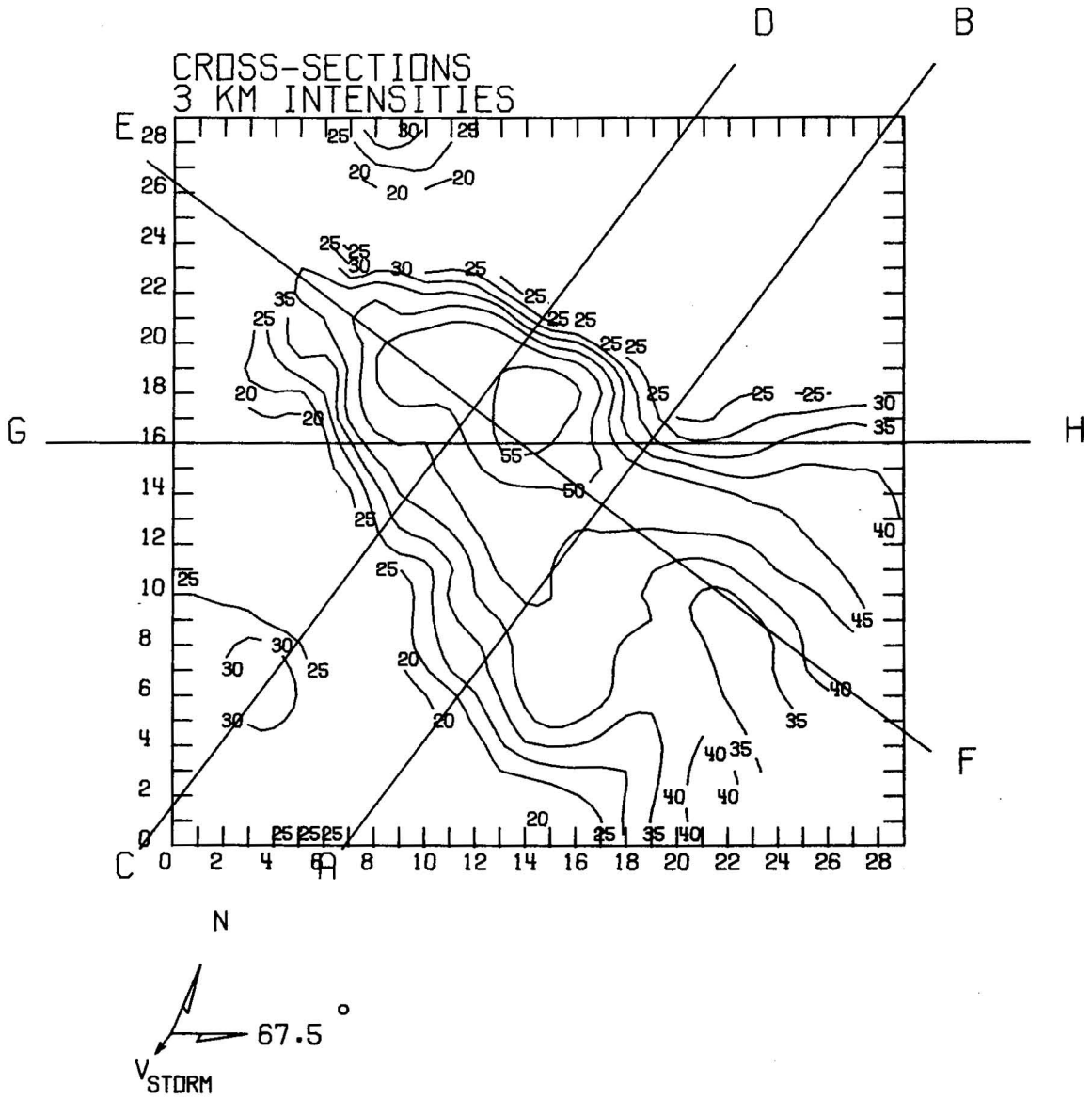

a

Figure 42a-e. Same as in Fig. 40, but at 1743.

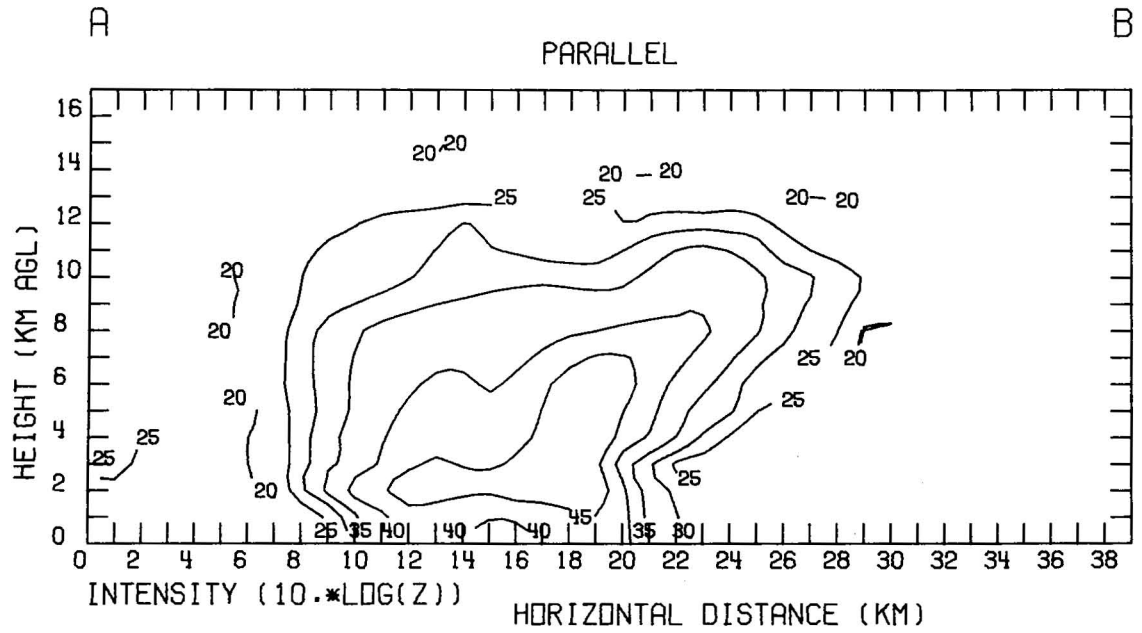
A
B
PARALLEL
HEIGHT (KM AGL)
INTENSITY (10.*LOG(Z))
HORIZONTAL DISTANCE (KM)

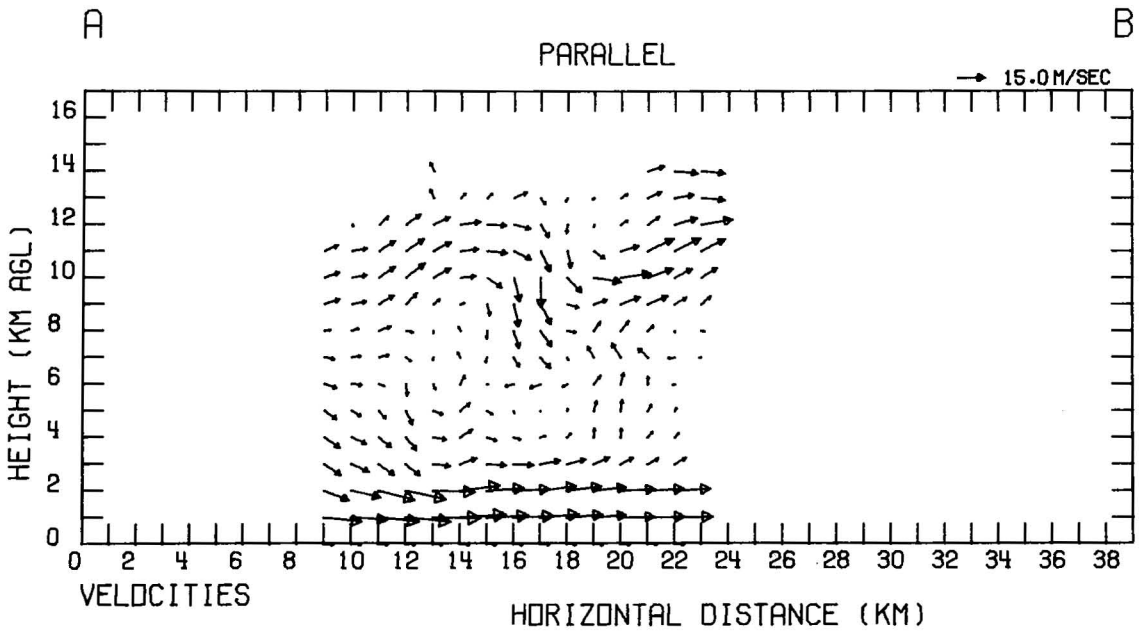
A
B
PARALLEL
15.0 M/SEC
HEIGHT (KM AGL)
VELOCITIES
HORIZONTAL DISTANCE (KM)

b

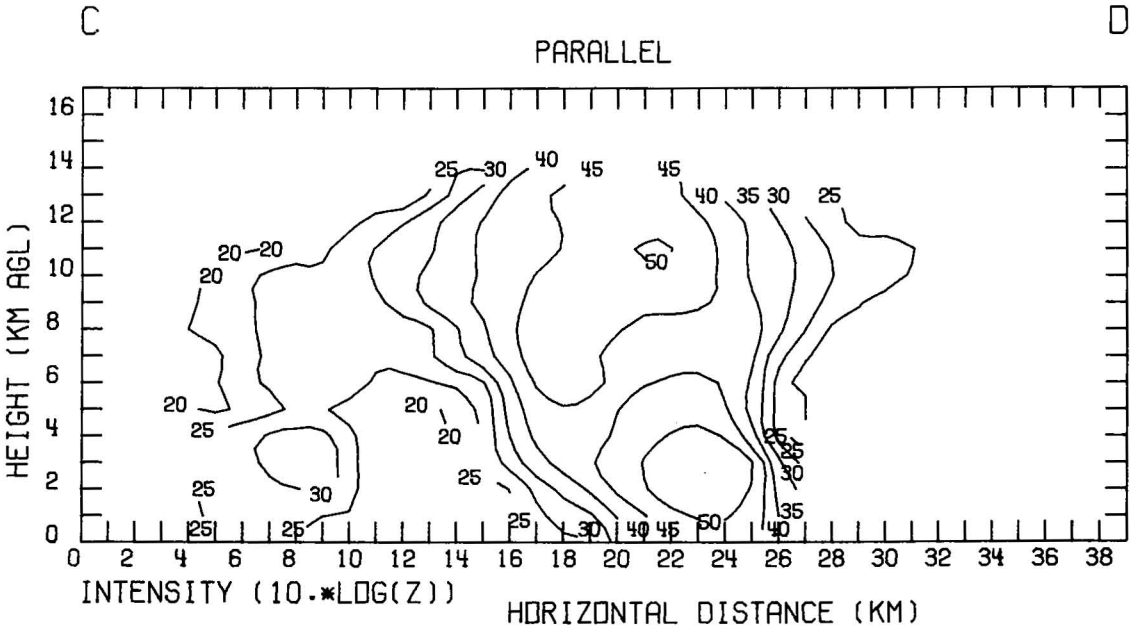
C
D
PARALLEL
HEIGHT (KM AGL)
INTENSITY (10.*LOG(Z))
HORIZONTAL DISTANCE (KM)

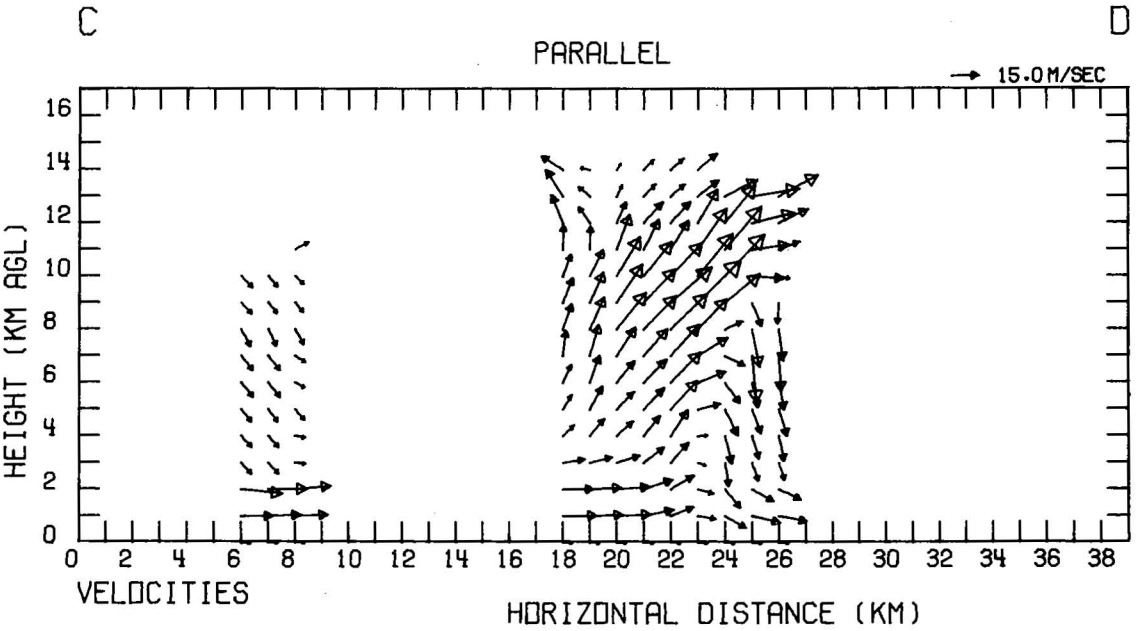
C
D
PARALLEL
15.0 M/SEC
HEIGHT (KM AGL)
VELOCITIES
HORIZONTAL DISTANCE (KM)

c

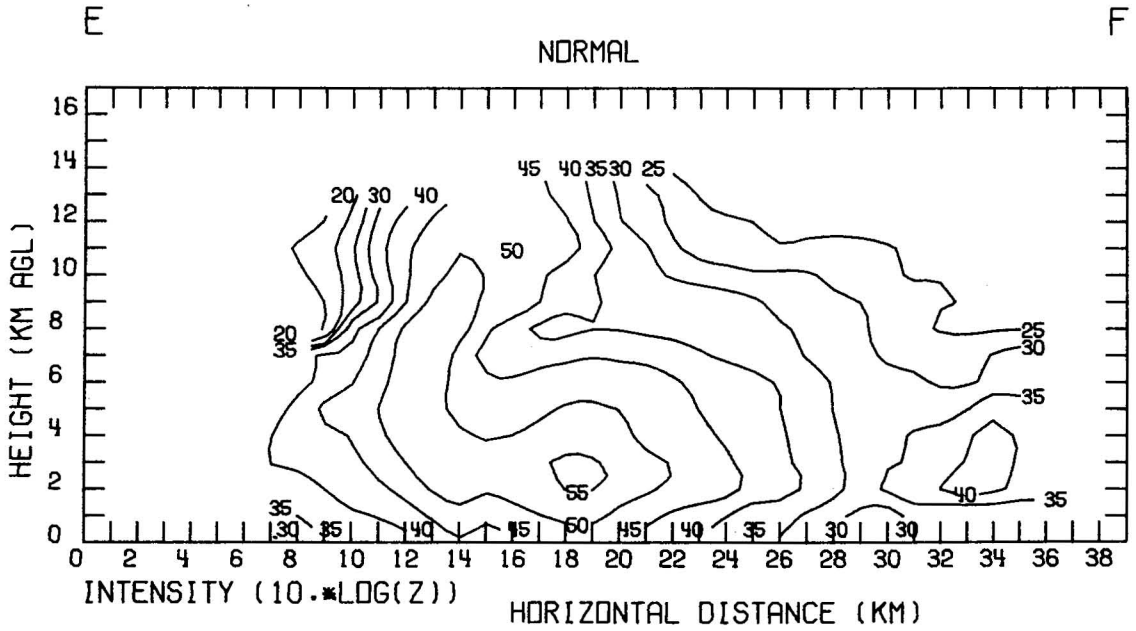
E
F
NORMAL
HEIGHT (KM AGL)
INTENSITY (10.*LOG(Z))
HORIZONTAL DISTANCE (KM)

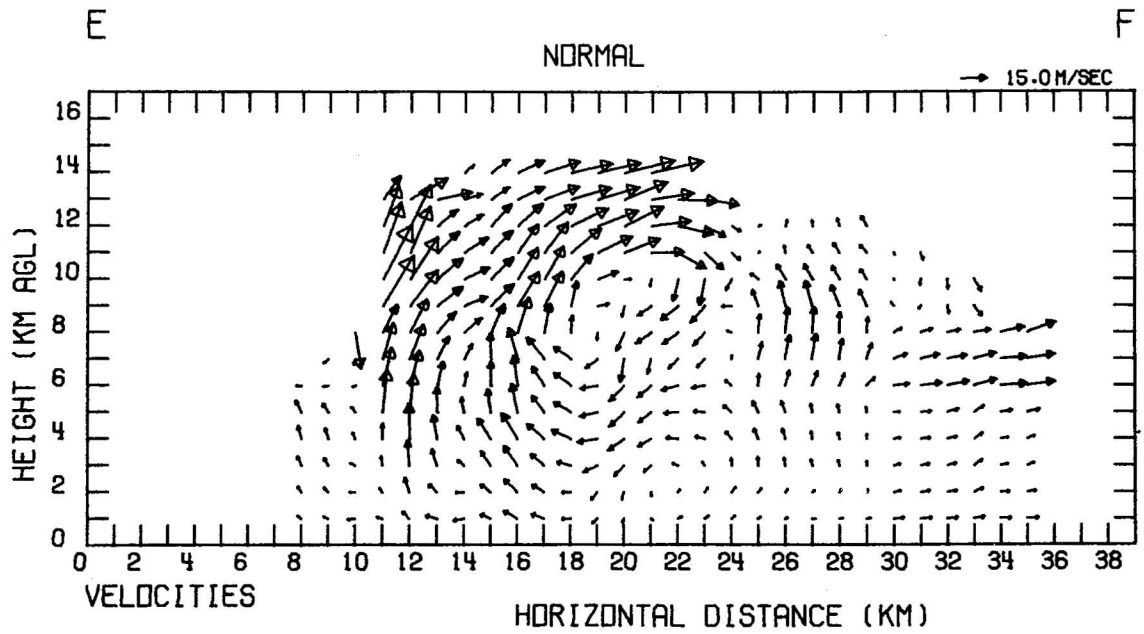
E
F
NORMAL
15.0 M/SEC
HEIGHT (KM AGL)
VELOCITIES
HORIZONTAL DISTANCE (KM)

d

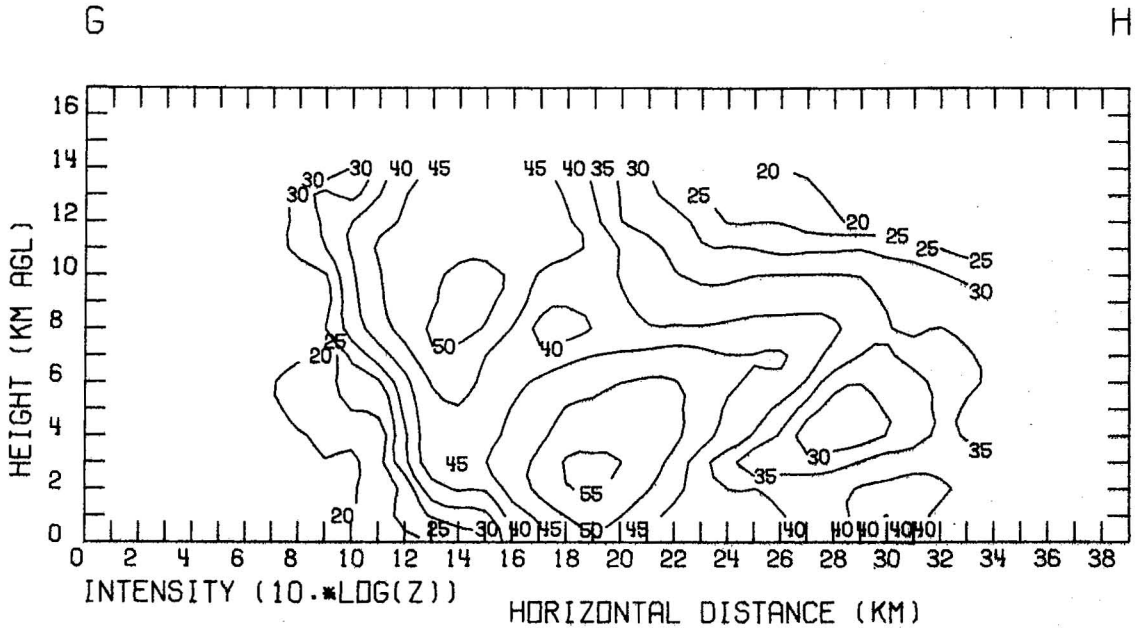
G
H
HEIGHT (KM AGL)
INTENSITY (10.*LOG(Z))
HORIZONTAL DISTANCE (KM)

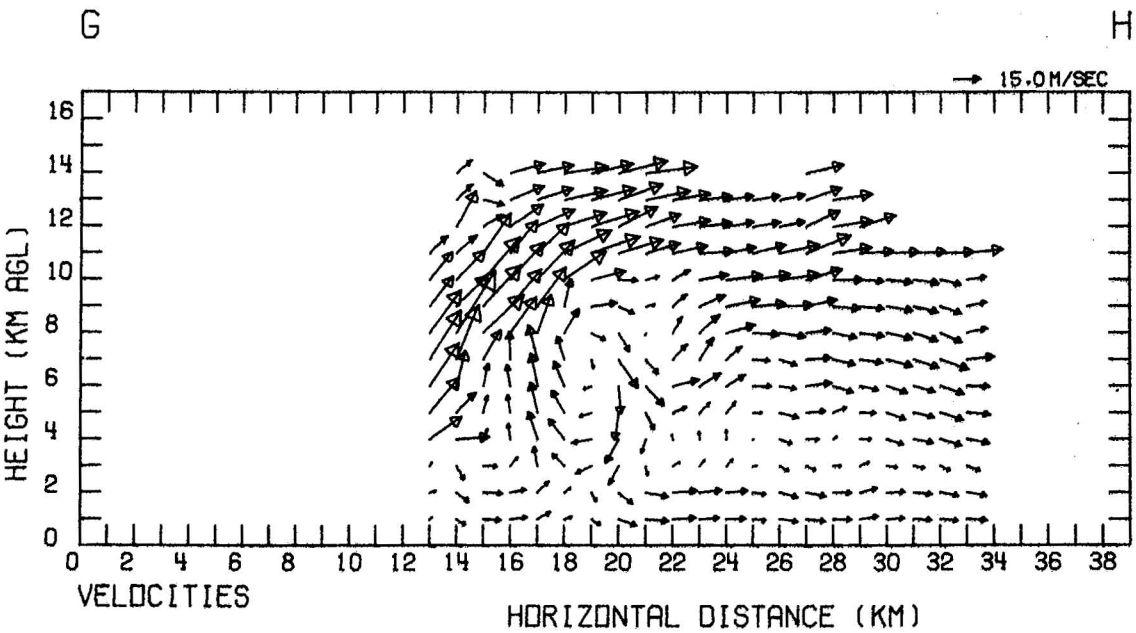
G
H
15.0M/SEC
HEIGHT (KM AGL)
VELOCITIES
HORIZONTAL DISTANCE (KM)

e

maximum of 30 m s^{-1} at 10 km. An intense downdraft with a maximum of -36 m s^{-1} at 7.0 km contains the pronounced north flank reflectivity gradient. The E-F and G-H cross-sections (Figs. 42d,e) show that the collapsing Cell I is dominated by downdrafts, while Cell II contains strong updrafts. The sloping downdraft in Fig. 42d is downflow in the wake seen from the south, and attains a maximum of -15 m s^{-1} at 10 km. A secondary maximum of -13 m s^{-1} occurs at 7.0 km. A portion of the air in the wake return flow may originate within the flanking jet regions. Water loading and evaporative cooling could maintain its descent as it flows back to the west. This air runs into the west flank updraft at low and mid-levels. Low-level convergence is therefore enhanced, but at the expense of a dilution of updraft buoyancy resulting from entrainment of a portion of the cool downdraft air. The updraft tilts downshear over the downdraft, and a large rotor forms in storm mid-levels as a result of this shearing. The horizontal vorticity of the rotor, approximately 1.6 x 10^{-2} s^{-1}, is appreciable. The maximum updrafts are well correlated with reflectivity maxima aloft. The strongest updraft in the storm at 1743 is 33 m s^{-1} at 8.0 km on the storm's west flank.

Analyses of the tilt sequences at 1800 and 1816 (Figs. 43-46) indicate that storm structure was fairly persistent through that period. The strongest convection remains near the storm's west flank. Peak updrafts range from 39 m s^{-1} to 44 m s^{-1} between 8.0 km and 12.0 km. Maximum reflectivities aloft range from 48 dBZ to 56 dBZ between 6.0 km and 9.0 km. Strongest downdrafts are downshear of the updraft plume, attaining values between -13 m s^{-1} and -22 m s^{-1} from 4.0 km to 7.0 km. Low-level horizontal wind flow is southerly. Divergent outflow is present at 13 km. The mid-level flanking jets are again evident, but the wake return flow vanishes by 1800. This feature reforms by 1816.

Figures 47 and 48 present the storm structure at 1832. A pronounced reflectivity gradient on the southwest and west flanks in low levels, is evident in Figs. 47a,b. Horizontal winds are uniform and southerly through 3 km. Westerly winds flanking the area of high reflectivity at 7 km, merge smoothly on its downshear side. The wake return flow feature has vanished, with weak eddy-like motions remaining on the downshear flank of the reflectivity core. Southerly flow within the core at mid-levels averages roughly 10 m s^{-1}, half the value attained nearly one hour earlier in the same region. At 10 km (Fig. 47d) westerly winds and weak diffluence are apparent. The vertical storm structure as illustrated by a west-east cross-section in Fig. 48c, has weakened considerably. A reflectivity maximum of 54 dBZ at 5 km and a vertical velocity maximum of 16 m s^{-1} at 6 km, are located near the storm west flank. This convective cell does not extend to the radar-visible cloud top. A small cell 5 km to the NE has a maximum vertical velocity of 18 m s^{-1} at 9 km, but overlies a weak downdraft between the surface and 3 km. The top of the storm-scale radar echo lies immediately beneath the tropopause at 13 km. Figure 48b shows that the north flank reflectivity gradient has weakened considerably and that cross-gradient airflow is essentially horizontal.

3.3.5 Some Aspects of Storm Structure, Dynamics, and Microphysics

The near-storm environment and the storm's internal structure exhibit some striking characteristics of great interest. The anomalous motion of the

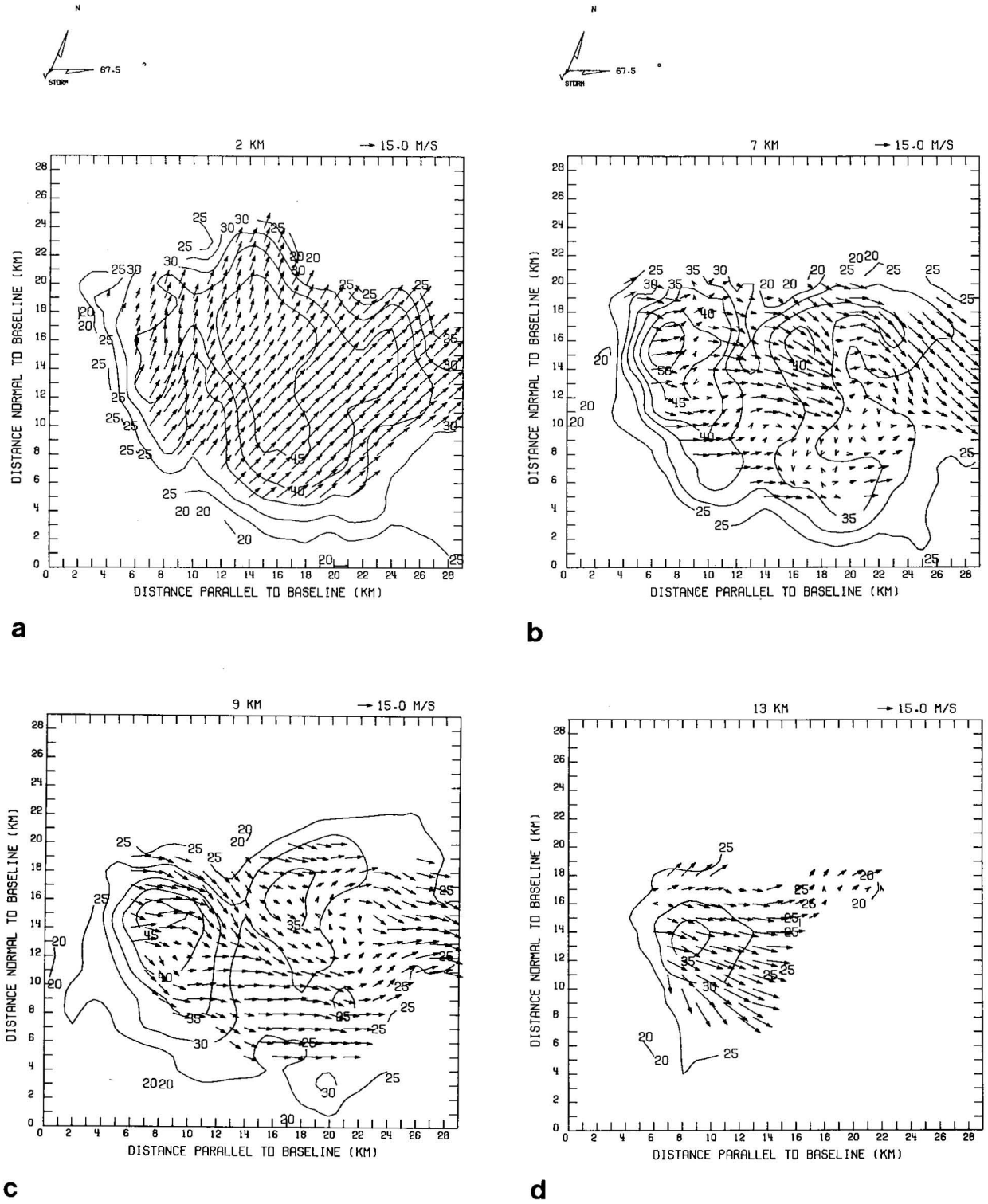

Figure 43. Same as in Fig. 39, but at 1800.

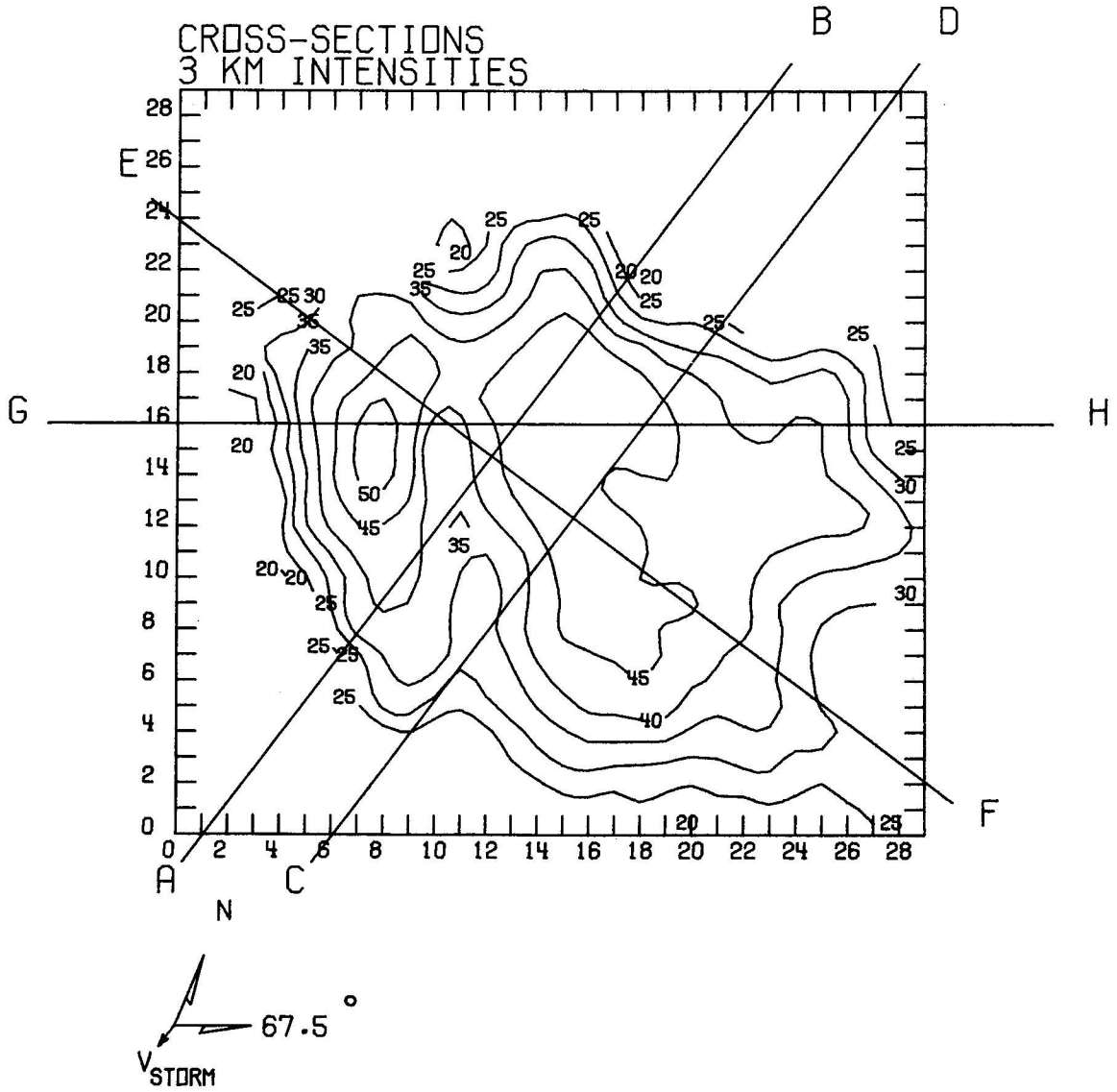

a

Figure 44a-e. Same as in Fig. 40, but at 1800.

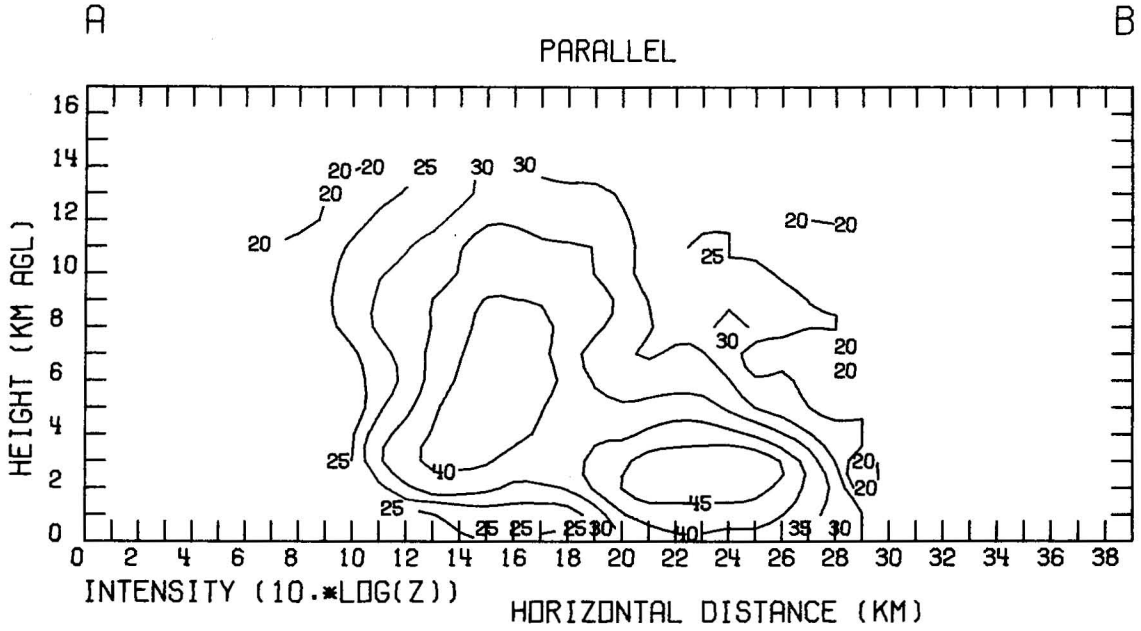
A
B
PARALLEL
HEIGHT (KM AGL)
INTENSITY (10.*LOG(Z))
HORIZONTAL DISTANCE (KM)

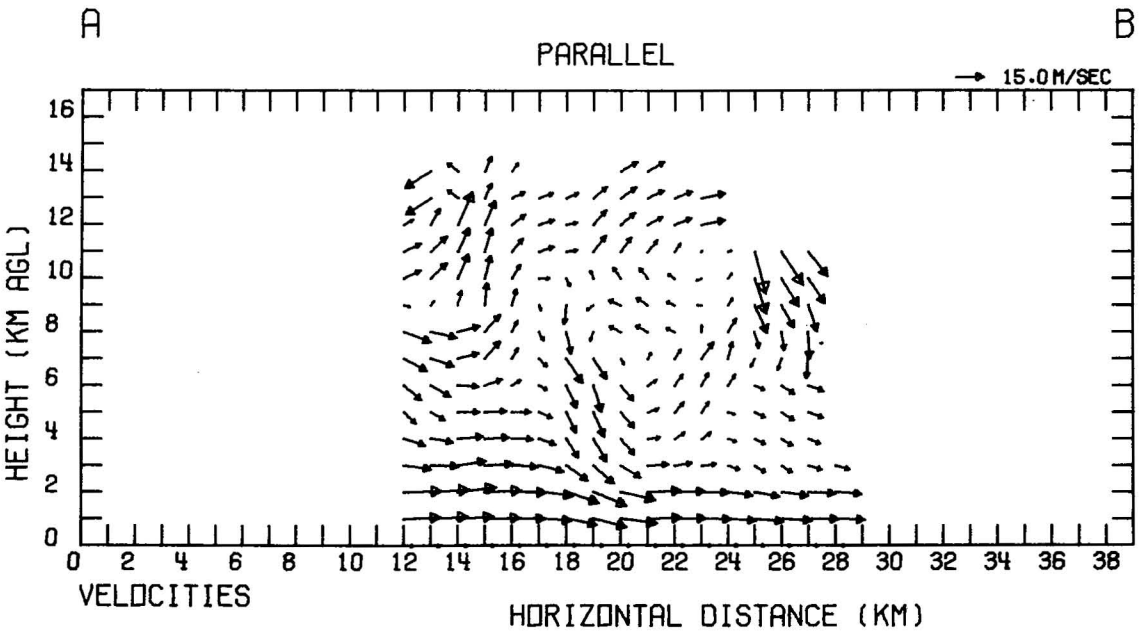
A
B
PARALLEL
15.0M/SEC
HEIGHT (KM AGL)
VELOCITIES
HORIZONTAL DISTANCE (KM)

b

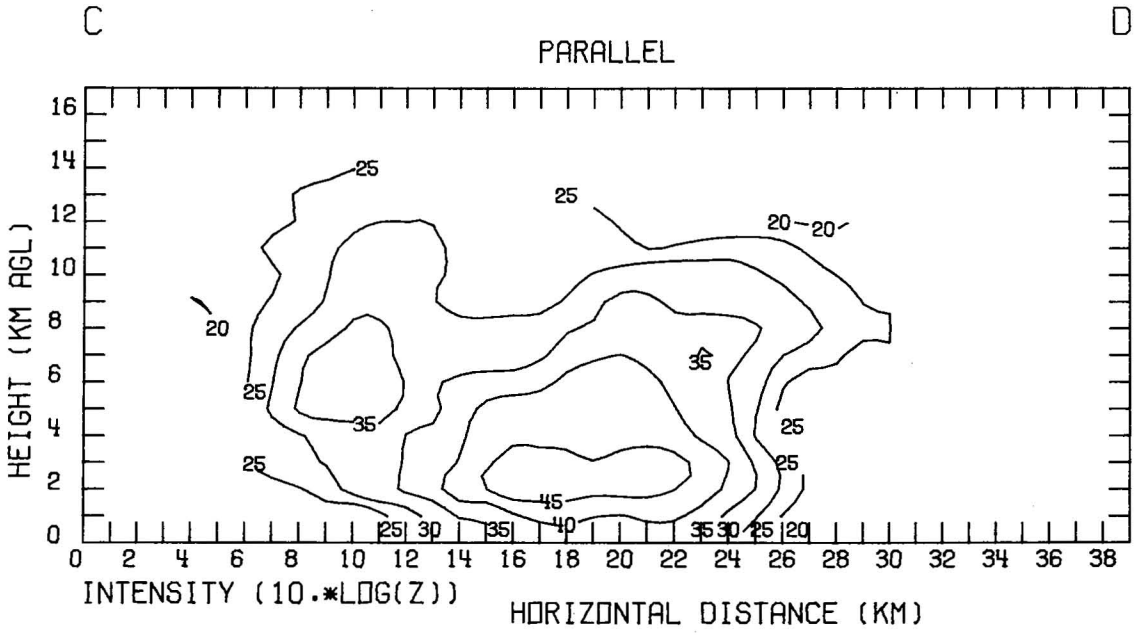
C
D
PARALLEL
HEIGHT (KM AGL)
INTENSITY (10.*LOG(Z))
HORIZONTAL DISTANCE (KM)

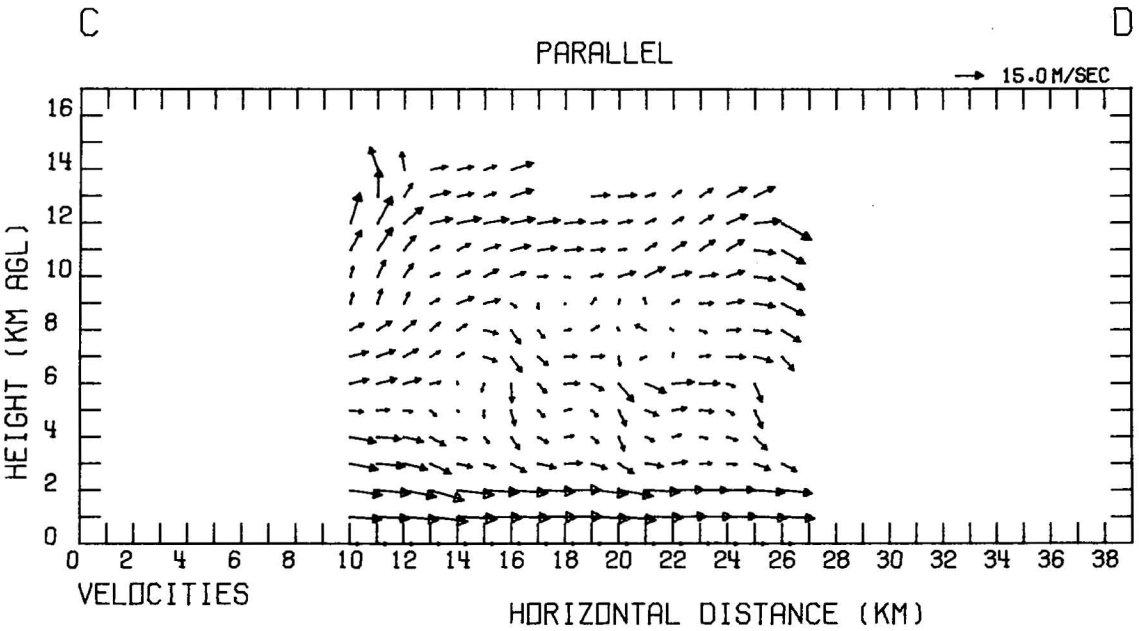
C
D
PARALLEL
15.0 M/SEC
HEIGHT (KM AGL)
VELOCITIES
HORIZONTAL DISTANCE (KM)

c

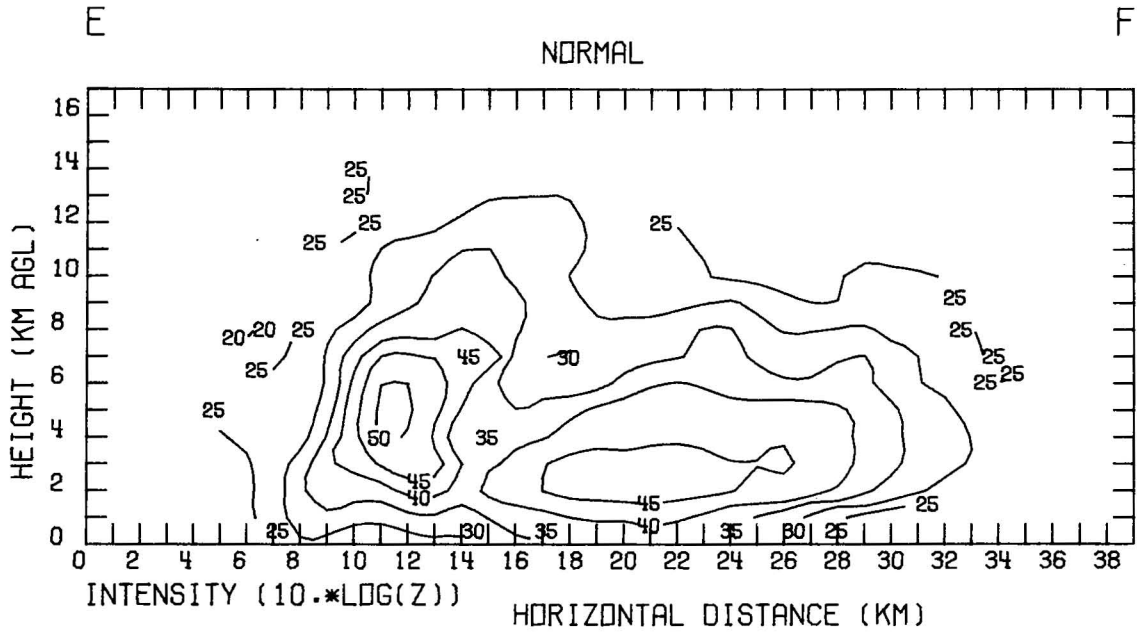
E
F
NORMAL
HEIGHT (KM AGL)
INTENSITY (10.*LOG(Z))
HORIZONTAL DISTANCE (KM)

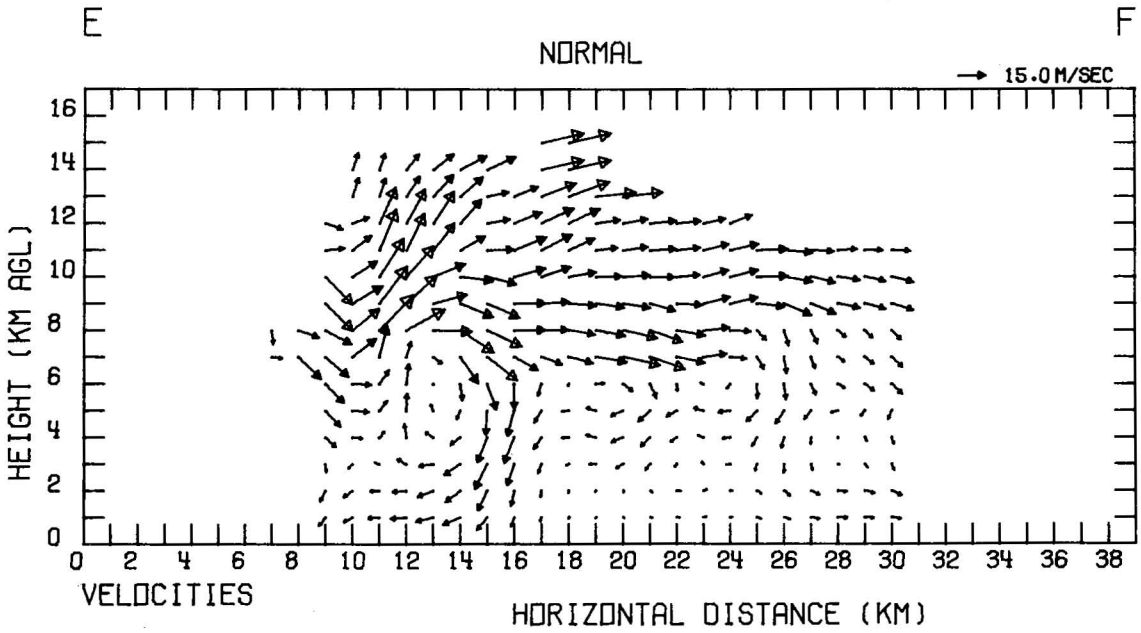
E
F
NORMAL
15.0 M/SEC
HEIGHT (KM AGL)
VELOCITIES
HORIZONTAL DISTANCE (KM)

d

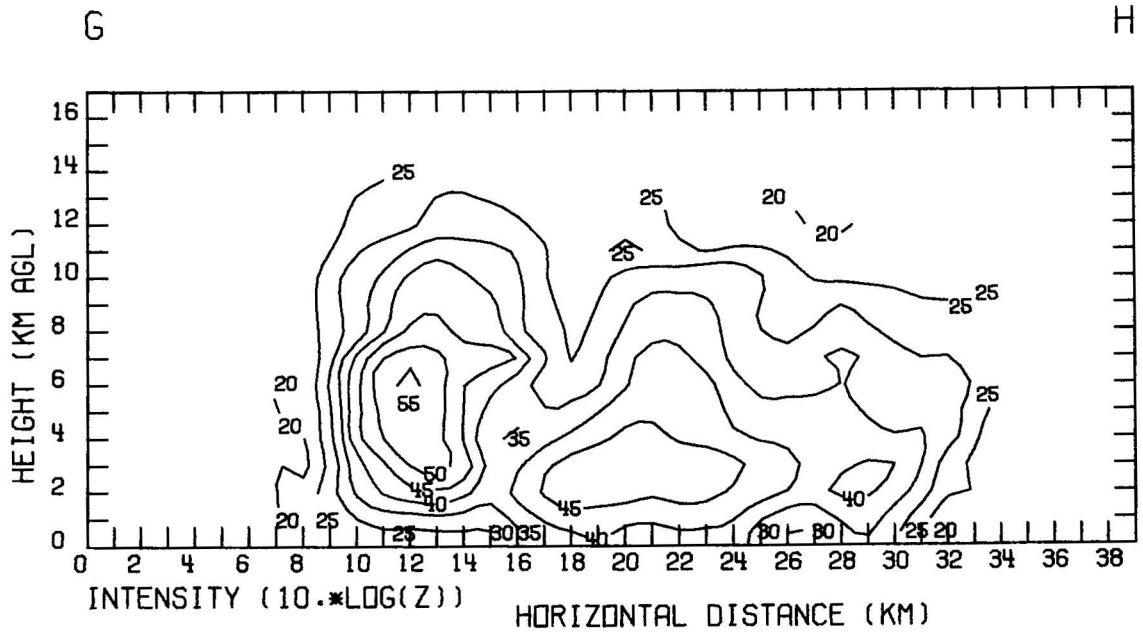
G
H
HEIGHT (KM AGL)
INTENSITY (10.*LOG(Z))
HORIZONTAL DISTANCE (KM)

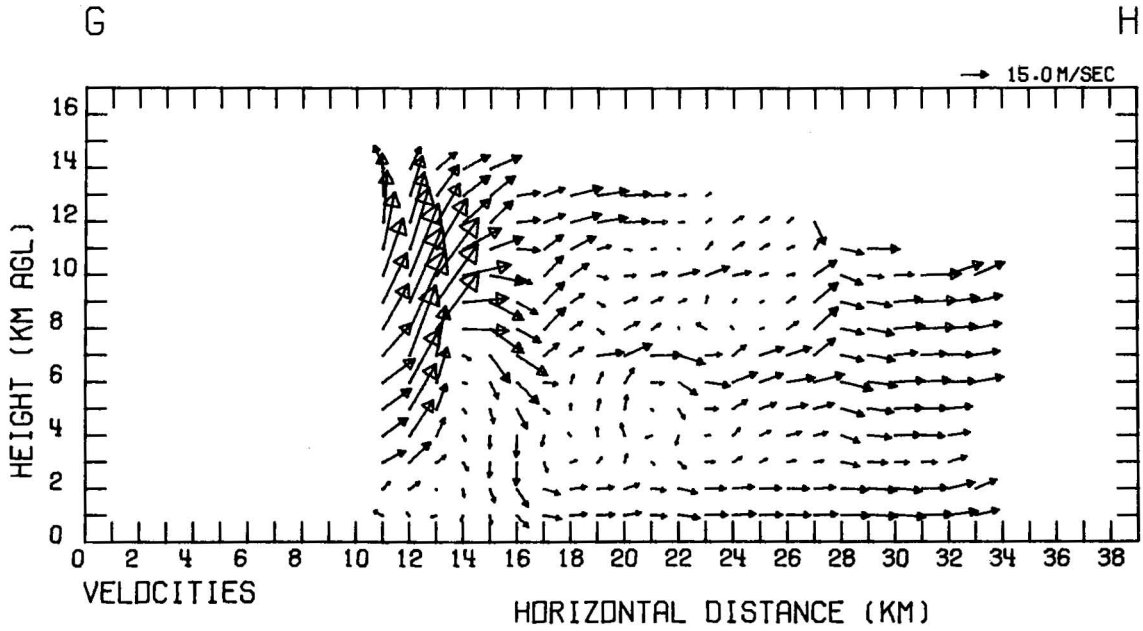
G
H
15.0 M/SEC
HEIGHT (KM AGL)
VELOCITIES
HORIZONTAL DISTANCE (KM)

e

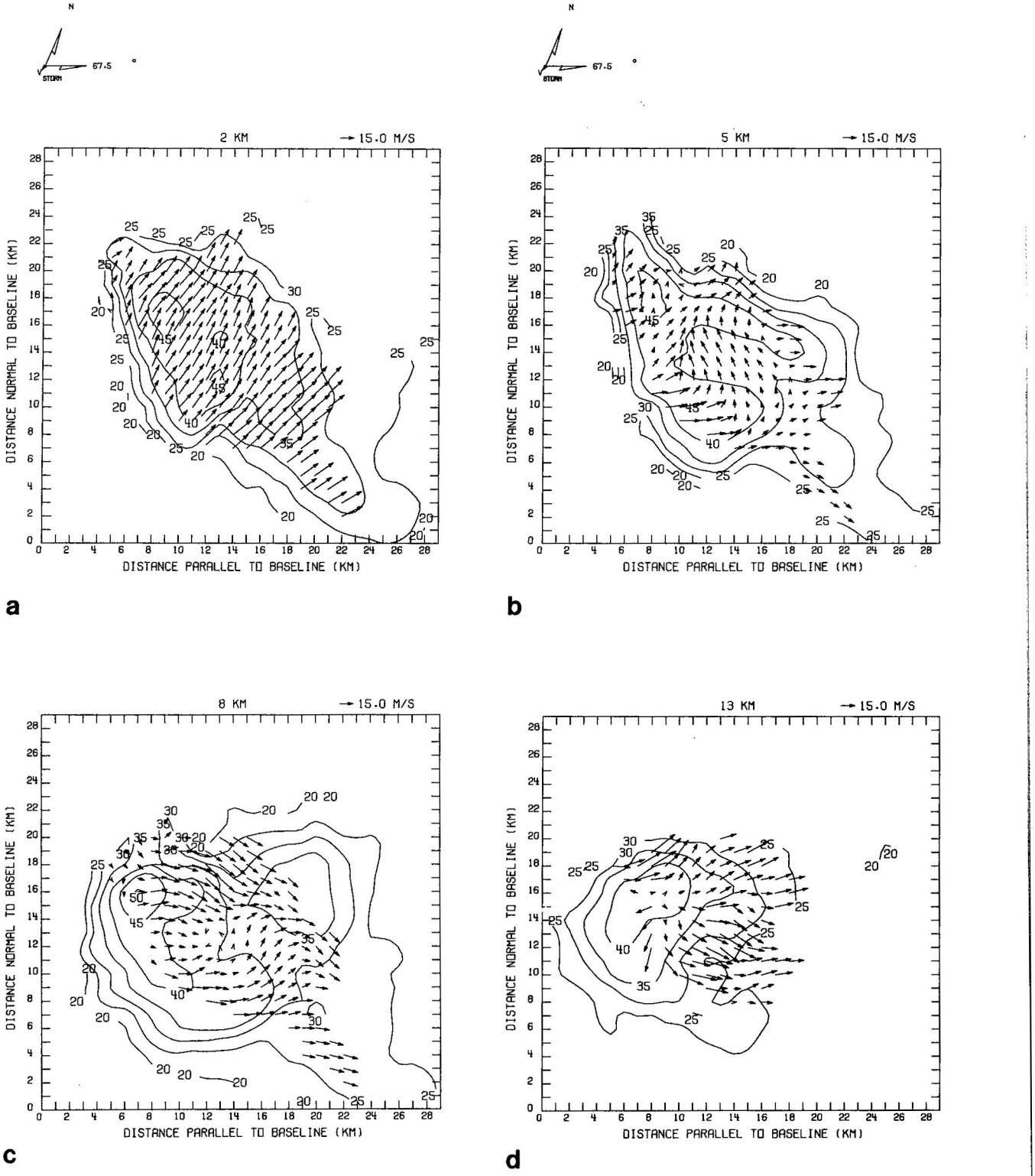

Figure 45. Same as in Fig. 39, but at 1816.

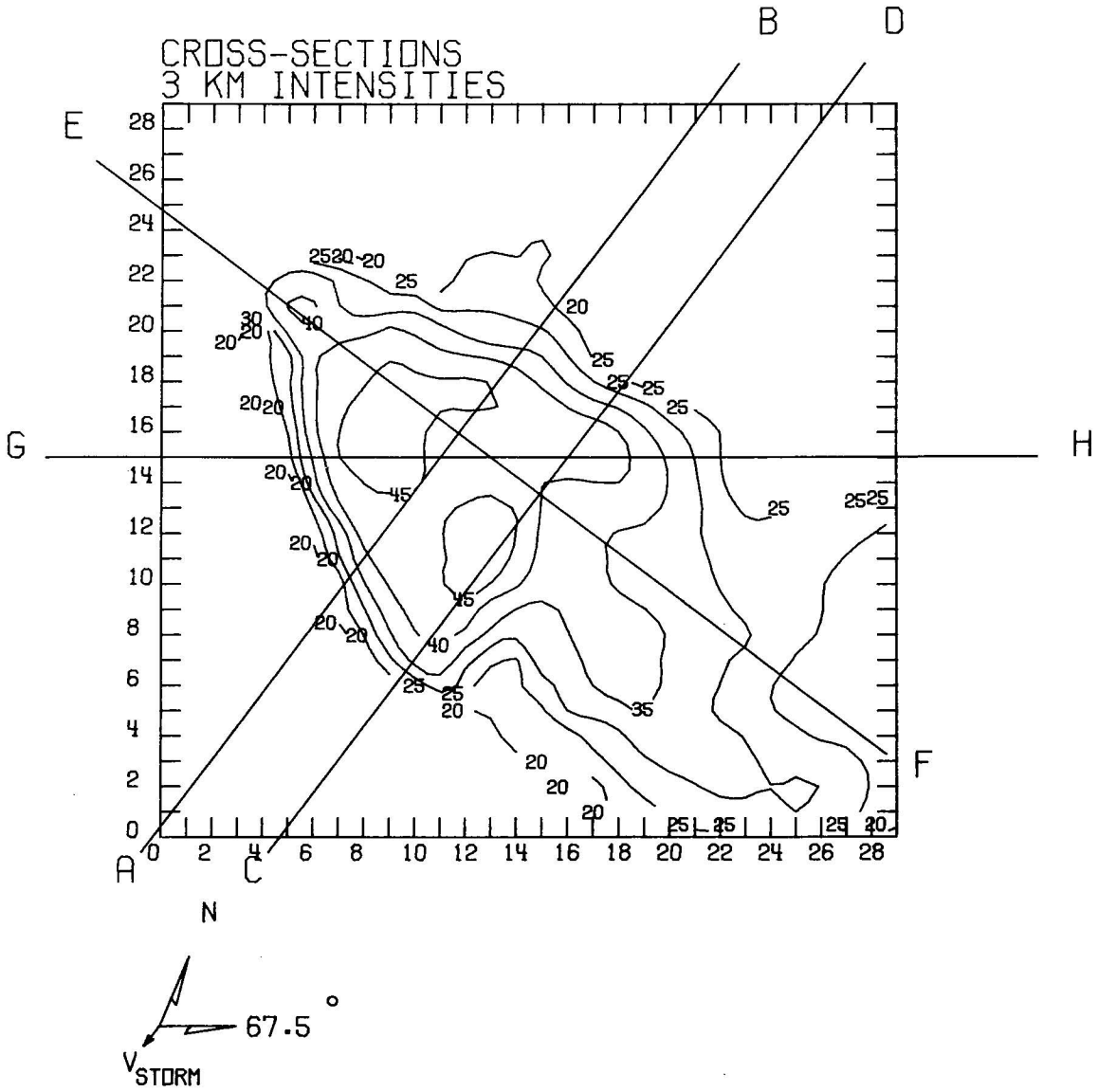

a

Figure 46a-e. Same as in Fig. 40, but at 1816.

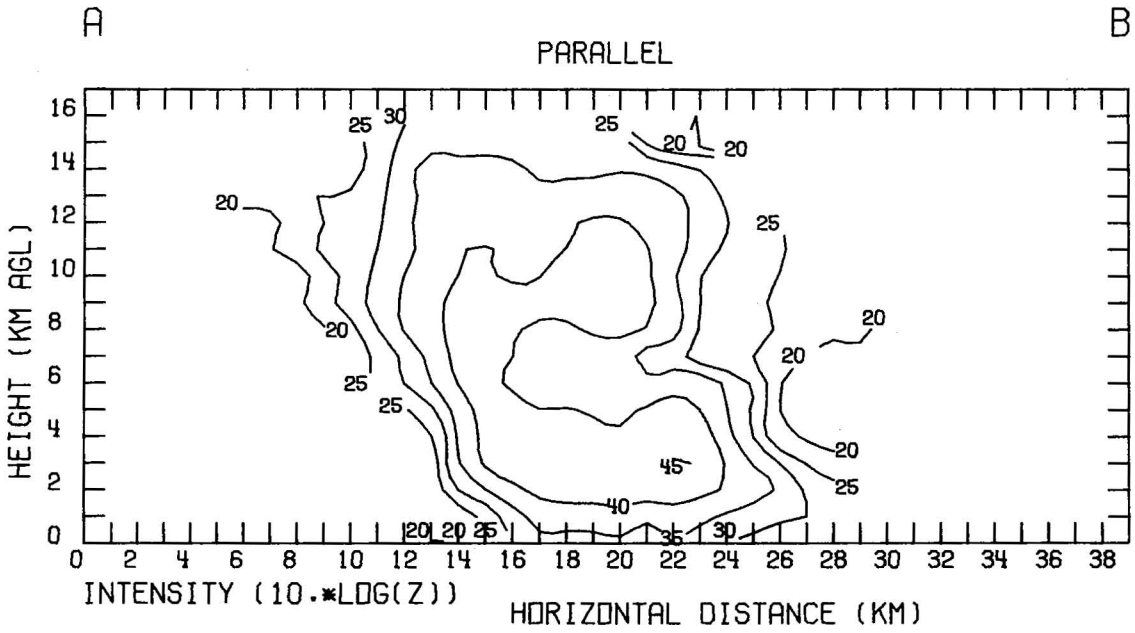
A
B
PARALLEL
HEIGHT (KM AGL)
INTENSITY (10.*LOG(Z))
HORIZONTAL DISTANCE (KM)

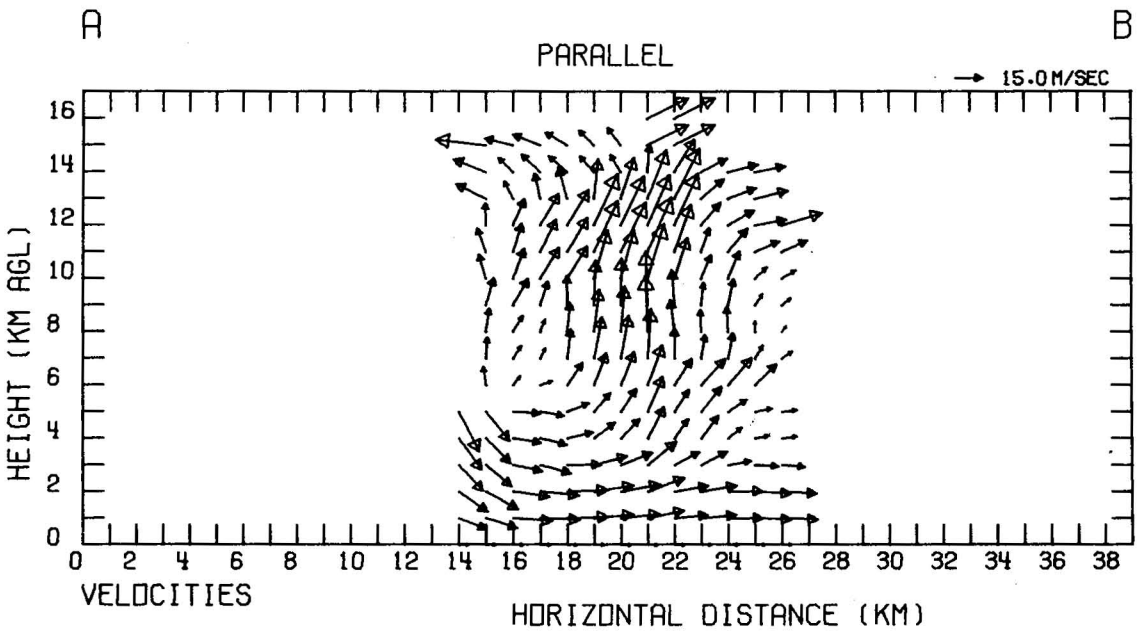
A
B
PARALLEL
15.0M/SEC
HEIGHT (KM AGL)
VELOCITIES
HORIZONTAL DISTANCE (KM)

b

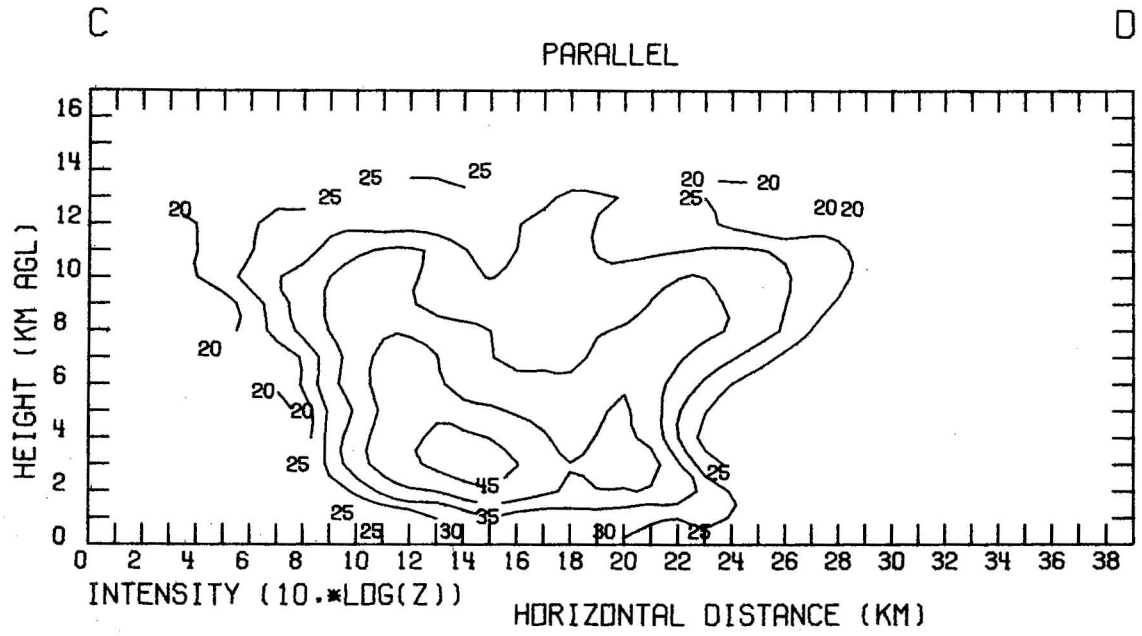
C
D
PARALLEL
HEIGHT (KM AGL)
INTENSITY (10.*LOG(Z))
HORIZONTAL DISTANCE (KM)

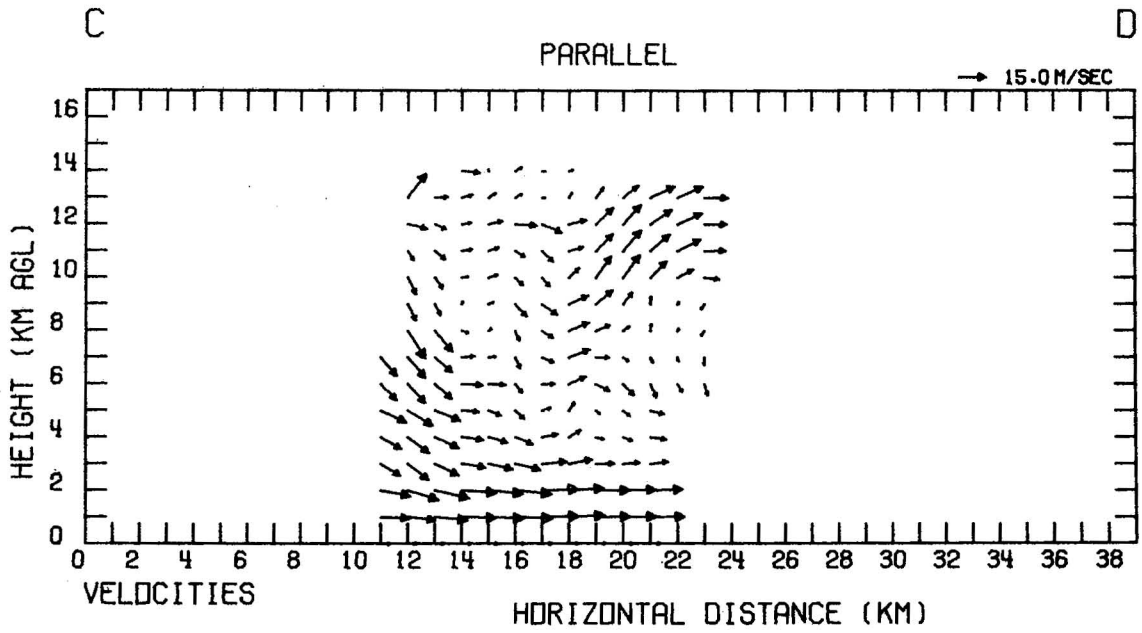
C
D
PARALLEL
15.0 M/SEC
HEIGHT (KM AGL)
VELOCITIES
HORIZONTAL DISTANCE (KM)

C

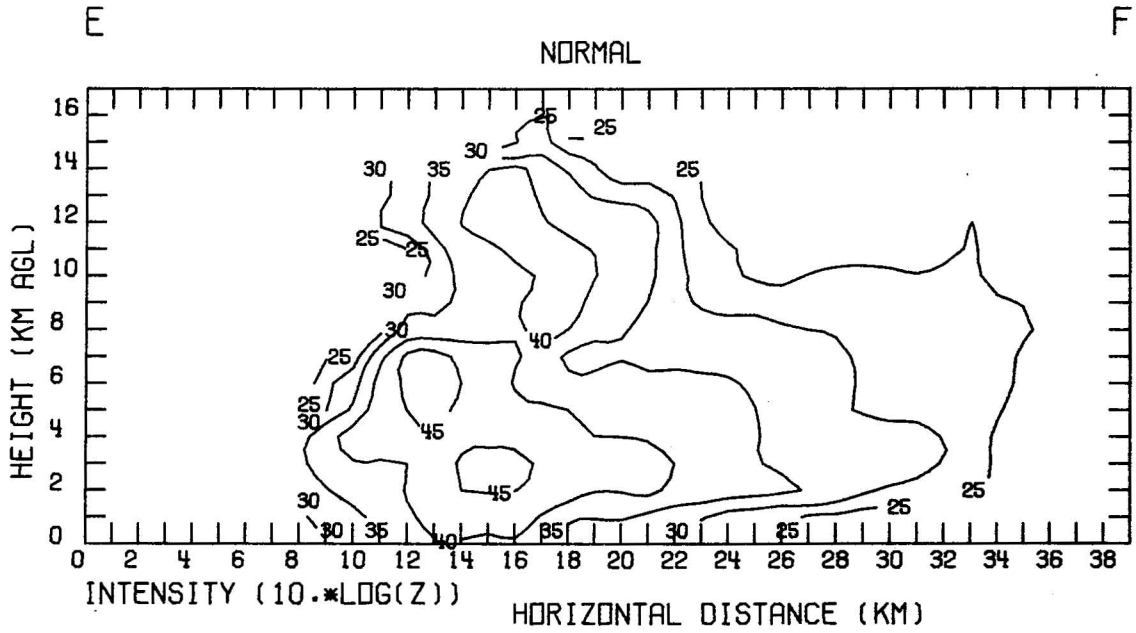
E
F
NORMAL
HEIGHT (KM AGL)
INTENSITY (10.*LOG(Z))
HORIZONTAL DISTANCE (KM)

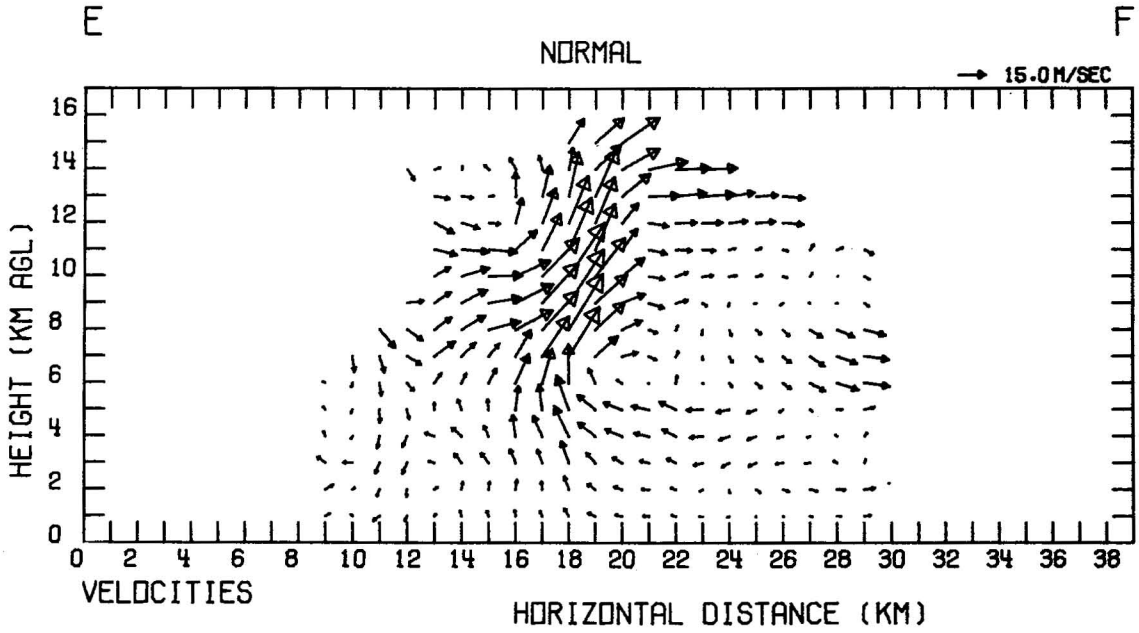
E
F
NORMAL
15.0 M/SEC
HEIGHT (KM AGL)
VELOCITIES
HORIZONTAL DISTANCE (KM)

d

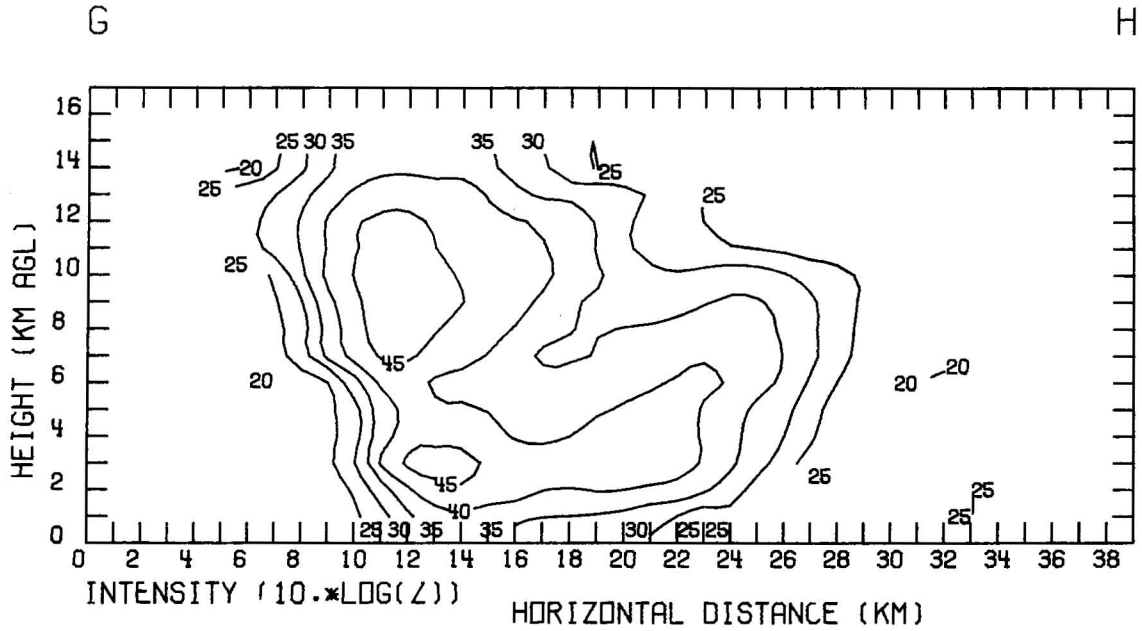
G
H
HEIGHT (KM AGL)
INTENSITY (10.*LOG(Z))
HORIZONTAL DISTANCE (KM)

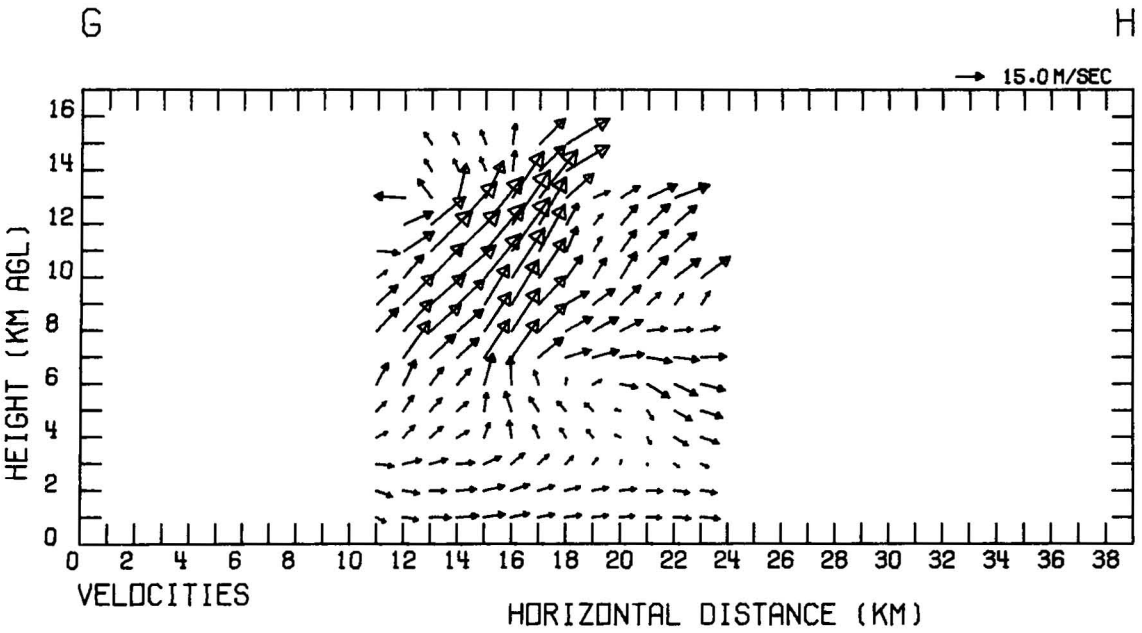
G
H
15.0 M/SEC
HEIGHT (KM AGL)
VELOCITIES
HORIZONTAL DISTANCE (KM)

e

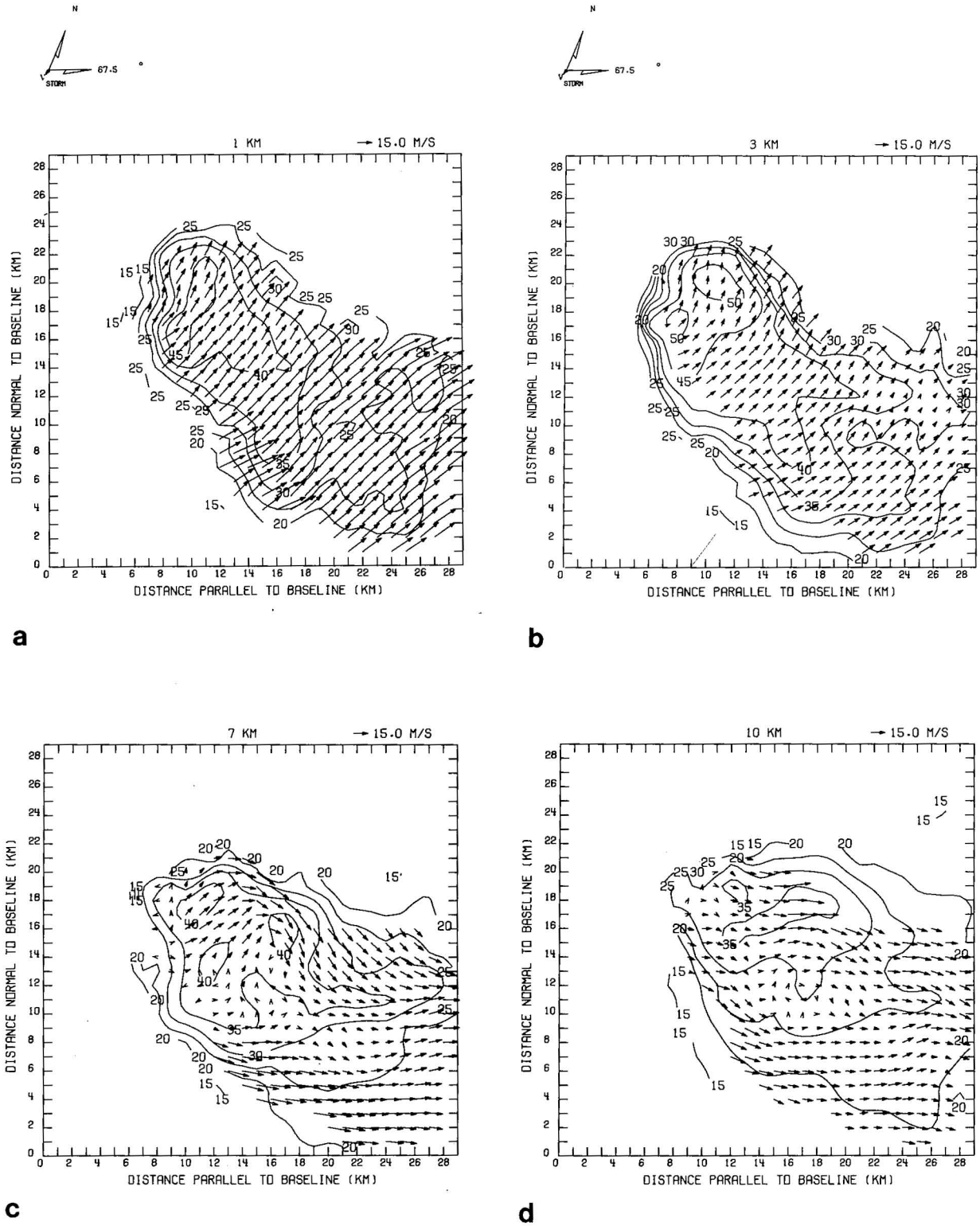

Figure 47. Same as in Fig. 39, but at 1832.

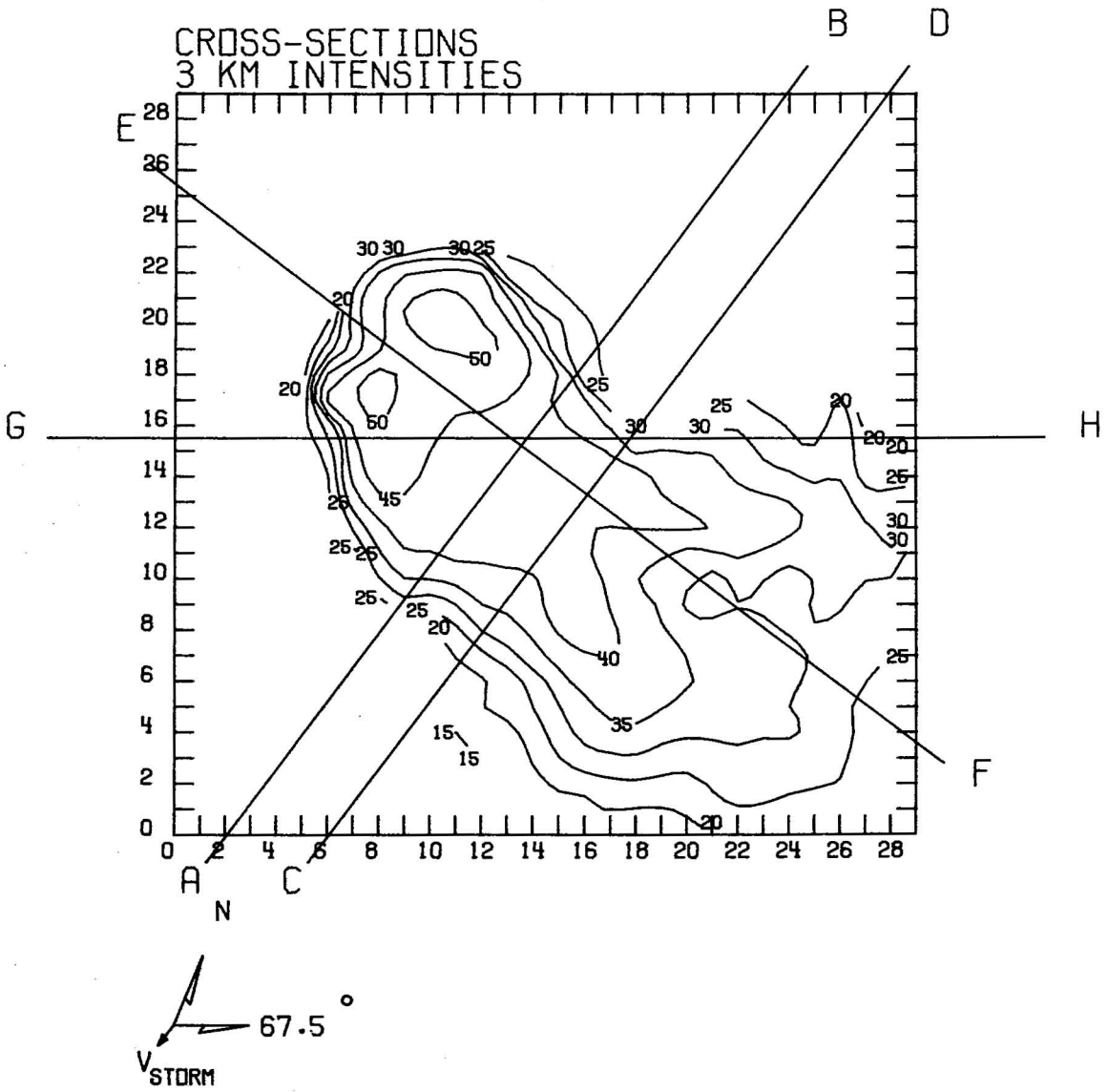

a

Figure 48a-c. Same as in Fig. 40, but at 1832.

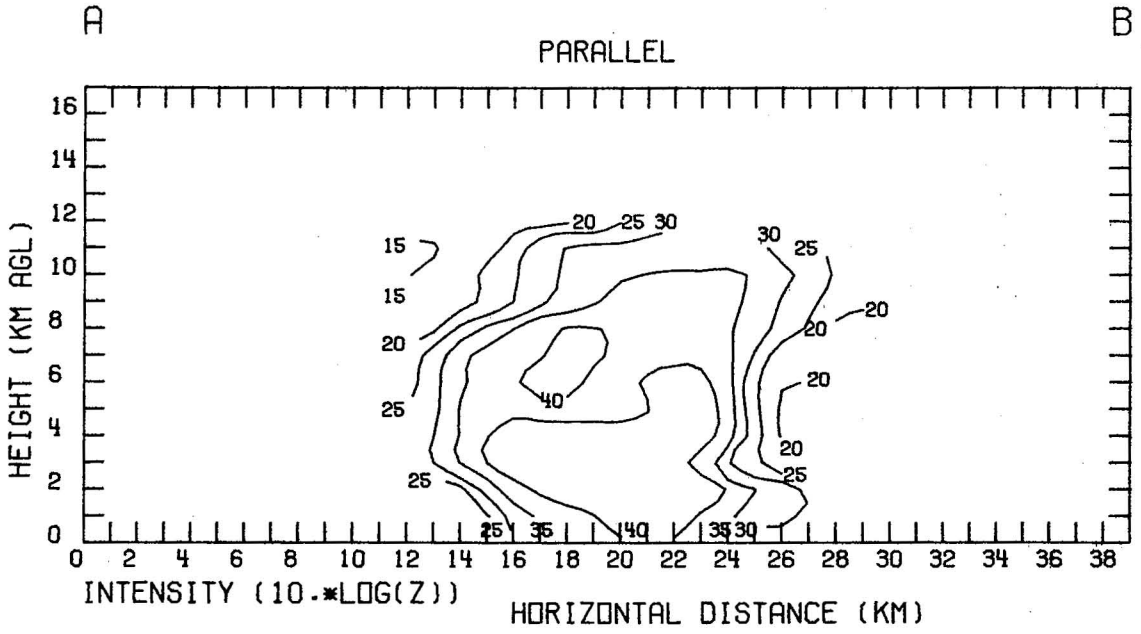
A
B
PARALLEL
HEIGHT (KM AGL)
INTENSITY (10.*LOG(Z))
HORIZONTAL DISTANCE (KM)

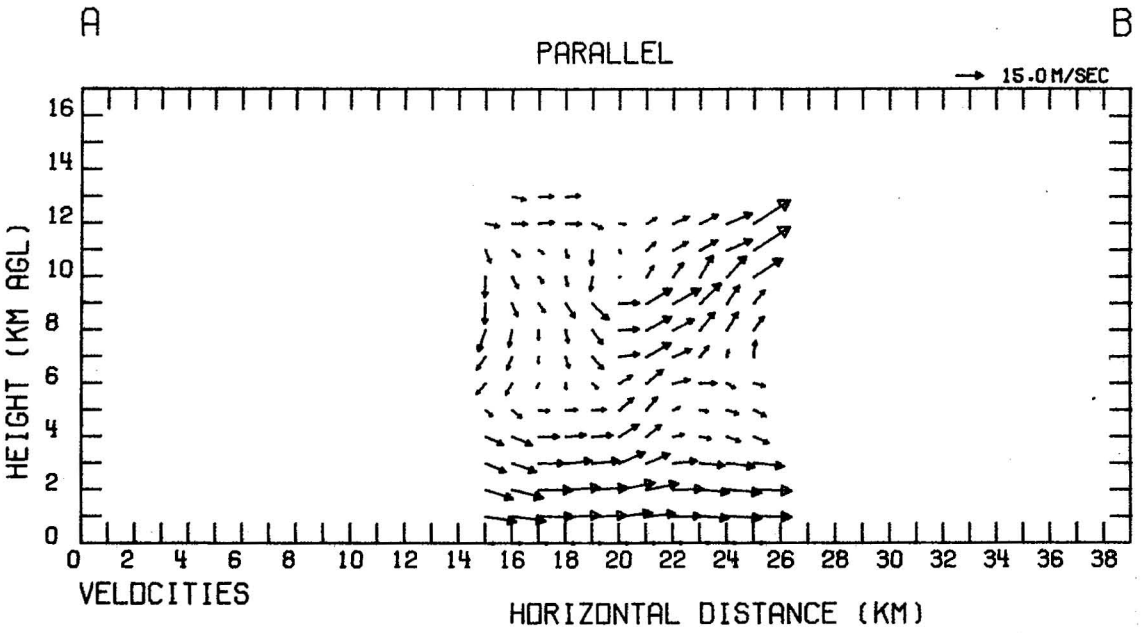
A
B
PARALLEL
15.0 M/SEC
HEIGHT (KM AGL)
VELOCITIES
HORIZONTAL DISTANCE (KM)

b

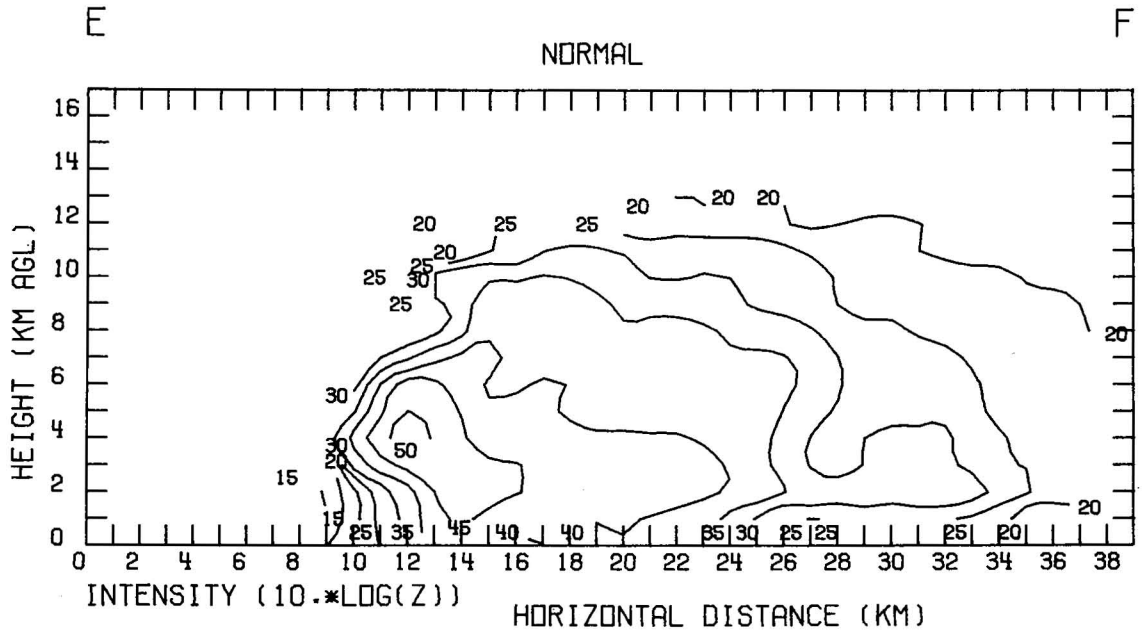
E
F
NORMAL
HEIGHT (KM AGL)
INTENSITY (10.*LOG(Z))
HORIZONTAL DISTANCE (KM)

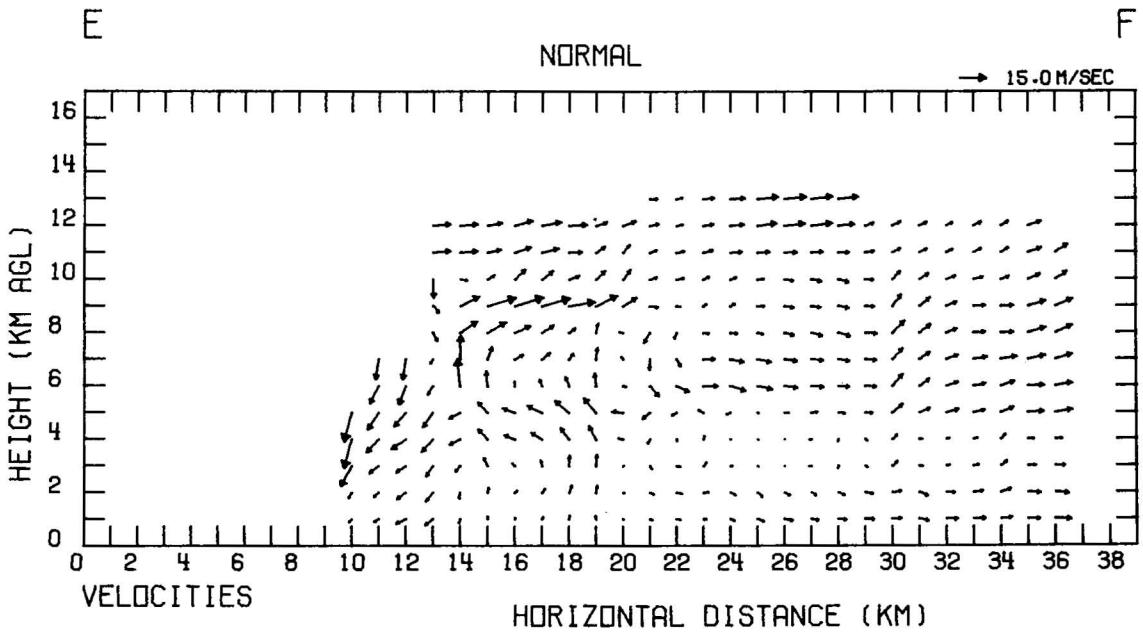
E
F
NORMAL
15.0 M/SEC
HEIGHT (KM AGL)
VELOCITIES
HORIZONTAL DISTANCE (KM)

C

radar echo 90° to the right of the mean wind of the cloud-bearing layer has been noted. Doppler and visual observations both indicate that strong updrafts persistently developed on the storm's southwest and west flanks. From the EMC 1641 sounding, we know that the near-environment west of the storm was marked by strong convective instability. Severe storms in eastern Oklahoma earlier in the afternoon moved southeast, nearly along the mean wind vector. These storms formed an east-west line, which indicates that their favored zone of convective development was along the south flank. The Wynnewood storm was observed to weaken considerably and to realign its motion to that of the upper winds near 1900 around sunset. Doppler observations at 1832 indicate that west flank convection was greatly weakened, reflecting the importance of surface heating on convective intensity and consequently the storm's propagation.

Reliable estimates of the vertical motion fields within convective storms are necessary in order to understand their evolutionary processes. Figure 49 depicts profiles of vertical velocity in the strongest updrafts and downdrafts at 1719 on 28 May. Adjusted profiles are solid while unadjusted profiles are dashed. Dotted curve represents strongest updraft predicted from parcel theory (no entrainment or water-loading) while curve of open circles represents the Dibble updraft balloon sounding discussed by Barnes (1970) and Davies-Jones (1974). The Dibble sounding, in which vertical velocity was deduced from the balloon rise rate excess, reflects conditions in a strong updraft which is undiluted at least through storm mid-levels. The Dibble storm's isolation and thermodynamic properties of environment and updraft indicate its similarity to the Wynnewood storm. Near the tropopause, the unadjusted updraft is 20-30 m s^{-1} larger than the parcel theory updraft, while the adjusted updraft is smaller than parcel theory. Above the tropopause, $\frac{\partial w}{\partial z} > 0$ for the unadjusted updraft while parcel theory predicts that $\frac{\partial w}{\partial z} < 0$. Note also that $\frac{\partial w}{\partial z} < 0$ for the adjusted updraft. The results of Wilhelmson's (1974) numerical simulation of deep convection indicated that the vertical gradient of the pressure perturbation consistently opposed thermal buoyancy in cloud upper levels. Consequently, updrafts were reduced in this region, and the updraft maximum was lowered toward cloud mid-levels. Consideration of the model diagnostic pressure equation (see also Wilhelmson and Ogura, 1972), indicates that this effect may be significantly enhanced if the convection is capped by a temperature inversion such as the tropopause. The storm echo top, near 16 km at 1719, is well below the altitude of maximum stratospheric penetration predicted by parcel theory. Since mean hydrometeor fall speed is rather small near echo top, the visible cloud top is probably not in excess of 1 km above the echo top at any given time. We may conclude that on the average, maximum updrafts are probably not as strong as indicated by parcel theory. The observation of pulsating towers which rise nearly to heights predicted by parcel theory offers an exception, but the time and space dimensions of these oscillations are below the minimum definable by the objective analysis. Excessive water and heat fluxes through the quasi-stationary echo top implied by unadjusted vertical motion fields are unrealistic. The variational analysis appears to produce improved, physically consistent vertical wind fields, as opposed to the conventional approach which often gives physically unrealizeable results.

The importance of the pressure perturbation on the updraft configuration in storm low levels may be established by considering measured updrafts in

relation to dynamics of convection. Consider again Fig. 33, discussed earlier in the case study. Dotted lines represent temperature and dew point profiles for a hypothetical parcel rising from below rain-free cloud base on the southwest flank of the Wynnewood storm near 1740. Input data was provided by sensors on board the NCAR Queen Air aircraft, which was flying near 650 m AGL at a pressure of 895 mb. The parcel LCL was near 1000 m AGL at a pressure of 858 mb and temperature of 19.2 C. If we can assume that the environmental sounding did not change considerably between 1641 and 1740 near

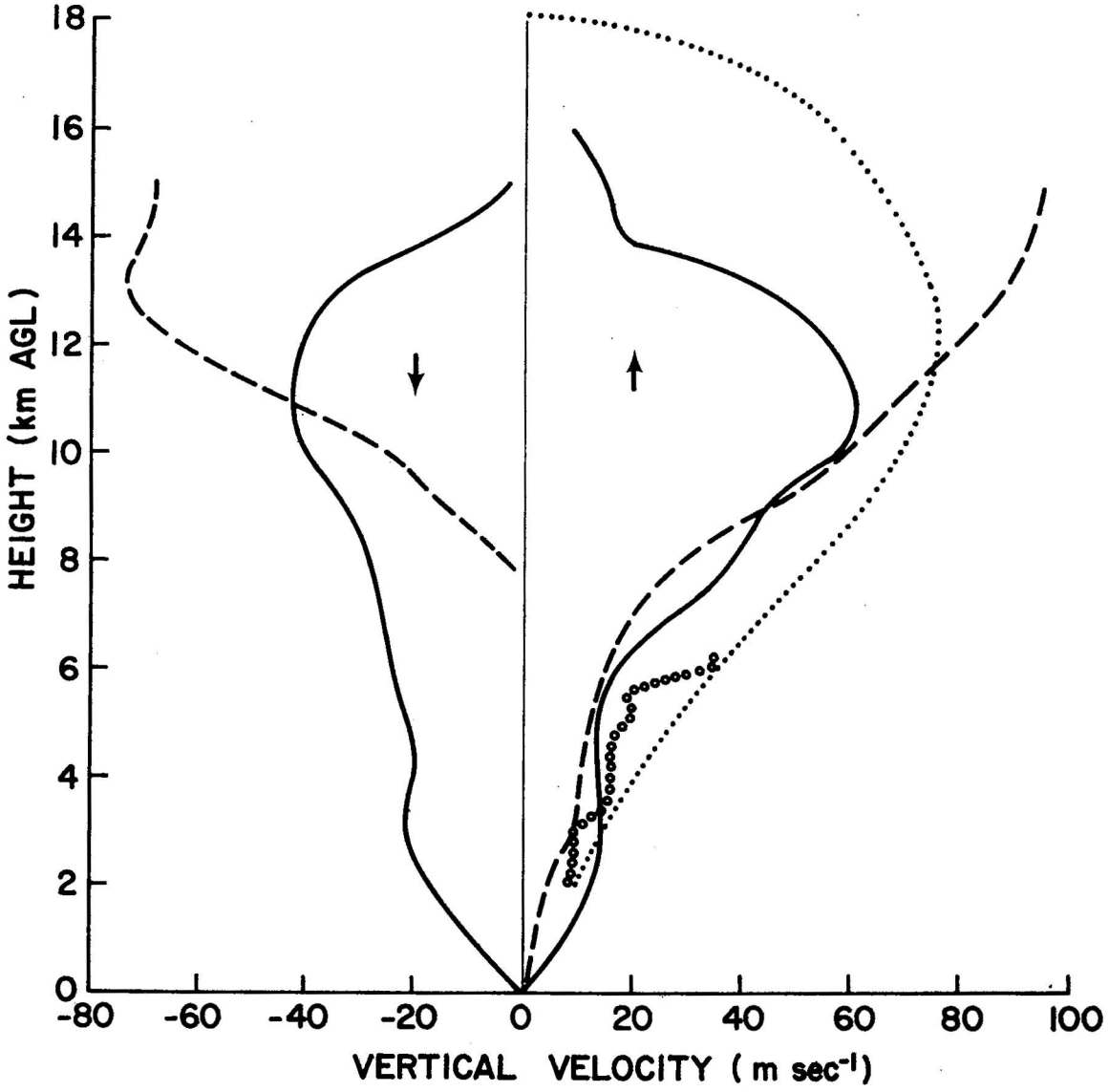

Figure 49. Profiles of strongest adjusted (solid) and unadjusted (dashed) updrafts and downdrafts at 1719. Updraft predicted from parcel theory indicated by dotted curve. Curve of open circles represents the Dibble updraft balloon sounding (see text).

1 km, it is apparent that a temperature deficit of approximately 1.8 C existed between the sub-cloud air and the undisturbed storm environment. Updrafts at 1 km in the rain area 6 km to the northeast of the aircraft position at 1740, averaged 5 m s^{-1}. Updrafts tilted to the northeast and became stronger with height on the west flank (Fig. 42e). Consequently updrafts at cloud base in the rain-free region could have been larger than 5 m s^{-1}. Furthermore, measured updrafts increased monotonically with altitude from cloud base although small decreases may have been averaged out in the data collection and analysis procedure. This information is taken as evidence that updrafts underwent uniform accelerations following the motion despite the fact that the air was negatively buoyant. Marwitz (1973) and Davies-Jones and Henderson (1974) found that the same relationship applied to deep convection on the high plains and in Oklahoma respectively. They concluded that a positive vertical perturbation pressure acceleration must be present to offset the retarding effect of negative buoyancy. The approximate vertical momentum equation appropriate for the sub-cloud layer in the absence of precipitation and assuming a horizontally uniform, locally steady updraft, may be written as

$$\frac{Dw}{Dt} = w\frac{\partial w}{\partial z} = -C_p\bar{\theta}\frac{\partial \pi'}{\partial z} + g\frac{\theta'}{\bar{\theta}} + g(0.61Q_v') \ .$$

The first right-hand-side term is the vertical perturbation pressure acceleration while the last two are the thermal and water vapor buoyancy accelerations, respectively. Consideration of the sub-cloud layer Q_v profile (Fig. 33) and the assumptions that the Q_v field is horizontally quasi-homogeneous and dominated by advection in the inflow layer, implies that Q_v' is at least one order of magnitude smaller than Q_v. Of the buoyancy terms, the thermal buoyancy is the larger by one order of magnitude in the region of temperature deficit indicated by aircraft measurements. In order for net acceleration of sub-cloud parcels to occur, therefore, the pressure term must be at least of order $g\Delta\theta'/\bar{\theta}$ or roughly 6 x 10^{-3} [m s^{-2}]. To explain observed updrafts where we assume a linear updraft profile between the surface and 1 km, the pressure term must be roughly twice the size of the observed thermal buoyancy term. We conclude that the perturbed pressure π' must decrease with height in the region below the LFC characterized by updrafts that increase monotonically with height, assuming at least quasi-steadiness of those updrafts.

A striking feature of the structure of the Wynnewood storm was the intense north flank reflectivity gradient. Since the storm moved toward the south, this feature may alternatively be called the rear flank gradient. For illustration, see Figs. 39a, 39c, 40c and 42c. In a previous section it was noted that the rear flank gradient was always north of the primary reflectivity core with strong updrafts that tilted through the core and over the gradient region. The reflectivity gradient contained weak updrafts and downdrafts at 1719, while at 1743 it was dominated by strong downdrafts. At storm mid-levels, a westerly current entered the rear flank within the strong reflectivity gradient. The reflectivity core at mid-levels was apparently being sheared off on its north flank. Since persistent and deep updrafts were not evident in the zone of shearing, abrupt precipitation fallout was encouraged. The 1641 EMC sounding shows that the dewpoint depression between cloud and environment was approximately 25°C. Hence the evaporative cooling mechanism may have caused the observed downdrafts.

Anticyclonic eddies were observed in storm mid-levels at 1719 and 1743 (Figs. 39c, 41b). These eddies resided within the updraft wake region, downstream from the zone of convergence of southerly winds within the updraft with westerly winds in the north flank jet. At no time from 1719 to 1830 was the main updraft observed to rotate cyclonically. Furthermore, no tornadoes or significant funnels were produced by the storm. The anticyclonic eddies did not arise by the starting vortex mechanism (Lemon, 1976). The flow appears to have been at least partially blocked by the updraft plume. Anticyclonic shear vorticity concentrated by convergence and advected downstream a short distance, is hypothesized as the agent of eddy formation. The strong tendency of severe storms to produce anticyclonic eddies was referred to by Lemon (1976). Since the environmental wind typically veers in severe storm situations, weaker convergence of obstacle flow and updrafts on the south flank may explain this bias. The eddies at 1719 and 1743 did not move in this period relative to the fixed earth, and consequently may in fact represent the same circulation.

Air trajectories relative to the moving storm have been generated to illustrate the essential storm core flow features for the period between 1719 and 1743. Input data are the wind analyses at these times. Analyses are superimposed to effectively remove storm motion, and the local time derivatives of the wind components are linearly approximated. The accuracy of this assumption depends on the relative lengths of dominant wave period and time difference between data sets. The first order ordinary differential equation for a particular trajectory is solved, using a second order Runge-Kutta integration algorithm and a specified initial point in space and time. A more detailed account of the method may be found in Appendix A. For these trajectories, initial points were located in or near the storm core at the 3, 7, and 11 km levels. The initial time was 1719. To avoid extrapolation, no trajectory was computed for longer than 24 minutes. The integration time increment was 60 seconds. Figure 50 displays these three dimensional trajectories with the viewer facing north. Heavy lines crossing a trajectory indicate where the 6 km mid-level has been intersected. Total elapsed time for each complete trajectory in minutes is presented near the arrowhead. The dashed 50 dBZ contour encloses the surface echo core at 1719 (Fig. 39a). The notch in the surface reflectivity core is beneath strong updrafts, since hydrometeors are carried aloft there. Trajectory 1 traces the path of a parcel originating in the strong updraft of Cell I at the 3 km level. During the first 2 minutes, the parcel experiences a vertical velocity increase of 25 m s^{-1} while moving nearly vertically. As the parcel detrains from the updraft core near 8 km, its momentum is subjected to mixing with westerly momentum of the north flank jet. Above 8 km, the outflow tilts toward the east. Trajectory 6 illustrates how outflow air initially at 11 km sinks briefly after detrainment from the updraft plume, and passes on into the outflow region. Although the compensating downdraft is initially strong at outflow levels (-40 m s^{-1} at 12 km), strong horizontal flow carries parcels rapidly across the downdraft. Essentially all of the high level outflow air may remain in the upper troposphere despite the presence of strong downdrafts. The smooth rising tendency and rapid eastward displacement of a parcel within the north flank jet, is summarized by trajectory 4. The eastward extension of the updraft within the north flank jet and outflow, may arise through the rapid advection downstream of thermal buoyancy eroded from the updraft core.

Trajectory 7 shows the path of a parcel initially within the compensating downdraft at 11 km. Detrainment from the downdraft just below 6 km is followed by weak rising and eastward translation coincident with anti-cyclonic rotation. This eddy motion is typical of the north flank shear zone. The parcel followed in trajectory 5 is initially at 7 km near the storm south flank, on the edge of the compensating downdraft. After sinking to roughly 3 km while rotating cyclonically, the parcel leaves the downdraft and moves slowly to the northwest. As shown by trajectory 2, air that enters the storm on its south flank and flows through the downdraft

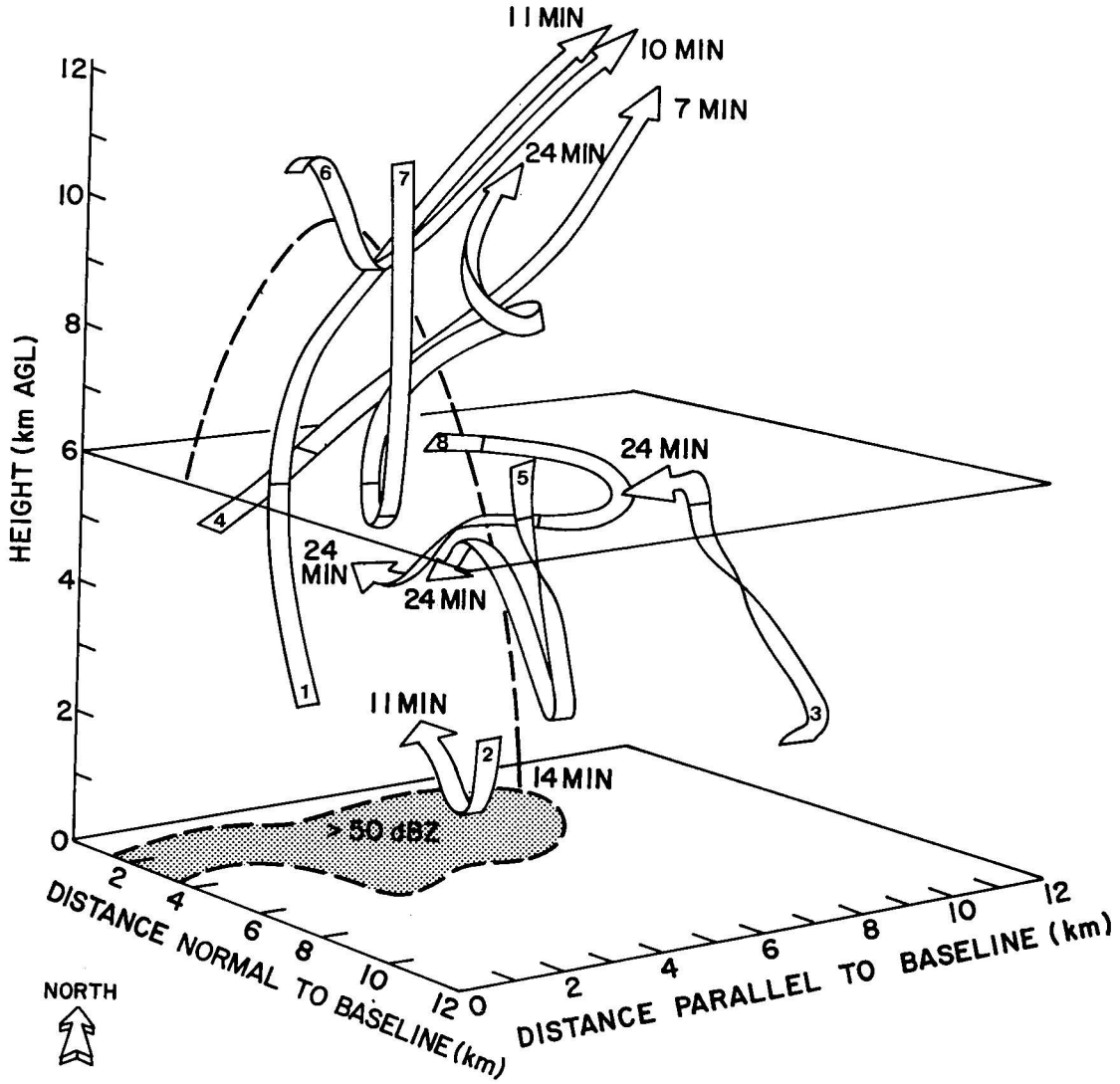

Figure 50. Air (broad arrow) and hailstone (dashed line) trajectories in the storm core between 1719 and 1743. Total elapsed time of air trajectory at arrow head. Thin line denotes intersection of 6 km plane and air trajectory. Stippling shows location of surface radar echo core at 1719.

remains in the low levels. Initially at 3 km, this parcel moves northward while sinking under the downdraft to within 900 m of the surface. It proceeds northward at low levels, eventually exiting from the storm north flank. A parcel originating farther downshear of the updraft on the south flank at 3 km (trajectory 3), flows northward while rising slowly in weak updrafts and turns westward as it nears the 6 km level. Apparently this parcel has entered the wake return flow evident at 1743 in mid-levels (Figs. 41b,c). Trajectory 8 traces the path of an air parcel, initially near 6 km, that is entrained into the developing wake return flow. As with other trajectories originating on the north edge of the wake, anticyclonic curvature characterizes the shape of trajectory 8. The fastest air displacements occur in the updraft plume, the flank jets, and low-level air that is not entrained into updrafts. The slowest displacements may be identified with air motions in decaying updrafts and the wake return flow, both features being downshear from the strongest updraft.

The Wynnewood storm produced 5 cm diameter hail, as well as large quantities of smaller hail. The growth history of these hydrometeors are of great interest. Selected hailstone trajectories have been computed, employing the continuous growth model due to Ludlam (Ludlam, 1950) and numerical methods similar to those employed in generating air trajectories. Details of the hailstone growth model are found in Appendix B. Wind data is supplied by the Doppler analyses at 1719 and 1743. Computed hail sizes may be anticipated to be smaller than the maximum observed for several reasons. First, the model allows growth to proceed only through the accretion of small supercooled cloud droplets. The neglect of stochastic growth processes prevents the modelling of chance collisions with large hydrometeors which would favor the development of larger stones. Secondly, the adiabatic liquid water content employed in the model cloud is probably an underestimate of the total water substance available for accretion to the growing hailstone. Thirdly, the Doppler data collection began only after the storm had begun to pass its peak intensity. The largest hail may already have formed and fallen from the cloud before hail trajectory simulations could be initiated. Finally, vertical velocities could not be determined through much of the southwest flank at 1743, in precisely the area where the strongest updrafts were expected. Modelled hailstones were not expected to be retained in strong updrafts for long enough periods to become very large. Hail was sampled at the surface near 1720 at the position represented by a dot in Fig. 39a. The hail sampling site is immediately to the north of the echo core as depicted in Fig. 50. Hail fell with greatest frequency within the 1-2 cm diameter category at this location. The heavy dashed line in Fig. 50 represents the trajectory (relative to the moving storm) of the largest simulated hailstone, which originated as an embryonic 2 mm frozen raindrop at 6.5 km and a temperature of -7°C. The greatest altitude achieved while the stone was within the strong updraft was 10 km. A diameter of 2.14 cm was attained before the stone fell through the freezing level. The stone was displaced approximately 7 km in the horizontal from the point of origin to the position where it reached the ground. Melting reduced the hailstone diameter to 1.64 cm in the 4 minutes that it was below the freezing level. The histories of the largest simulated hailstone and of three additional stones are presented in Fig. 51. Hailstones represented by curves 1, 3, and 4 originated in the -7°C thru -10°C layer while the remaining hailstone originated high in the cloud at -32°C. Liquid water content

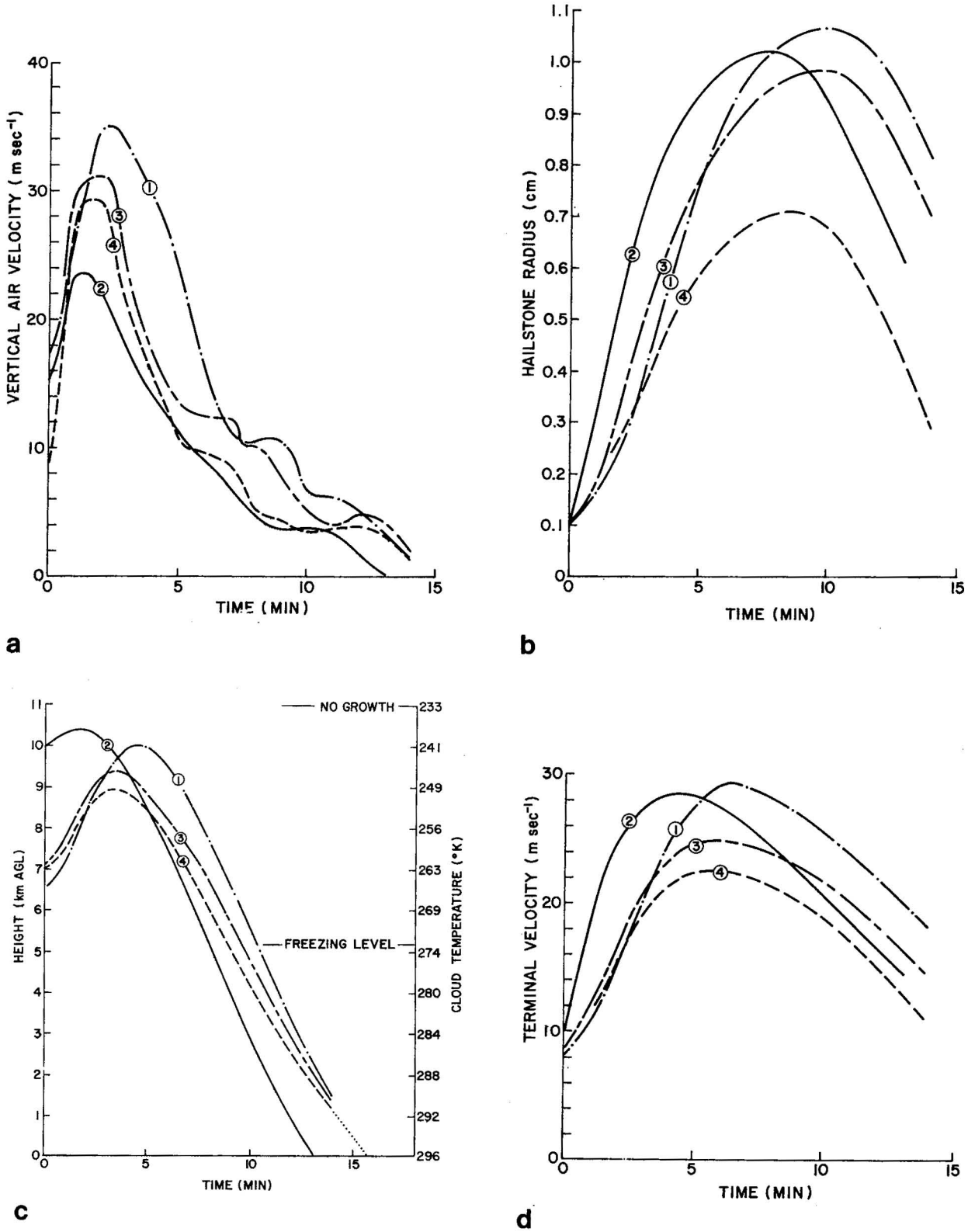

Figure 51. Growth histories of 4 simulated hailstones. Panel (a) gives evolution of updraft experienced by hailstones. Panels (b), (c) and (d) illustrate the evolution of radius, height, and terminal velocity, respectively. Vertical coordinate intercepts show initial conditions.

experienced by all stones during the 8-10 minute residence period in the growth region was roughly 6 gm m^{-3}. The larger stones are seen to have spent more time in the growth region, primarily due to the existence of strong updrafts. All hailstones had begun to fall after 5 minutes since vertical velocities peaked before this time. Accordingly, stones did not recirculate. Large growth rates occurred at low temperatures within strong updrafts. The peak radius of hailstone 2 nearly equals hailstone 1 for this reason despite experiencing significantly weaker peak updrafts. As an example of the significance of hailstone melting, a stone with a growth history similar to that of hailstone 4 and a maximum radius less than 0.5 cm would melt before reaching the ground. The melting process causes greater shrinkage of initially smaller hailstones whose lower terminal velocities allow these to remain longer within the melting layer. Between the freezing level and the ground, the hail size spectrum should shift towards smaller radii with an overall decrease in number density. Growth in all simulated hailstones proceeded in the wet regime as a consequence of the high adiabatic liquid water content. All modeled hailstones were composed of hard, clear ice due to wet growth. Although Ludlam's model can simulate hailstones with a "ringed" or onionskin structure, such stones were not produced here. In summary, a simple hail growth model has been applied to real data and appears to simulate average growth histories with reasonable success. This conclusion is based primarily on the rough agreement between the sizes of observed and simulated stones.

3.3.6 Summary and Conclusions

Three distinctive features of the convective storm that developed near Wynnewood in south-central Oklahoma on the afternoon of 28 May 1977 are: 1) the storm's motion, 90 deg to the right of the mean wind of the cloud-bearing layer; 2) the storm's isolation from other convective activity on 28 May; 3) the storm's production of large hail.

The synoptic discussion reveals that the storm's parent airmass was convectively unstable and that it possessed abundant low level moisture. Convection was initiated by surface heating and low level convergence along a pre-existing mesoscale cold front. In the absence of an upper level disturbance, convection was localized.

A study of photographs and a time-lapse movie of the storm indicates intense and persistent west flank cloud development. The observations suggest that westward propagation can explain the storm's extreme right-moving tendency. Examination of the WSR-57 radar photographs establishes the dominance of continuous propagation of the main storm echo.

Internal storm structure, deduced from the variationally formulated analysis of five dual Doppler radar data sets spaced over a one hour period, reveals that the strongest updrafts were located within the western portion of the radar echo volume. This result is related to photographic observations of the storm. An excellent visual correlation exists between locations of updraft plumes and reflectivity maxima aloft. These observations support the contention that strong updrafts are regions of large hydrometeor growth and accumulation. Derived updrafts are capable of supporting large hail, which the storm produced in quantity. Simulated hailstones up to 2 cm in

diameter were produced by employing a simple cloud/hail growth model and dual Doppler derived wind fields. Strong, deep downdrafts were observed. Results of air trajectory computations within the storm core suggest that air, transported into the upper troposphere by updrafts, remains at high levels despite the presence of deep downdrafts.

The study demonstrates the ability of the variationally formulated dual Doppler analysis to yield improved, physically consistent vertical wind fields within a deep convective storm.

4. CONCLUSIONS

The principle goal of this variational dual Doppler data analysis is to improve vertical velocity estimates, where conventional methods often yield physically inconsistent results. Case studies demonstrate that this goal is achieved. With a better estimate of vertical velocity for the kinematic upper boundary condition, results could be further improved. Additional analysis improvements can be realized through reduction of filtering and an expanded specification of errors in the adjustment procedure. Application of this technique yields wind fields which support the growth of hail in general agreement with independent surface observations.

5. ACKNOWLEDGMENTS

The author wishes to express his appreciation to Dr. Peter Ray, who suggested the subject of this research and contributed generously of his time and insight throughout the study. The many helpful suggestions offered by Prof. Yoshi Sasaki of Oklahoma University and by Drs. Robert Davies-Jones and Carl Hane of the National Severe Storms Laboratory are gratefully acknowledged. The author expresses his appreciation to the many members of the NSSL, NCAR and Illinois State Water Survey staffs who rendered support to the multiple Doppler and surface data collection efforts. The graphic and arts services of Mrs. Jennifer Moore and Mr. Charles Clark are gratefully acknowledged. The manuscript was typed by Ms. Sandy Mudd and Ms. Connie Hall. This research was partially supported by NOAA Contract 03-6-022-35148 to the University of Illinois, the Atmospheric Sciences Section, National Science Foundation under Grant #ATM 77-04285 to Florida State University, and by the National Center for Atmospheric Research, Research Aviation Facility, Project 7-493. NCAR is sponsored by the National Science Foundation.

6. REFERENCES

Armijo, L., 1969: A theory for the determination of wind and precipitation velocities with Doppler radars. J. Atmos. Sci., 26, 566-569.

Barnes, S. L., 1970: Some aspects of a severe right-moving thunderstorm deduced from mesonetwork rawinsonde observations. J. Atmos. Sci., 27, 634-648.

Brandes, E. A., 1977: Flow in severe thunderstorms observed by dual-Doppler radar. Mon. Wea. Rev., 105, 113-120.

Browning, K. A., T. W. Harrold, A. J. Whyman and J. G. D. Beimers, 1968: Horizontal and vertical air motion, and precipitation growth, within a shower. Proceedings, 13th Radar Meteor. Conf., Boston, Mass., Amer. Meteor. Soc., 122-127.

Cressman, G. P., 1959: An operational objective analysis system. Mon. Wea. Rev., 87, 367-374.

Danielsen, E. F., R. Bleck and D. A. Morris, 1972: Hail growth by stochastic collection in a cumulus model. J. Atmos. Sci., 29, 135-155.

Davies-Jones, R. P., 1974: Discussion of measurements inside high-speed thunderstorm updrafts. J. Appl. Meteor., 13, 710-717.

_____, and J. H. Henderson, 1974: Updraft properties deduced from rawinsoundings. NOAA Tech. Memo. ERL NSSL-72, Norman, National Severe Storms Lab., 117 pp.

Doviak, R. J., P. S. Ray, R. G. Strauch and L. J. Miller, 1976: Error estimation in wind fields derived from dual-Doppler radar measurement. J. Appl. Meteor., 15, 868-878.

Foote, G. B., and P. S. du Toit, 1969: Terminal velocity of raindrops aloft. J. Appl. Meteor., 8, 249-253.

Frisch, A. S., L. J. Miller and R. J. Strauch, 1974: Three-dimensional air motion measured in snow. Geophys. Res. Lett., 1, 86-89.

Hane, C. E., 1973: The squall line thunderstorm: numerical experimentation. J. Atmos. Sci., 30, 1672-1690.

Joss, J., and D. Waldvogel, 1970: Raindrop size distribution and Doppler velocities. Preprints, 14th Radar Meteor. Conf., Tucson, Ariz., Amer. Meteor. Soc., 153-156.

Kropfli, R. A., and L. J. Miller, 1976: Kinematic structure and flux quantities in a convective storm from dual-Doppler radar observations. J. Atmos. Sci., 33, 520-529.

Lemon, L. R., 1976: Wake vortex structure and aerodynamic origin in severe thunderstorms. J. Atmos. Sci., 33, 678-685.

Lhermitte, R. M., and L. J. Miller, 1970: Doppler radar methodology for the observation of convective storms. Preprints, 14th Radar Meteor. Conf., Tucson, Ariz., 133-138.

Ludlam, F. H., 1950: The composition of coagulation elements in cumulonimbus. Q. J. R. Meteorol. Soc., 76, 52-58.

Marwitz, J. D., 1973: Non-hydrostatic pressures in severe thunderstorms. Preprints, 8th Conf. on Severe Local Storms, Denver, Colo., 14-17.

Mathur, M. B., 1972: Simulation of an asymmetric hurricane with a fine mesh multiple grid primitive equation model. Report No. 72-1, Pt. III, Dept. of Meteorology, Florida State University, 162 pp.

McGinley, J. A., 1973: Environmental energy fields associated with severe storms. Masters' Thesis, University of Oklahoma, Norman, Okla., 129 pp.

Miller, L. J., 1975: Internal airflow of a convective storm from dual Doppler radar measurements. Pageoph, 113, 765-785.

_____, and R. G. Strauch, 1974: A dual Doppler radar method for the determination of wind velocities within precipitating weather systems. Remote Sensing of Environment, 3, 219-235.

Miller, R. C., 1972: Notes on analysis and severe-storm forecasting procedures of the Air Force global weather central. Tech. Rept. 200 (REV), Air Weather Service (MAC), USAF.

Newton, C. W., 1966: Circulations in large sheared cumulonimbus. Tellus, 18, 699-713.

O'Brien, J. J., 1970: Alternative solutions to the classical vertical velocity problem. J. Appl. Meteor., 9, 197-203.

Ogura, Y., and N. A. Phillips, 1962: Scale analysis of deep and shallow convection in the atmosphere. J. Atmos. Sci., 19, 173-179.

Peace, R. L., Jr., and R. A. Brown, 1968: Comparison of single and double Doppler radar velocity measurements in convective storms. Preprints, 13th Radar Meteor. Conf., Montreal, Canada, 464-473.

Ray, P. S., R. J. Doviak, G. B. Walker, D. Sirmans, J. Carter and B. Bumgarner, 1975: Dual-Doppler observation of a tornadic storm. J. Appl. Meteor., 14, 1521-1530.

___, and K. K. Wagner, 1976: Multiple Doppler radar observations of storms. Geophys. Res. Lett., 3, 189-191.

___, and C. L. Ziegler, 1977: De-aliasing first-moment Doppler estimates. J. Appl. Meteor., 16, 563-564.

___, K. K. Wagner, K. W. Johnson, J. J. Stephens, W. C. Bumgarner and E. A. Mueller, 1978: Triple Doppler observations of a convective storm. J. Appl. Meteor., 17, 1201-1212.

Sasaki, Y., 1958: An objective analysis based on the variational method. J. Meteor. Soc., Japan, 36, 77-88.

_____, 1970: Some basic formalisms in numerical variational objective analysis. Mon. Wea. Rev., 98, 875-883.

Sirmans, D., and B. Bumgarner, 1975: Numerical comparison of five mean frequency estimators. J. Appl. Meteor., 14, 991-1003.

Srivastava, R. C., 1967: A study of the effect of precipitation on cumulus dynamics. J. Atmos. Sci., 24, 36-45.

Stephens, J. J., 1965: A variational approach to numerical weather analysis and prediction. Report No. 3, Atmos. Sci. Group, The University of Texas, Austin, 243 pp.

_____, 1967: Filtering responses of selected distance-dependent weight functions. Mon. Wea. Rev., 95, 45-46.

_____, and J. M. Stitt, 1970: Optimum influence radii for interpolation with the method of successive corrections. Mon. Wea. Rev., 98, 680-687.

_____, and A. L. Polan, 1971: Spectral modification by objective analysis. Mon. Wea. Rev., 99, 374-378.

Wagner, K. K., 1971: Variational analysis using observational and low pass filtering constraints. Masters' Thesis, University of Oklahoma, Norman, Okla., 39 pp.

Whittaker, E., and G. Robinson, 1944: The calculus of observations. London, Blackie and Son, Ltd., 397 pp.

Wilhelmson, R., and Y. Ogura, 1972: The pressure perturbation and the numerical modeling of a cloud. J. Atmos. Sci., 29, 1295-1307.

_____, 1974: The life cycle of a thunderstorm in three dimensions. J. Atmos. Sci., 31, 1629-1651.

Wisner, C., H. D. Orville and C. Myers, 1972: A numerical model of a hail-bearing cloud. J. Atmos. Sci., 29, 1160-1181.

APPENDIX A

Method for Generating Trajectories

APPENDIX A

Generation of trajectories requires the solution of the first-order ordinary differential equation

$$\frac{ds}{dt} = V(x,y,z,t) \qquad A(1)$$

by numerical methods. Distance along a trajectory is denoted by s. The three-dimensional storm-relative air velocity, denoted by V, is known only at regular gridpoints. Hence, V must be interpolated to points on the particle trajectory. The second order Runge-Kutta algorithm of the form

$$y(n+1) = y(n) + h[K_1 f(x(n),y(n)) + K_2 f(x(n) + \alpha h, y(n) + \beta h f(x(n),y(n)))] \qquad A(2)$$

is selected for integration of Eq. A(1) due to its relative computational ease and accuracy. This scheme is equivalent to a quadratic Taylor algorithm. For these integrations, we choose $K_1 = K_2 = 0.5$ and $\alpha = \beta = 1$. With these coefficients, Eq. A(2) may be written as

$$y(n+1) = y(n) + \frac{h}{2}[f(x(n),y(n)) + f(x(n) + h, y(n) + hf(x(n),y(n)))] \qquad A(3)$$

Particle displacement is resolved into its components in the $\hat{x}$, $\hat{y}$, and $\hat{z}$ directions through the integration of Eq. A(3) for each component. The accuracy of interpolation of wind components at gridpoints to trajectory points is essential to suppress the fictitious numerical dispersion of computed trajectories. Wherever possible, a 27-point formula of the form

$$V(P) = \sum_{i=I-1}^{I+1} \sum_{j=J-1}^{J+1} \sum_{k=K-1}^{K+1} V_{i,j,k} \prod_{\substack{\ell=I-1 \\ \ell\neq i}}^{I+1} \frac{x-x_\ell}{x_i-x_\ell} \prod_{\substack{m=J-1 \\ m\neq j}}^{J+1} \frac{y-y_m}{y_j-y_m} \prod_{\substack{n=K-1 \\ n\neq k}}^{K+1} \frac{z-z_n}{z_k-z_n} \qquad A(4)$$

is employed to interpolate a wind component V to the trajectory point P. V is assumed to vary quadratically in x, y, and z. The point located by the indices (i,j,k) centers a grid region $2\delta x \times 2\delta y \times 2\delta z$ in volume. If data is not available at all 27 points, a data search is conducted at the 8 corner points of a grid cube $\delta x \times \delta y \times \delta z$ in volume in which the point P resides. If data is available, an 8 point interpolation formula of the form

$$V(P) = \sum_{i=I}^{I+1} \sum_{j=J}^{J+1} \sum_{k=K}^{K+1} V_{i,j,k} \prod_{\substack{\ell=I \\ \ell\neq i}}^{I+1} \frac{x-x_\ell}{x_i-x_\ell} \prod_{\substack{m=J \\ m\neq j}}^{J+1} \frac{y-y_m}{y_j-y_m} \prod_{\substack{n=K \\ n\neq k}}^{K+1} \frac{z-z_n}{z_k-z_n} \qquad A(5)$$

is used. This expresses linear variation of V in x, y, and z. If neither of these options is open, the trajectory is terminated. The quadratic interpolation scheme is an extension of the formula used by Mathur (1972) in a quasi-lagrangian time integration scheme of a multi-level primitive equation model.

APPENDIX B

Method for Generating Hailstone Trajectories

APPENDIX B

The problem of generating hailstone trajectories requires the choice of a suitable model for hailstone growth following the motion of the stone as well as a method of computing displacements. The differential equation governing hail trajectories is identical in form to Eq. A(1) in Appendix A for air trajectories. The treatment of vertical displacement is different in that vertical hailstone motion is the sum of the terminal velocity and vertical air motion. The algorithm for computing the trajectories is Eq. A(3), while A(4) and A(5) manage the necessary interpolation of air motion components. The model of hailstone evolution chosen for these studies allows for wet and/or dry growth and melting. The equations for the growth phase are adapted from Ludlam (1950) who modeled this growth as a continuous process in which supercooled cloud droplets are accreted and frozen on the stone surface. Water drop and ice particle size distributions are not considered. Hence, the growth may best be considered as an average rather than a stochastic process as in the work of Danielsen et al. (1972). The growth equations are founded on the concept of a heat balance condition for the stone. The release of the heat of fusion is balanced by conduction and evaporation heat transfer in such a manner that collected water may be frozen while the hailstone surface temperature is maintained at 0°C. A critical ambient liquid water content w_c may be derived such that all or only a portion of the accreted water is frozen, depending upon whether the ambient liquid water content is above or below w_c. This condition determines whether growth proceeds in the dry regime (all accreted water frozen) or the wet regime (part of accreted water frozen and excess shed). In the wet regime, a thin film of water uniformly covers the surface of the hailstones. The parameter w_c is computed at each trajectory point from

$$w_c = \frac{2X(2V_H r_H \rho_a/\mu)^{1/2}}{E r_H V_H} \quad \frac{K(T_H - T_a)}{[C_w(T_a - T_o) + L_f]} \quad , \qquad B(1)$$

where condensation effects have been neglected here and,

E is the average collection efficiency (1.0);

r_H is the radius of the spherical hailstone;

V_H is the difference between hailstone terminal velocity and vertical air motion;

L_f is the latent heat of fusion (74.5 cal g^{-1});

C_w is the specific heat of water (1.02 cal $g^{-1}K^{-1}$);

T_o is a reference temperature (equals 0°C);

T_a is the ambient air temperature;

T_H is the hailstone surface temperature (0°C);

K is the thermal conductivity of the air (2.36 x 10^3erg $cm^{-1}s^{-1}K^{-1}$);

μ is the dynamic viscosity of air (1.667×10^{-4} g cm^{-1} s^{-1});

ρ_a is air density;

χ is a constant (equals 0.6).

Values of constants and parameters are noted beside the definition.

For dry growth with ambient liquid water content $w \leq w_c$, the expression for the growth rate is

$$\frac{dr_H}{dt} = \frac{EV_H w}{4\rho i} \quad , \qquad B(2)$$

where ρ_i is the density of accreted water after freezing. In these studies, ρ_i took a value of 0.9 g cm^{-3}. For the case where $w > w_c$, the wet growth rate is determined from

$$\left(\frac{r_H}{V_H}\right)^{1/2} \frac{dr_H}{dt} = \left(\frac{2\rho_a}{\mu}\right)^{1/2} \frac{\chi}{2\rho_i} \frac{K(T_H - T_a)}{C_w(T_a - T_o) + L_f} \quad . \qquad B(3)$$

The ambient cloud is modeled in terms of moist adiabatic updraft properties. Pressure, temperature, density, and liquid water content are determined from a proximity sounding at 1 km intervals from cloud base to the tropopause. The surface temperature is approximated by the sounding wet-bulb temperature since hail falls to the ground within a precipitation shaft. Hailstone melting occurs via heat conduction from the air and from accreted cloud droplets and is the only active process when the ambient temperature is above freezing. Following the treatment of Wisner et al (1972), the melting rate may be expressed as

$$\frac{dr_H}{dt} = -\left[1.6 + 0.3\left(\frac{2V_H r_H \rho_a}{\mu}\right)^{1/2}\right] \frac{2K(T_a - T_o)}{L_f \rho_i r_H} - \frac{C_w}{L_f}(T_a - T_o)\frac{EV_H w}{4\rho_i} \quad . \qquad B(4)$$

This model is probably not capable of simulating the largest hailstones in a given storm since these are thought to be statistically fortunate in accreting supercooled raindrops and smaller hail in the process of attaining their large size. Although the actual cloud had liquid water content which was probably significantly non-adiabatic, the chosen model cloud is considered to be an acceptable approximation in view of the simplistic hail growth model employed. Estimated radar reflectivity could not be related to liquid water content because unknown quantities of hail probably had a great influence on returned power.

APPENDIX C

Variational Algorithm to Impose Continuity on Interpolated Cartesian Wind Field

APPENDIX C

Consider u, v, and w wind components interpolated to a cartesian grid. We desire that the anelastic equation of continuity,

$$\frac{\partial u}{\partial x} + \frac{\partial v}{\partial y} + \frac{\partial w}{\partial z} + \kappa w = 0 \quad , \qquad C(1)$$

be exactly satisfied throughout the domain D. We minimize the first variation of the functional I where

$$I = \sum_i \sum_j \sum_k \alpha(u-\tilde{u})^2 + \beta(v-\tilde{v})^2 + \gamma(w-\tilde{w})^2 + \lambda\left(\frac{\partial u}{\partial x} + \frac{\partial v}{\partial y} + \frac{\partial w}{\partial z} + \kappa w\right) \quad . \qquad C(2)$$

By rules of commutation, there follows

$$\delta I = \sum_i \sum_j \sum_k \left(2\alpha(u-\tilde{u}) - \frac{\partial \lambda}{\partial x}\right)\delta u + \left(2\beta(v-\tilde{v}) - \frac{\partial \lambda}{\partial y}\right)\delta v$$

$$+ \left(2\gamma(w-\tilde{w}) - \frac{\partial \lambda}{\partial z} + \kappa\lambda\right)\delta w = 0 \quad . \qquad C(3)$$

All finite-difference boundary terms are implicit in Eq. C(3). Since δu, δv, and δw are arbitrary on the interior of D, we obtain the following Euler-Lagrange equations:

$$2\alpha(u-\tilde{u}) - \frac{\partial \lambda}{\partial x} = 0 \quad , \qquad C(4)$$

$$2\beta(v-\tilde{v}) - \frac{\partial \lambda}{\partial y} = 0 \quad , \qquad C(5)$$

$$2\gamma(w-\tilde{w}) - \frac{\partial \lambda}{\partial z} + \kappa\lambda = 0 \quad . \qquad C(6)$$

Equation C(1) is the fourth analysis equation.

Since interpolation error may be considered a random event, we might assume that the precision moduli α, β, and γ are constants. In this case, the second order partial differential equation for λ is

$$\frac{1}{2\alpha}\frac{\partial^2 \lambda}{\partial x^2} + \frac{1}{2\beta}\frac{\partial^2 \lambda}{\partial y^2} + \frac{1}{2\gamma}\frac{\partial^2 \lambda}{\partial z^2} - \frac{\kappa^2}{2\gamma}\lambda = \frac{\partial \tilde{u}}{\partial x} + \frac{\partial \tilde{v}}{\partial y} + \frac{\partial \tilde{w}}{\partial z} + \kappa\tilde{w} \quad . \qquad C(7)$$

Equation C(7) is of the Helmholtz-type and may be solved by an SOR technique with a proper specification of boundary terms. Equations C(4), C(5), and C(6) are then employed to deduce u, v, and w from $\tilde{u}$, $\tilde{v}$, and $\tilde{w}$.

NATIONAL SEVERE STORMS LABORATORY

The NSSL Technical Memorandum, beginning with No. 28, continue the sequence established by the U. S. Weather Bureau National Severe Storms Project, Kansas City, Missouri. Numbers 1-22 were designated NSSP Reports. Numbers 23-27 were NSSL Reports, and 24-27 appeared as subseries of Weather Bureau Technical Notes. These reports are available from the National Technical Information Service, Operations Division, Springfield, Virginia 22151, for $3.00 and a microfiche version for $0.95. NTIS numbers are given below in parentheses.

No. 1 National Severe Storms Project Objectives and Basic Design. Staff, NSSP. March 1961, 16 p. (PB-168207)

No. 2 The Development of Aircraft Investigations of Squall Lines from 1956-1960. B. B. Goddard. 34 p. (PB-168208)

No. 3 Instability Lines and Their Environments as Shown by Aircraft Soundings and Quasi-Horizontal Traverses. D. T. Williams. February 1962. 15 p. (PB-168209)

No. 4 On the Mechanics of the Tornado. J. R. Fulks. February 1962. 33 p. (PB-168210)

No. 5 A Summary of Field Operations and Data Collection by the National Severe Storms Project in Spring 1961. J. T. Lee. March 1962. 47 p. (PB-165095)

No. 6 Index to the NSSP Surface Network. T. Fujita. April 1962. 32 p. (PB-168212)

No. 7 The vertical structure of Three Dry Lines as Revealed by Aircraft Traverses. E. L. McGuire. April 1962. 10 p. (PB-168213)

No. 8 Radar Observations of a Tornado Thunderstorm in Vertical Section. Ralph J. Donaldson, Jr. April 1962. 21 p. (PB-174859)

No. 9 Dynamics of Severe Convective Storms. Chester W. Newton. July 1962. 44 p. (PB-163319)

No. 10 Some Measured Characteristics of Severe Storms Turbulence. Roy Steiner and Richard H. Rhyne. July 1962. 17 p. (N62-16401)

No. 11 A Study of the Kinematic Properties of Certain Small-Scale Systems. D. T. Williams. October 1962. 22 p. (PB-168216)

No. 12 Analysis of the Severe Weather Factor in Automatic Control of Air Route Traffic. W. Boynton Beckwith. December 1962. 67 p. (PB-168217)

No. 13 500-Kc./Sec. Sferics Studies in Severe Storms. Douglas A. Kohl and John E. Miller. April 1963. 36 p. (PB-168218)

No. 14 Field Operations of the National Severe Storms Project in Spring 1962. L. D. Sanders. May 1963. 71 p. (PB-168219)

No. 15 Penetrations of Thunderstorms by an Aircraft Flying at Supersonic Speeds. G. P. Roys. Radar Photographs and Gust Loads in Three Storms of 1961 Rough Rider. Paul W. J. Schumacher. May 1963. 19 p. (PB-168220)

No. 16 Analysis of Selected Aircraft Data from NSSP Operations, 1962. T. Fujita. May 1963. 29 p. (PB-168221)

No. 17 Analysis of Methods for Small-Scale Surface Network Data. D. T. Williams. August 1963. 20 p. (PB-168222)

No. 18 The Thunderstorm Wake of May 4, 1961. D. T. Williams. August 1963. 23 p. (PB-168223)

No. 19 Measurements by Aircraft of Condensed Water in Great Plains Thunderstorms. George P. Roys and Edwin Kessler. July 1966. 17 p. (PB-173048)

No. 20 Field Operations of the National Severe Storms Project in Spring 1963. J. T. Lee, L. D. Sanders, and D. T. Williams. January 1964. 68 p. (PB-168224)

No. 21 On the Motion and Predictability of Convective Systems as Related to the Upper Winds in a Case of Small Turning of Wind with Height. James C. Fankhauser. January 1964. 36 p. (PB-168225)

No. 22 Movement and Development Patterns of Convective Storms and Forecasting the Probability of Storm Passage at a Given Location. Chester W. Newton and James C. Fankhauser. January 1964. 53 p. (PB-168226)

No. 23 Purposes and Programs of the National Severe Storms Laboratory, Norman, Oklahoma. Edwin Kessler. December 1964. 17 p. (PB-166675)

No. 24 Papers on Weather Radar, Atmospheric Turbulence, Sferics and Data Processing. August 1965. 139 p. (AD-621586)

No. 25 A Comparison of Kinematically Computed Precipitation with Observed Convective Rainfall. James C. Fankhauser. September 1965. 28 p. (PB-168445)

No. 26 Probing Air Motion by Doppler Analysis of Radar Clear Air Returns. Roger M. Lhermitte. May 1966. 37 p. (PB-170636)

No. 27 Statistical Properties of Radar Echo Patterns and the Radar Echo Process. Larry Armijo. May 1966. The Role of the Kutta-Joukowski Force in Cloud Systems with Circulation. J. L. Goldman. May 1966. 34 p. (PB-170756)

No. 28 Movement and Predictability of Radar Echoes. James Warren Wilson. November 1966. 30 p. (PB-173972)

No. 29 Notes on Thunderstorm Motions, Heights, and Circulations. T. W. Harrold, W. T. Roach, and Kenneth E. Wilk. November 1966. 51 p. (AD-644899)

No. 30 Turbulence in Clear Air Near Thunderstorms. Anne Burns, Terence W. Harrold, Jack Burnham, and Clifford S. Spavins. December 1966. 20 p. (PB-173992)

No. 31 Study of a Left-Moving Thunderstorm of 23 April 1964. George R. Hammond. April 1967. 75 p. (PB-174681)

No. 32 Thunderstorm Circulations and Turbulence from Aircraft and Radar Data. James C. Fankhauser and J. T. Lee. April 1967. 32 p. (PB-174860)

No. 33 On the Continuity of Water Substance. Edwin Kessler. April 1967. 125 p. (PB-175840)

No. 34 Note on the Probing Balloon Motion by Doppler Radar. Roger M. Lhermitte. July 1967. 14 p. (PB-175930)

No. 35 A Theory for the Determination of Wind and Precipitation Velocities with Doppler Radars. Larry Armijo. August 1967. 20 p. (PB-176376)

No. 36 A Preliminary Evaluation of the F-100 Rough Rider Turbulence Measurement System. U. O. Lappe. October 1967. 25 p. (PB-177037)

No. 37 Preliminary Quantitative Analysis of Airborne Weather Radar. Lester P. Merritt. December 1967. 32 p. (PB-177188)

No. 38 On the Source of Thunderstorm Rotation. Stanley L. Barnes. March 1968. 28 p. (PB-178990)

No. 39 Thunderstorm - Environment Interactions Revealed by Chaff Trajectories in the Mid-Troposphere. James C. Fankhauser. June 1968. 14 p. (PB-179659)

No. 40 Objective Detection and Correction of Errors in Radiosonde Data. Rex L. Inman. June 1968. 50 p. (PB-180284)

No. 41 Structure and Movement of the Severe Thunderstorms of 3 April 1964 as Revealed from Radar and Surface Mesonetwork Data Analysis. Jess Charba and Yoshikazu Sasaki. October 1968. 47 p. (PB-183310)

No. 42 A Rainfall Rate Sensor. Brian E. Morgan. November 1968. 10 p. (PB-183979)

No. 43 Detection and Presentation of Severe Thunderstorms by Airborne and Ground-based Radars: A Comprehensive Study. Kenneth E. Wilk, John K. Carter, and J. T. Dooley. February 1969. 56 p. (PB-183572)

No. 44 A Study of a Severe Local Storm of 16 April 1967. George Thomas Haglund. May 1969. 54 p. (PB-184970)

No. 45 On the Relationship Between Horizontal Moisture Convergence and Convective Cloud Formation. Horace R. Hudson. March 1970. 29 p. (PB-191720)

No. 46 Severe Thunderstorm Radar Echo Motion and Related Weather Events Hazardous to Aviation Operations. Peter A. Barclay and Kenneth E. Wilk. June 1970. 63 p. (PB-192498)

No. 47 Evaluation of Roughness Lengths at the NSSL-WKY Meteorological Tower. Leslie D. Sanders and Allen H. Weber. August 1970. 24 p. (PB-194587)

No. 48 Behavior of Winds in the Lowest 1500 ft in Central Oklahoma: June 1966-May 1967. Kenneth C. Crawford and Horace R. Hudson. August 1970. 57 p. (N71-10615)

No. 49 Tornado Incidence Maps. Arnold Court. August 1970. 76 p. (COM-71-00019)

No. 50 The Meteorologically Instrumented WKY-TV Tower Facility. John K. Carter. September 1970. 18 p. (COM-71-00108)

No. 51 Papers on Operational Objective Analysis Schemes at the National Severe Storms Forecast Center. Rex L. Inman. November 1970. 91 p. (COM-71-00136)

No. 52 The Exploration of Certain Features of Tornado Dynamics Using a Laboratory Model. Neil B. Ward. November 1970. 22 p. (COM-71-00139)

No. 53 Rawinsonde Observation and Processing Techniques at the National Severe Storms Laboratory. Stanley L. Barnes, James H. Henderson and Robert J. Ketchum. April 1971. 245 p. (COM-71-00707)

No. 54 Model of Precipitation and Vertical Air Currents. Edwin Kessler and William C. Bumgarner. June 1971. 93 p. (COM-71-00911)

No. 55 The NSSL Surface Network and Observations of Hazardous Wind Gusts. Operations Staff. June 1971. 20 p. (COM-71-00910)

No. 56 Pilot Chaff Project at the National Severe Storms Laboratory. Edward A. Jessup. November 1971. 36 p. (COM-72-10106)

No. 57 Numerical Simulation of Convective Vortices. Robert P. Davies-Jones and Glenn T. Vickers. November 1971. 27 p. (COM-72-10269).

No. 58 The Thermal Structure of the Lowest Half Kilometer in Central Oklahoma: December 9, 1966-May May 31, 1967. R. Craig Goff and Horace R. Hudson. July 1972. 53 p. (COM-72-11281)

No. 59 Cloud-to-Ground Lightning Versus Radar Reflectivity in Oklahoma Thunderstorms. Gilbert D. Kinzer. September 1972. 24 p. (COM-73-10050)

No. 60 Simulated Real Time Displays of Velocity Fields by Doppler Radar. L. D. Hennington and G. B. Walker. November 1972. 10 p. (COM-73-10515)

No. 61 Gravity Current Model Applied to Analysis of Squall-Line Gust Front. Jess Charba. November 1972. 58 p. (COM-73-10410)

No. 62 Mesoscale Objective Map Analysis Using Weighted Time-Series Observations. Stanley L. Barnes. March 1973. 60 p. (COM-73-10781)

No. 63 Observations of Severe Storms on 26 and 28 April 1971. Charles L. Vlcek. April 1973. 19 p. (COM-73-11200)

No. 64 Meteorological Radar Signal Intensity Estimation. Dale Sirmans and R. J. Doviak. September 1973. 80 p. (COM-73-11923/2AS)

No. 65 Radisonde Altitude Measurement Using Double Radiotheodolite Techniques. Stephan P. Nelson. September 1973. 20 p. (COM-73-11932/9AS)

No. 66 The Motion and Morphology of the Dryline. Joseph T. Schaefer. September 1973. 81 p. (COM-74-10043)

No. 67 Radar Rainfall Pattern Optimizing Technique. Edward A. Brandes. March 1974. 16 p. (COM-74-10906/AS)

No. 68 The NSSL/WKY-TV Tower Data Collection Program: April-July 1972. R. Craig Goff and W. David Zittel. May 1974. 45 p. (COM-74-11334/AS)

No. 69 Papers on Oklahoma Thunderstorms, April 29-30, 1970. Stanley L. Barnes, Editor. May 1974. 147 p. (COM-74-11474/AS)

No. 70 Life Cycle of Florida Key's Waterspouts. Joseph H. Golden. June 1974. 147 p. (COM-74-11477/AS)

No. 71 **Interaction of Two Convective Scales Within a Severe Thunderstorm: A Case Study and Thunderstorm** Wake Vortex Structure and Aerodynamic Origin. Leslie R. Lemon. June 1974. 43 p. (COM-74-11642/AS)

No. 72 Updraft Properties Deduced from Rawinsoundings. Robert P. Davies-Jones and James H. Henderson. October 1974. 117 p. (COM-75-10583/AS)

No. 73 Severe Rainstorm at Enid, Oklahoma - October 10, 1973. L. P. Merritt, K. E. Wilk, and M. L. Weible. November 1974. 50 p. (COM-75-10583/AS)

No. 74 Mesonetwork Array: Its Effect on Thunderstorm Flow Resolution. Stanley L. Barnes. October 1974. 16 p. (COM-75-10248/AS)

No. 75 Thunderstorm-Outflow Kinematics and Dynamics. R. Craig Goff. December 1975. 63 p. (PB-250808/AS)

No. 76 An Analysis of Weather Spectra Variance in a Tornadic Storm. Philippe Waldteufel. May 1976. 80 p. (PB-258456/AS)

No. 77 Normalized Indices of Destruction and Deaths by Tornadoes. Edwin Kessler and J. T. Lee. June 1976. 47 p. (PB-260923/AS)

No. 78 Objectives and Accomplishments of the NSSL 1975 Spring Program. K. Wilk, K. Gray, C. Clark, D. Sirmans, J. Dooley, J. Carter, and W. Bumgarner. July 1976. 47 p. (PB-263813/AS)

No. 79 Subsynoptic Scale Dynamics As Revealed By The Use Of Filtered Surface Data. Charles A. Doswell III. December 1976. 40 p. (PB-265433/AS)

No. 80 The Union City, Oklahoma Tornado of 24 May 1973. Rodger A. Brown, Editor. December 1976. 235 p. (PB-269443/AS)

No. 81 Mesocyclone Evolution and Tornado Generation Within the Harrah, Oklahoma Storm. Edward A. Brandes. May 1977 28 p. (PB-271675/AS)

No. 82 The Tornado: An Engineering-Oriented Perspective. Joseph E. Minor, James R. McDonald, and Kishor C. Mehta. December 1977. 196 p. (PB-281860/AS)

No. 83 Spring Program '76. R. L. Alberty, J. F. Weaver, D. Sirmans, J. T. Dooley, and B. Bumgarner. December 1977. 130 p. (PB280745/AS)

No. 84 Spring Program '77. P. S. Ray, J. Weaver, and NSSL Staff. December 1977. 173 p. (PB-284953/AS)

☆ U.S. GOVERNMENT PRINTING OFFICE:1979—677-072 / 1237